POLITECNICO DI TORINO

Corso di Laurea Magistrale in Ingegneria Elettrica

Tesi di Laurea

Modelling and control of an innovative electrical drive for electrical vehicles

Relatore
Prof. Radu Bojoi

Correlatori:
Prof. Francesco Castelli Dezza
Dott. Davide Cittanti

Laureando
Andrea Comino

Dicembre 2019

"Let the future tell the truth,
and evaluate each one
according to his work and
accomplishments. The
present is theirs; the future,
for which I have really
worked, is mine."

[Nikola Tesla]

Summary

In the automotive world new technologies are entering the market with great potentialities of becoming the future dominant design. These technologies are based on electric traction system cooperating or not with classic combustion engine. In this innovation phase, it is fundamental to fill the gap between old technologies with new ones. For this reason new components and features have to be introduced in the future traction system. In this case study an innovative electromechanical actuator for safety purpose is proposed to be added in the electric traction system in order to improve it. It needs specific conditions to be actuated which are monitored through electrical machine parameters. This innovative actuator will not be analysed, while the whole electric traction system and its relation with it will be treated. This thesis has different aims that comprehend all the aspects of the previously cited system.

The first aim is to develop a complete model of the electric traction of a pure electric vehicle or hybrid electric vehicle in a simulation environment. This electric traction is composed by typical elements as storage system, converter and electrical machine. The storage system is not strictly defined and a battery is preliminary chosen. The selected converter is a three-phase inverter, in specific a two-level inverter. The electric machine is a PMASR motor with high performance and it could work really near to its limits. In addition to these, the mechanical load is also considered in order to simulate the mechanical dynamic too. The chosen simulation environment is Simulink in which every components have been modelled with pre-existing block or ad hoc generated one.
The second aim is to analyse the control method for the electric motor and generate it in the specific programming language. The control method employed is the Direct Flux Vector Control, which is greatly suitable for an automotive electric motor since it is advantageous in flux-weakening operations.
The third aim is to generate a secondary motor control that is active when a safety action of the innovative electromechanical actuator is required. The complete shut-down of the inverter and the electrical machine is necessary to allow the actuator operate. This task is performed by the secondary motor control through a sequence of precise actions. Specific conditions, such as magnet temperature below limits and complete shut-down of the inverter and electrical machine, have to be monitored in order to trigger when necessary the actuator.
The fourth aim of this thesis is to analyse the different method employed to monitor these conditions, thus find out a procedure to estimate the parameters of interest. These quantities are the magnet temperature for safety issue and the magnet back-emf for the

Uncontrolled Generation, which lead to the unsuccessful shut-down of the electrical system.

The system generated in the simulation environments is tested in comparison to a model developed in another simulation tool (PLECS), highlighting its validity. Further step will be testing it in comparison to the real electric traction system when it will be built. Furthermore the implemented control method for the motor, both the principal and the secondary one, are tested in simulation environment and results are provided, showing their suitability and validity. A procedure to estimate the magnet temperature is developed and promising results are shown due to a maximum absolute error of nearly $5\,K$ in particular system state. The magnet back-emf is estimated as a direct consequence of the magnet temperature. These results are the basis for further developments and improvements of this estimation method, which should be tested in the real traction system.

KEYWORDS:
Innovation, electric traction system, Simulink, DFVC, magnet temperature, UCG

Acknowledgements

Cinque anni fa ho iniziato un percorso complicato, cercando di ottenere il meglio da ciò che mi veniva offerto. Questi cinque anni intensi sono finiti. Sono pienamente soddisfatto di tutto ciò che ho raggiunto, ma non avrei mai potuto ottenere tutto ciò senza coloro che sono stati al mio fianco giorno per giorno. Cerco ora di ringraziarli e farli capire quanto hanno contato veramente per me.

Prima di tutto vorrei ringraziare il professor Radu Bojoi per avermi dato fiducia dal primo istante, per avermi dato responsabilità che ad un tesista si ha paura di dare e per vedere in me qualcosa che forse non vedo neanch'io.

Ringrazio Luca, Javier, Ruggero, Michele e Giovanni per avermi accolto nel loro team come se ne avessi sempre fatto parte, per la loro fantastica collaborazione e per avermi sempre sostenuto ed insegnato molto in questo progetto.

Un ringraziamento particolare va a Francesca per l'infinita pazienza che ha portato nei miei confronti e con tutte le mie follie, per avermi sopportato e supportato in ogni momento anche quando sembrava impossibile e per essere stata al mio fianco dandomi la forza di affrontare qualsiasi cosa.

Vorrei ringraziare anche i miei genitori per i loro sacrifici e continui sforzi che hanno permesso di realizzarmi in tutto per tutto, per il loro quotidiano modello di vita basato sull'onestà e sulla fiducia e per i loro saggi consigli che mi hanno permesso di arrivare dove sono ora.

A Matty perché ha saputo aiutarmi ogni volta che ne avessi bisogno, mi ha incoraggiato a superare sempre me stesso e mi ha fornito un modello di resilienza e determinazione senza eguali.

Un grazie di cuore a tutta la mia famiglia, dai nonni agli zii e cugini, per aver creduto ciecamente in me senza mai dubitare un solo istante.

Cristina, Claudio, Graziella e Federica vi ringrazio per aver allargato la mia famiglia nel miglior modo possibile e per avermi saputo ascoltare sia nei momenti migliori sia in quelli peggiori.

A Norman per essere stato il fratello adottivo di sempre dalle elementari fino ad oggi e per essere stato sempre presente ogni volta che ne avessi bisogno.

Un profondo grazie a quello spagnolo-svedese di Davide per aver condiviso i trionfi e le difficoltà con me in questi due anni e per non avermi abbandonato nonostante la distanza.

Ringrazio Davide, Deave, Giorgio, Erik, Bandi e Silvia per tutti i momenti trascorsi assieme, dalle serate ai semplici viaggi in treno, e per essere stati gli amici che ho sempre desiderato.

Un grande grazie a Checco per essermi stato d'ispirazione in questi anni, Michi per avermi aiutato senza mai chiedere qualcosa in cambio, Fiz per non essersi mai risparmiato con me, Albi per essere stato più di un semplice compagno di squadra, Paolo e Silve perchè senza di voi sarebbe stato tutto più noioso, tutti gli altri miei compagni di squadra ed allenatori per avermi permesso di ottenere tante soddisfazioni al di fuori dell'ambito accademico.

Ringrazio Chiara, Dona, Albi e Luca per le loro ventate di allegria, per gli esami preparati assieme, per le lunghe chiaccherate e per non avermi mai mollato malgrado vivessi a 90 km di distanza.

Grazie ancora a Luca, Nour e Riccardo per aver condiviso con me i trionfi e le difficoltà delle school, le ansie sui paper da svolgere e le serate per sfuggire alla routine dell'ASP.

Infine ringrazio Antonio, Francesco, Massimo e Davide per aver condiviso con me questi due anni di pazzie.

Grazie infinite a tutti coloro che ho dimenticato in queste poche righe ma che mi hanno accompagnato, anche se per poco, in questi cinque meravigliosi anni.

Andrea

Contents

List of Figures

List of Tables

List of Nomenclature and Acronyms

ACRONYMS	MEANS
HEV	Hybrid Electric Vehicle
EV	Electric Vehicle
SOC	State Of Charge
IGBT	Insulted Gate Bipolar Transistor
PWM	Pulse Width Modulation
PMASR	Permanent Magnet Assisted Synchronous Reluctance
FEM	Finite Element Analysis
PMSM	Permanent Magnet Synchronous Machine
LUT	Look Up Table
MTPA	Maximum Torque Per Ampere
MTPV	Maximum Torque Per Volt
ISR	Interrupt Service Routine
UCG	Uncontrolled Generation
UR	Uncontrolled Rectifier
RTD	Resistive Temperature Detector
LPTN	Lumped-Parameter Thermal Network
KF	Kalman Filter
EKF	Extended Kalman Filter

Chapter 1

Introduction

In recent years a new design is entered into the vehicle market, becoming a great promise of change the mobility world. This new design is based on the electric traction system, complementing the traditional combustion engine in Hybrid Electric Vehicle (*HEV*) or constituting the only traction system in Electric Vehicle (*EV*). The electric mobility, namely e-mobility, is constantly growing over the past few years. The evidence of this can be found in the market interest for this new technology. In 2018, the whole electric vehicle number is higher than 5.1 million, up 2 million from the previous year and almost doubling the number of new electric vehicle registrations [1]. The trend of *HEV* and *EV* is shown by McKinsey& Company [2] until 2017 in Fig. 1.1:

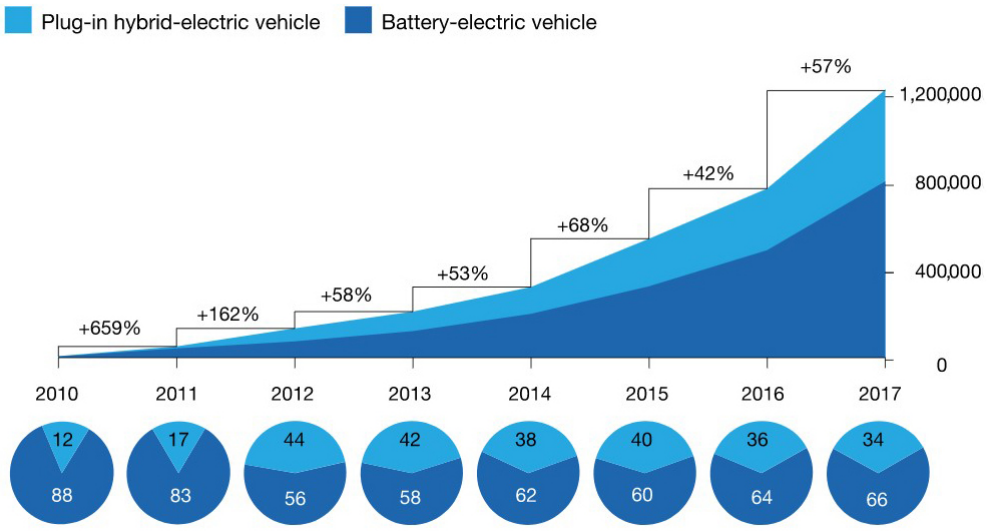

Figure 1.1: Global electric vehicle sales trend from 2010 to 2017

These new technologies are also becoming so important thank to the necessity of reducing pollutant emissions, pushed by new policies at European and International level.

Many vehicle manufacturers have put a considerable effort in investing in these technologies. They are ripping up their business models and their factories are being overhauled to next generation of production. The Volkswagen group is spending €30 billion over the next five years to make an electric or hybrid version of every vehicle in its lineup [3]. Toyota, a pioneer in the electric traction, will invest €2 billion over the next four years to develop electric vehicles in Indonesia [4]. The future of automotive is clearly pushed in the electric direction.

Nonetheless there is still room of improvement for e-mobility, it is a growing technology: it is just at the early adopters phase in the Moore's segmentation. There is a struggling standard war ongoing and the dominant design has not come out yet. New features and components are being introduced in order to win this war. For this reason an innovative electrical drive for electrical vehicles is analysed in this thesis. This innovation is proposed by a company, thus it is protected by confidentiality issue and will be treated limitedly in the thesis. The main elements of this innovative electrical drive are an electric traction system and an innovative electromechanical actuator. The electric traction system is composed by a storage system, a converter and an electrical machine (example reported in Fig. 1.2 [5]). The latter is a highly performing machine, thus it could operate nearly to its limits. For this reason the innovative electromechanical actuator is proposed: it has safety purposes that lead to avoid the electrical traction system failure.

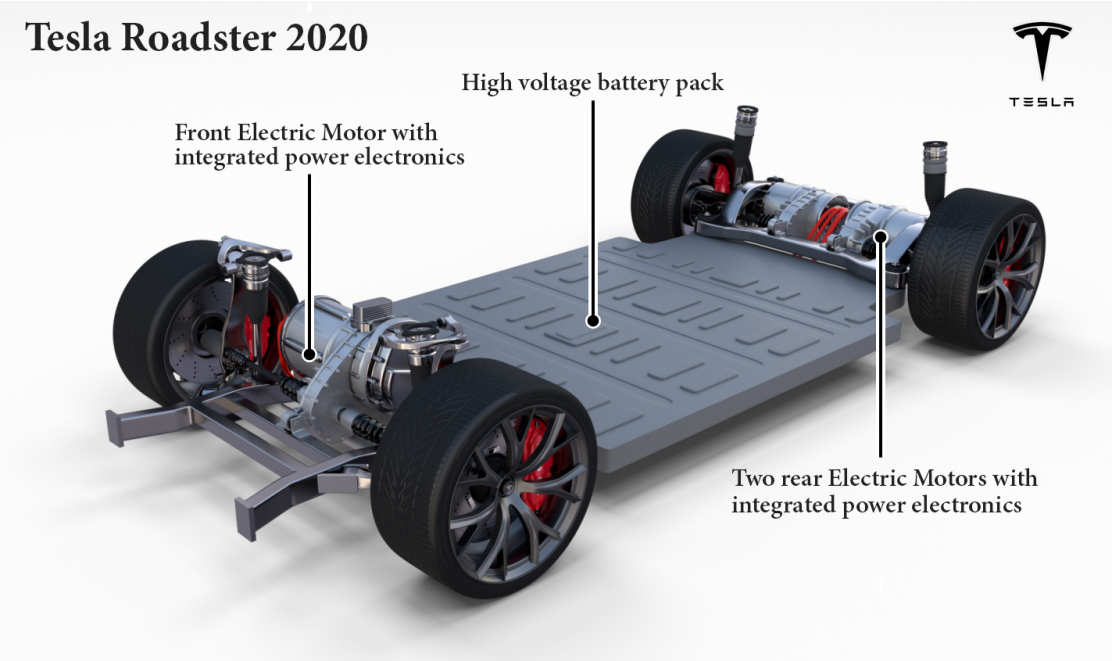

Figure 1.2: Example of electric traction system in the Tesla roadster 2020

The whole system is under development and it has not produced yet, therefore it is analysed only in a simulation environment. The electrical traction system will be analysed

with its interaction with the innovative actuator, while this last will not be treated in this thesis. In specific:

- the electric traction system is modelled in the simulation software Simulink in all its components with the addition of the mechanical load (Chapter 2);
- the motor control is developed and tested in the simulation environment (Chapter 3);
- the motor control when the electromechanical actuator must operate is developed and tested in the simulation environment (Chapter 4);
- the estimation of the quantities necessary to trigger the operation of the innovative actuator are analysed and a method is tested in the simulation environment (Chapter 5).

Chapter 2

Modelling of the system under study

The aim of this chapter is to show and analyse the model of the whole system generated for the simulation. As previously mentioned, the under analysis system is a typical traction system with the addition of the electromechanical actuator, thus its main elements are:

- Storage system (described in section 2.1)
- Converter (described in section 2.2)
- Electrical machine (described in section 2.3)
- Mechanical load (described in section 2.4)

2.1 Storage system model

The technology of storage system for this electric vehicle is not strictly defined and for this reason a battery is preliminary selected. A battery consists of one or more electrochemical cells, which transform stored chemical energy directly into electrical energy [6]. The voltage generated at the battery terminals is proportional to its SOC. In order to model it, there is the possibility to utilise the battery block or the controlled voltage source one, to which the voltage is provided as a function of SOC.

2.1.1 Battery

This block emulates a simple battery as a voltage source and an internal resistor in series, with the chance of customizing different aspects:

- Charge capacity;
- Battery fade;
- Thermal effects;
- Charge dynamics.

The symbol of this block is:

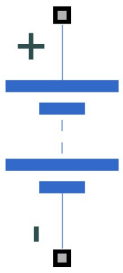

Figure 2.1: Simulink symbol for the Battery block

The first possible customization is to impose an infinite or a finite charge capacity. In the first case the battery has always the same voltage, while in the second one it depends on the battery SOC with the following law:

$$V = V_0 \left(\frac{SOC}{1 - \beta\,(1 - SOC)} \right) \tag{2.1}$$

where V_0 is the battery voltage when it is fully charged at no load and is a constant, evaluated in a way that the battery voltage is $V1$ when the charge is $AH1$. These two last parameters have to be provided by the user in the block mask.

The second customisation allows the user to implement a fade behaviour that consist in a battery performance worsening directly proportional to charge-discharge cycles. This

deterioration changes some internal battery parameters with a multiplier evaluated for each of them. This parameters are V1 and AH1, mentioned above, and the internal resistance. The multipliers are respectively obtained as:

$$\begin{aligned} \lambda_{V1} &= 1 - k_1\, N^{0.5} \\ \lambda_{AH1} &= 1 + k_2\, N^{0.5} \\ \lambda_{R0} &= 1 - k_3\, N \end{aligned} \tag{2.2}$$

where N is the number of discharge cycles completed and k_1, k_2 and k_3 are user-defined coefficients.

The third customization introduces the temperature in the evaluation of the V_0 (eq. 2.1) and of the internal resistance with the following laws:

$$\begin{aligned} V_{0T} &= V_0[1 + \lambda_V(T - T_1)] \\ R_T &= R[1 + \lambda_R(T - T_1)] \end{aligned} \tag{2.3}$$

where λ_V and λ_R are obtained from V_0 and R at a given second temperature. The temperature is evaluated dividing all the ohmic losses with a battery thermal mass, defined by the user.

The last customization introduces a dynamic in the charge and discharge process, adding in series to the battery a resistor in parallel to a capacitor. It is possible to specify the type of dynamic: from one time-constant to five time-constants, respectively from one RC section to five RC sections in series.

2.1.2 Controlled Voltage Source

This block simulates an ideal voltage source that is powerful enough to maintain the requested voltage at its output regardless of the current following through it [7]. The symbol of this block is:

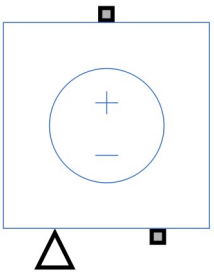

Figure 2.2: Simulink symbol for the Controlled Voltage Source block

The requested voltage is given as Simulink signal to the signal port of the block, therefore it is possible to change it as necessary. In the case of Lithium-Ion cell, in specific the

DowKokam XALT^{TM} 75 Ah High power, the relation between the voltage and the battery capacity is:

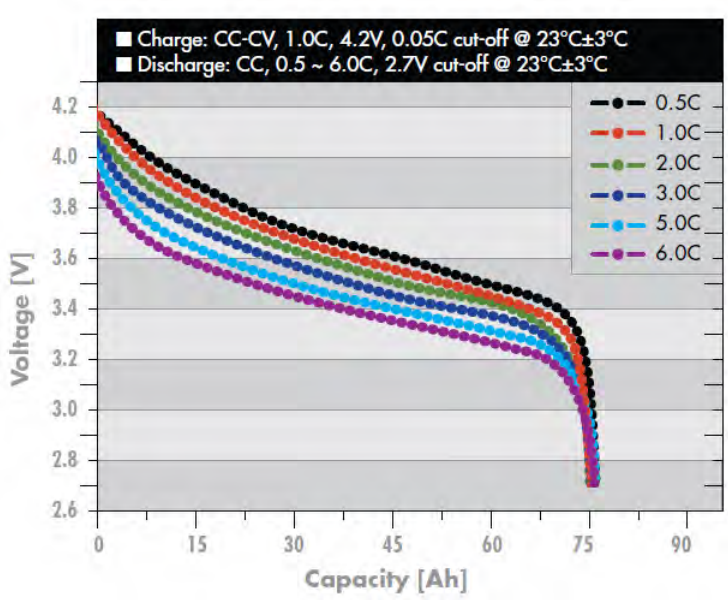

Figure 2.3: Relation between the voltage and the battery capacity for the DowKokam XALT^{TM} 75 Ah High power

Furthermore, if there will be the necessity to emulate a real battery behaviour, a resistor and an inductor can be added in series to it or a parameter that models the battery fade can be taken into account in the previously shown relations.

2.1.3 Block selection

Starting from the premise that the simulations will be shorter than the battery dynamic, the two possible alternatives are considered equivalent for the actual necessities. The differences will be highlighted when longer simulations will be required. The main distinction is in the way the voltage is given as function of the SOC, temperature and fade. The Battery block has less degrees of freedom than the Controlled Voltage Source one, for example the discharge law is strictly defined in the block. Furthermore the last block can model not only a battery but every type of storage system, changing the voltage law as desired.

2.2 Converter model

The converter chosen for the system under analysis is a three-phase inverter. It is a two levels inverter based on IGBT-technologies. It has the following functional scheme:

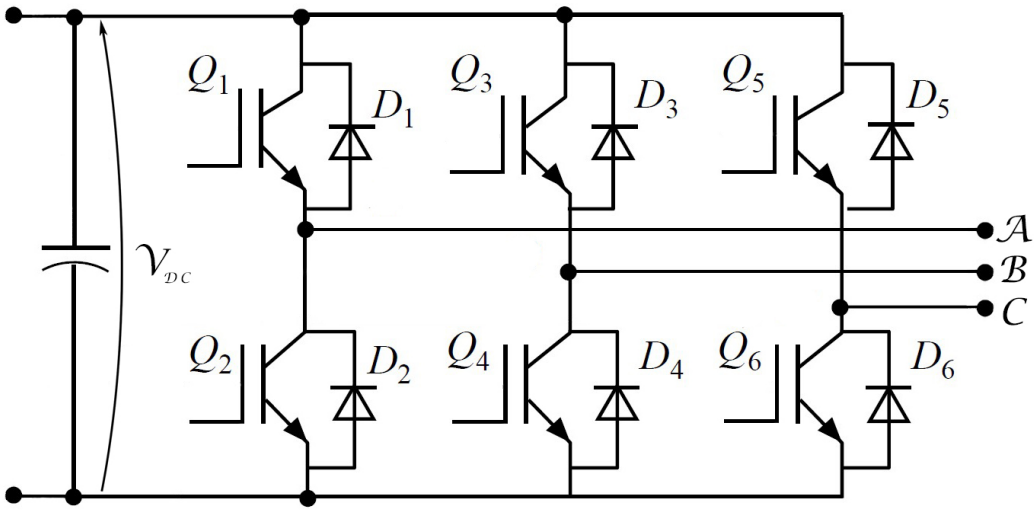

Figure 2.4: Scheme of a two level three-phase inverter

This type of inverter has three legs, one for each phase. Every leg is constituted by two canonic cells, in turn each cell is constituted by an IGBT and a free-wheeling diode. Every IGBT is controlled by a command $Q(t)$, which is obtained by a PWM technique. This technique consist in the comparison between a triangular carrier $tr(t)$ and a signal called duty cycle $d(t)$, done for each phase. The triangular carrier is symmetrical and its absolute maximum value $|\hat{V}_{tr}|$ is equal to one, as shown in Fig. 2.5 in blue.

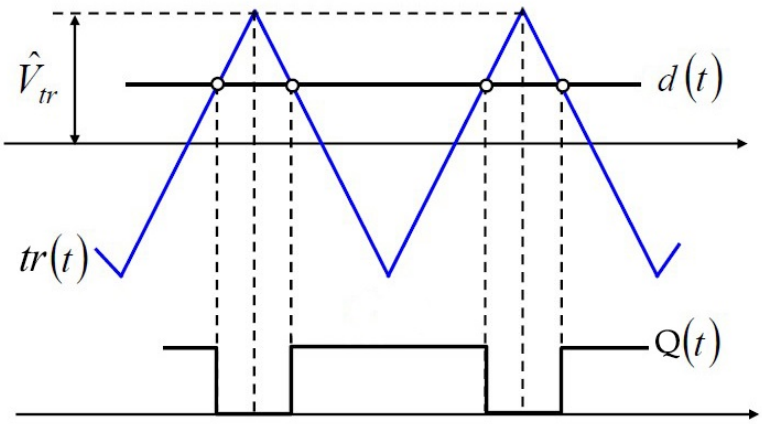

Figure 2.5: Comparison between the triangular carrier and duty cycle

When the triangular carrier is higher than the duty cycle the command $Q(t)$ is equal to zero, while it is equal to one when the duty cycle is higher than the carrier. Three duty cycles are generated, one for each phase, thus three commands $Q(t)$ are generated for the high-side IGBT and the commands for the low-side ones are equal to the negative of the respective high-side one commands.
Utilising a zero-sequence voltage injection, the duty cycle is evaluated for each phase as follows:

$$\begin{aligned} d_A &= \frac{1}{2} + \frac{v_A^*}{V_{DC}} - \frac{1}{2}\frac{v_{min}^* + v_{MAX}^*}{V_{DC}} \\ d_B &= \frac{1}{2} + \frac{v_B^*}{V_{DC}} - \frac{1}{2}\frac{v_{min}^* + v_{MAX}^*}{V_{DC}} \\ d_C &= \frac{1}{2} + \frac{v_C^*}{V_{DC}} - \frac{1}{2}\frac{v_{min}^* + v_{MAX}^*}{V_{DC}} \end{aligned} \tag{2.4}$$

Where

- V_{DC} is the voltage of the DC-link capacitor;
- v_A^*, v_B^* and v_C^* are the reference voltage for each phase, namely the desired output voltage;
- v_{min}^* and v_{MAX}^* are respectively the minimum and the maximum reference voltage.

The output moving average voltage are equivalent to:

$$\begin{aligned} v_A &= \frac{1}{3} V_{DC}\big(2d_A - d_B - d_C\big) \\ v_B &= \frac{1}{3} V_{DC}\big(2d_B - d_A - d_C\big) \\ v_C &= \frac{1}{3} V_{DC}\big(2d_C - d_A - d_B\big) \end{aligned} \tag{2.5}$$

In order to model this inverter, there are two possibilities for the simulation tool employed:

- IGBT
- Converter

2.2.1 IGBT

The IGBT block simulates an insulated gate bipolar transistor with two electrical ports (collector and emitter) and a command port (gate). The symbol of this block is:

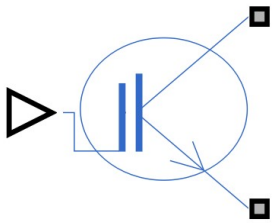

Figure 2.6: Simulink symbol for the IGBT block

A voltage is applied to the command port: if it is higher than a threshold (adjustable by the user) the IGBT moves to an ON-state, otherwise it stay in a state of interdiction (OFF-state), following these equations [8]:

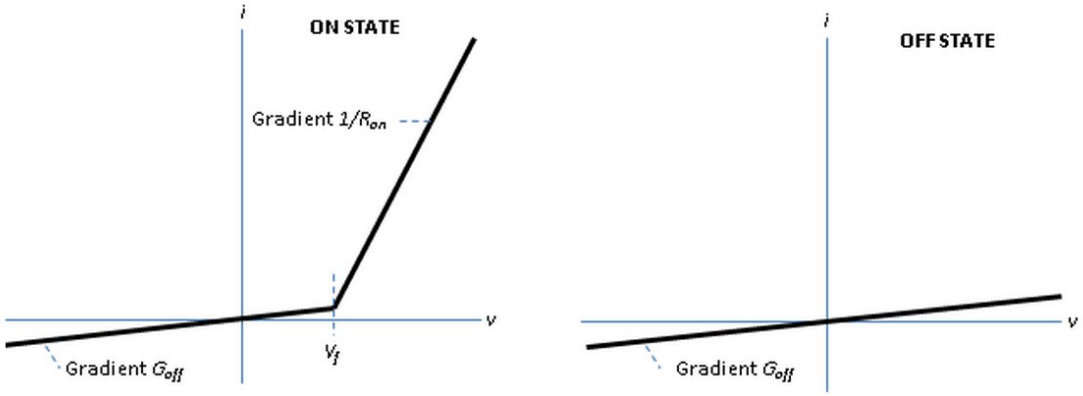

Figure 2.7: Current-Voltage curves of the IGBT

```
if (v>Vf)&&(G>Vth)
   i == (v - Vf*(1-Ron*Goff))/Ron;
else
   i == v*Goff;
end
```

where

- V_f is the forward voltage, from which the IGBT, if it is in ON-state, starts conducting;
- R_{ON} is the ON-state resistance, which is the slope of the curve in the current-voltage plane when the IGBT is conducting;
- G_{off} is the OFF-state conductance, which is the slope of the curve in the current-voltage plane when the IGBT is not conducting, both in ON-state and OFF-state.

This block has also the possibility to insert a free-wheeling diode, called "protection diode" by Simulink, whose parameters can be customize by the user. These parameters are of the same typology of the IGBT with the same properties.
In order to model the converter under study six IGBT blocks are necessary with the respective protection diode enabled.

2.2.2 Converter

The Converter (Three-Phase) block models a three-arm converter circuit that connects a three-phase AC network to a DC network [9]. The symbol of this block is:

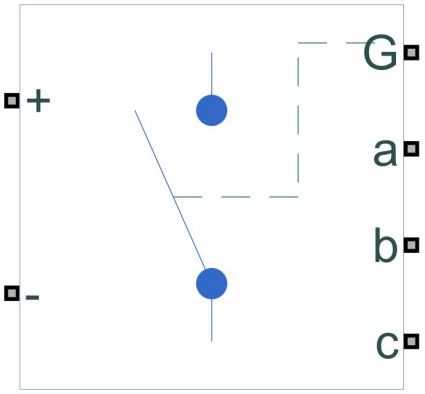

Figure 2.8: Simulink symbol for the Converter block

There is the possibility to customize the type of semiconductor switch and to add also the protection diode. Therefore, choosing IGBT with protection diode, the equivalent electric scheme of this block will be exactly equal to the one needed (Fig. 2.4) a part from the DC-link capacitor. In this case an additional block is necessary to give the gate command to the command port G: the Six-Pulse Gate Multiplexer block. This block multiplex the six gate signals into a single vector.

2.2.3 Block selection and evaluation

The two possible solutions are evaluated in order to find out the best suitable. A test to compare the two blocks has been done with the following conditions:

- V_{DC} equal to 300 V;
- ideal IGBT;
- three-phase load composed by a resistor $R = 20\,\Omega$ and an inductor $L = 1\,mH$
- three-phase reference voltage of amplitude 150 V and frequency of 50 Hz.

The three-phase currents obtained in the test are:

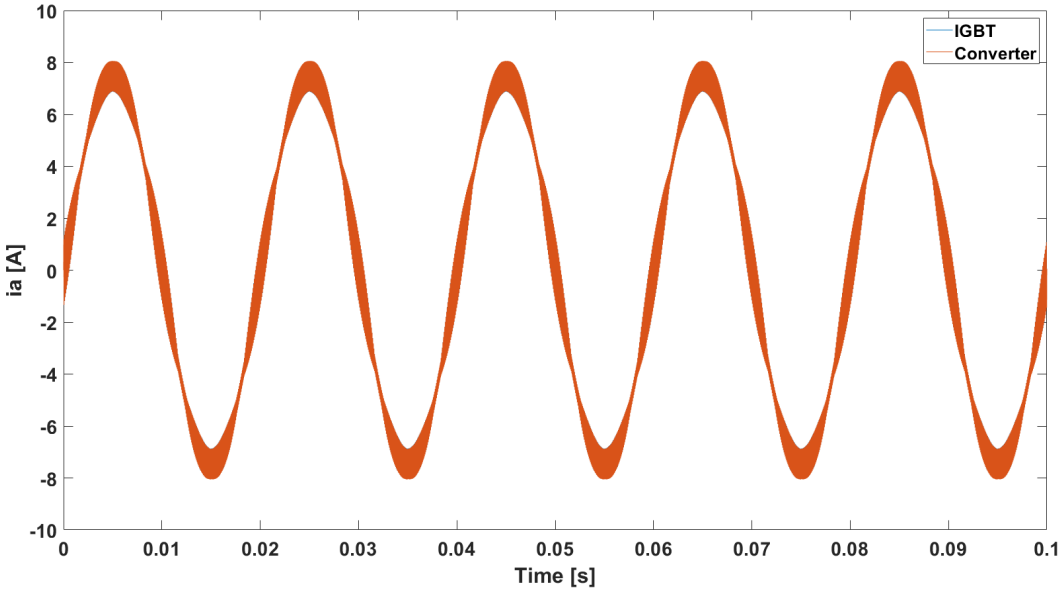

Figure 2.9: Current of phase a in the inverter test

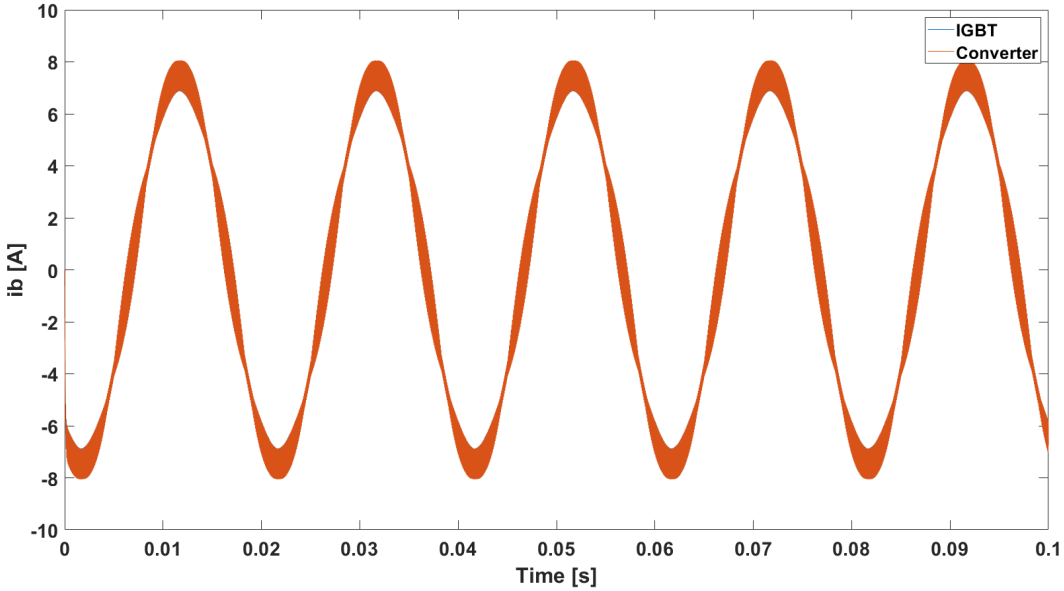

Figure 2.10: Current of phase b in the inverter test

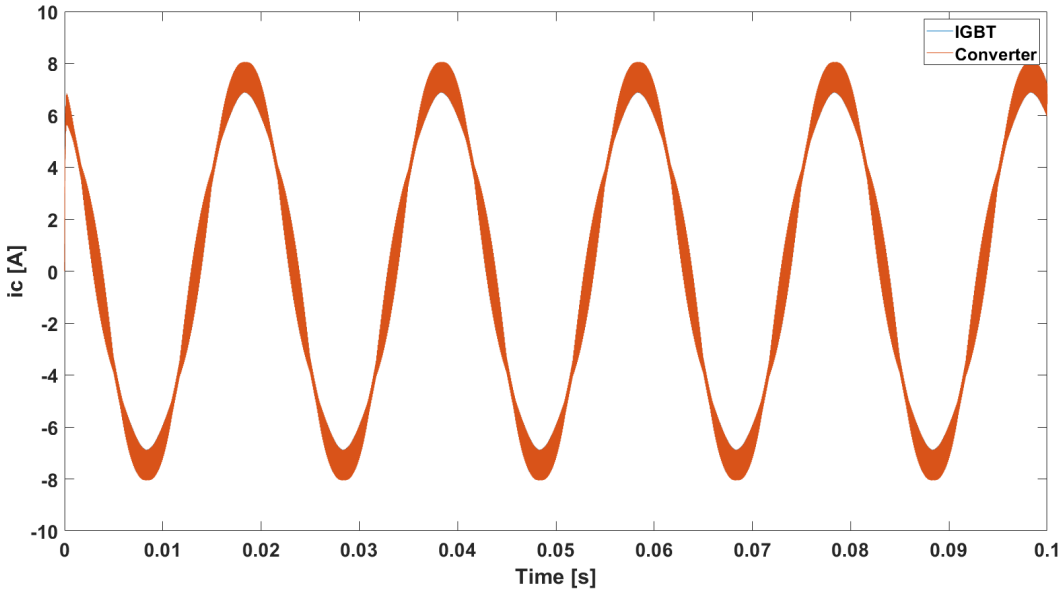

Figure 2.11: Current of phase c in the inverter test

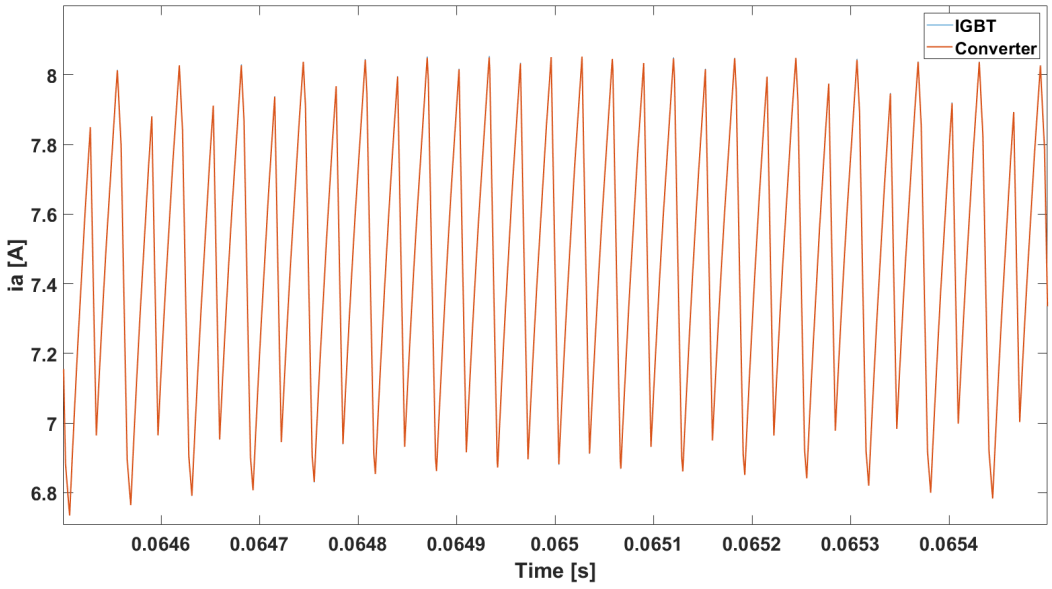

Figure 2.12: Detail of current of phase a in the inverter test

As it is possible to notice, they are exactly the same thus there is not difference between the two blocks. The only discriminating factor is the possibility to explore the inverter scheme with the IGBT block, therefore it offers the chance to test different situations, such as the short-circuit of one IGBT.

2.3 Electrical machine model

The electrical machine considered in the system under analysis is a PMASR motor. This synchronous motor consists of a three-phase wounded stator and an anisotropic rotor with permanent magnet (represented in black in figure 2.13) inserted in it.

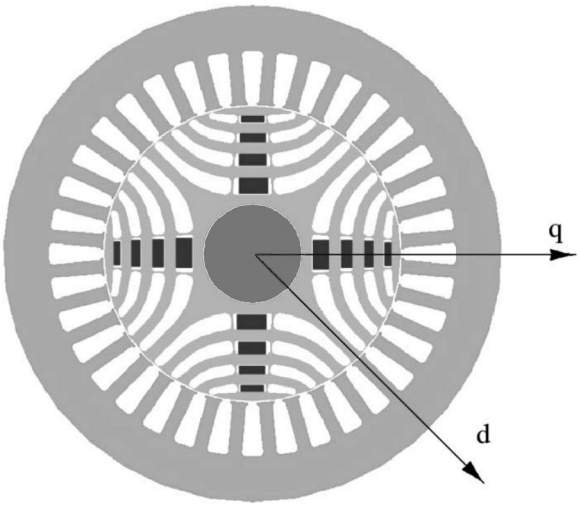

Figure 2.13: Transversal section of a PMASR motor

Taking into account the reference axes joined to the rotor (dq axes), the minimum reluctance path is headed towards the d axis and the permanent magnet flux counteracts the q flux, thus it is directed along the negative direction of the q axis. Therefore the torque generated is constituted by a reluctance component and a permanent magnet component. The equation of the machine in dq frame are:

$$\boldsymbol{v}_{dq} = R\,\boldsymbol{i}_{dq} + \frac{d\boldsymbol{\lambda}_{dq}}{dt} + J\,\omega\,\boldsymbol{\lambda}_{dq} \tag{2.6}$$

$$\boldsymbol{\lambda}_{dq} = [L_{dq}]\,\boldsymbol{i}_{dq} + \boldsymbol{\lambda}_M \tag{2.7}$$

which can be written as:

$$\begin{cases} v_d = R_s\,i_d + \frac{d\lambda_d}{dt} - \omega\,\lambda_q \\ v_q = R_s\,i_q + \frac{d\lambda_q}{dt} + \omega\,\lambda_d \end{cases} \tag{2.8}$$

$$\begin{bmatrix} \lambda_d \\ \lambda_q \end{bmatrix} = \begin{bmatrix} L_{dd} & L_{dq} \\ L_{qd} & L_{qq} \end{bmatrix} \begin{bmatrix} i_d \\ i_q \end{bmatrix} + \begin{bmatrix} 0 \\ -\lambda_M \end{bmatrix} \tag{2.9}$$

As it is possible to notice, the current of d-axis influences the flux of q-axis and the current of q-axis influences the flux of d-axis, leading to nonlinear magnetic behaviour. This phenomenon is called cross-saturation and it is typical of this kind of motor.

The torque is evaluated as:

$$T = \frac{3}{2} p \left(\lambda_d(i_d; i_q)\, i_q - \lambda_q(i_d; i_q)\, i_d \right) \tag{2.10}$$

Since the two components of magnetic flux are generated by both currents, due to the cross saturation phenomenon previously cited, the torque expression is not possible to be simplified any more.
Therefore, in order to model this type of motor, the alternatives offered by the simulation tool (Simulink) are different and depend on the necessities of the case study. The selected options for this case are:

- FEM-Parameterized PMSM
- Hybrid Excitation PMSM
- Simscape component and Controlled Voltage Source

This three possibilities will be analysed in order to find out the most suitable for the case under study.

2.3.1 FEM-Parameterized PMSM

The FEM-Parameterized PMSM block implements a model of a permanent magnet synchronous motor (PMSM) defined in terms of magnetic flux linkage [10]. The symbol of this block is:

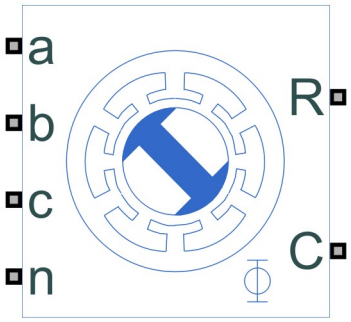

Figure 2.14: Simulink symbol for the FEM-Parameterized PMSM

The input parameters of this block are the flux maps given as a parametrization of currents and rotor angle. Therefore the flux linkages vary depending on the current level and rotor position, allowing also the modelling of non-linear behaviour. It is also possible to insert parameters to evaluate iron losses and mechanical behaviour, indeed it has two mechanical rotational ports. Moreover, there is the opportunity to add the thermal behaviour in order to analyse the temperature evolution of each stator winding. This block permits the user to choose among four different type of parametrization, which differ from the memory requirements and computational effort.

2-D partial derivative data

This parametrization has two options to model the machine behaviour:

- **Constant mutual inductance** - the flux linkage of each phase winding is considered to be linearly dependent from all the other phase currents through the defined constant mutual inductance, while it depends in a nonlinear way on the same phase current, as it is shown in 2.11.

$$\begin{bmatrix}\lambda_a\\ \lambda_b\\ \lambda_c\end{bmatrix} = \begin{bmatrix}0 & -M_s & -M_s\\ -M_s & 0 & -M_s\\ -M_s & -M_s & 0\end{bmatrix}\begin{bmatrix}i_a\\ i_b\\ i_c\end{bmatrix} + \begin{bmatrix}\lambda_a(i_a,\theta_r)\\ \lambda_b(i_b,\theta_r-2\pi/3N)\\ \lambda_c(i_c,\theta_r-4\pi/3N)\end{bmatrix} \tag{2.11}$$

  As input data of the block, the partial derivatives of flux linkage with respect to current and rotor angle have to be provided.

- **Sinusoidal back-emf** - the flux linkage of each phase winding is considered to be nonlinearly dependent on all the phase currents and permanent magnet flux linkage is assumed sinusoidal and dependent on phase currents, as it is shown in 2.12.

$$\begin{bmatrix}\lambda_d\\ \lambda_q\end{bmatrix} = \begin{bmatrix}L_d(i_d,i_q) & \\ & L_q(i_d,i_q)\end{bmatrix}\begin{bmatrix}i_d\\ i_q\end{bmatrix} + \begin{bmatrix}\lambda_M(i_d,i_q)\\ \end{bmatrix} \tag{2.12}$$

  As input data of the block, the inductance in d-axis and q-axis and the permanent magnet flux linkage, all mapped in function of dq-axes currents, have to be provided.

3-D partial derivative data

This parametrization is based on the nonlinear dependence of each phase winding flux linkage with respect on direct and quadrature current (neglecting the zero sequence current) and rotor angle, as shown in 2.13.

$$\begin{bmatrix}\lambda_a\\ \lambda_b\\ \lambda_c\end{bmatrix} = \begin{bmatrix}\lambda_a(i_d,i_q,\theta_r)\\ \lambda_b(i_d,i_q,\theta_r-2\pi/3N)\\ \lambda_c(i_d,i_q,\theta_r-4\pi/3N)\end{bmatrix} \tag{2.13}$$

As input data of the block, the direct and quadrature current and rotor angle maps, the partial derivative of phase-a flux linkage with respect to abc current and rotor angle have to be provided. The block uses Park transform to map the three stator winding currents to direct and quadrature currents [10].

4-D partial derivative data

This parametrization is based on the same hypothesis of the previous one, indeed the employed equation are the ones shown in 2.13. The difference consist of the input data that have to be provided: the abc-phase current and rotor angle maps, the partial derivative of phase-a flux linkage with respect to abc current and rotor angle. In this parametrization Park transform are not utilized.

3-D flux linkage data

This parametrization works directly with flux linkages without having to calculate partial derivatives. There are four different possibilities to provide input data:

- dq-axes flux linkages as a function of dq-axes currents and rotor angle;
- dq-axes flux linkages as a function of total current module and phase and rotor angle;
- a-phase flux linkages as a function of dq-axes currents and rotor angle;
- a-phase flux linkages as a function of total current module and phase and rotor angle.

The last two options are based on the hypothesis of having the b and c flux equal to the a flux shifted in phase.

2.3.2 Hybrid Excitation PMSM

The Hybrid Excitation PMSM block represents a hybrid excitation synchronous machine with a three-phase wye-wound stator. Permanent magnets and excitation windings provide the machine excitation [11]. The symbol of this block is:

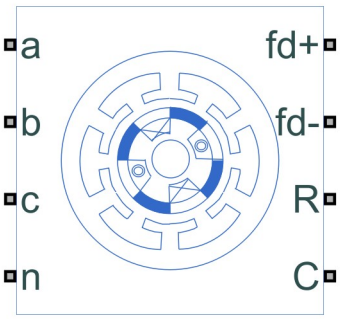

Figure 2.15: Simulink symbol for the Hybrid Excitation PMSM

The equations that are followed by this model are:

$$\begin{bmatrix} v_a \\ v_b \\ v_c \end{bmatrix} = \begin{bmatrix} R_s & 0 & 0 \\ 0 & R_s & 0 \\ 0 & 0 & R_s \end{bmatrix} \begin{bmatrix} i_a \\ i_b \\ i_c \end{bmatrix} + \begin{bmatrix} \frac{d\lambda_a}{dt} \\ \frac{d\lambda_b}{dt} \\ \frac{d\lambda_c}{dt} \end{bmatrix} \tag{2.14}$$

$$\begin{bmatrix}\lambda_a\\ \lambda_b\\ \lambda_c\end{bmatrix} = \begin{bmatrix}L_{aa} & L_{ab} & L_{ac}\\ L_{ba} & L_{bb} & L_{bc}\\ L_{ca} & L_{cb} & L_{cc}\end{bmatrix}\begin{bmatrix}i_a\\ i_b\\ i_c\end{bmatrix} + \begin{bmatrix}\lambda_{aM}\\ \lambda_{bM}\\ \lambda_{cM}\end{bmatrix} + \begin{bmatrix}L_{amf}\\ L_{amf}\\ L_{amf}\end{bmatrix}\begin{bmatrix}i_a\\ i_b\\ i_c\end{bmatrix} \tag{2.15}$$

As it is possible to notice, there are two source of excitation: permanent magnet and rotor windings, which can be used both together to create the rotor magnetic field. All the parameters visible in the equations can be given as input, although they are not variable during the simulation unless a Matlab script is run in parallel with it. Moreover, it is possible to add mechanical parameters to analyse the mechanical behaviour, indeed two rotational ports are provided.

2.3.3 Simscape component and Controlled Voltage Source

In this case a pre-built Simscape block is not used, while two Simulink blocks are employed to emulate the behaviour of an electrical machine. For this purpose some manipulation to the machine equations are necessaries. Starting from 2.6, the flux derivative can be written as:

$$\frac{d\boldsymbol{\lambda}_{dq}}{dt} = \frac{\partial \boldsymbol{\lambda}_{dq}}{\partial \boldsymbol{i}_{dq}} \cdot \frac{d\boldsymbol{i}_{dq}}{dt} \tag{2.16}$$

where the partial derivative of flux with respect to current is defined as incremental inductance, thus generating an incremental inductance tensor:

$$L_{dd} = \frac{\partial \boldsymbol{\lambda}_d}{\partial \boldsymbol{i}_d} \qquad L_{dq} = \frac{\partial \boldsymbol{\lambda}_d}{\partial \boldsymbol{i}_q} \qquad L_{qd} = \frac{\partial \boldsymbol{\lambda}_q}{\partial \boldsymbol{i}_d} \qquad L_{qq} = \frac{\partial \boldsymbol{\lambda}_q}{\partial \boldsymbol{i}_q} \tag{2.17}$$

$$\left[L_{inc,dq}\right] = \begin{bmatrix}L_{dd} & L_{dq}\\ L_{qd} & L_{qq}\end{bmatrix} \tag{2.18}$$

This incremental inductances vary with the working point according to currents. Therefore, the equation 2.6 can be written as:

$$\boldsymbol{v}_{dq} = R\,\boldsymbol{i}_{dq} + \left[L_{inc,dq}\right]\frac{d\boldsymbol{i}_{dq}}{dt} + J\,\omega\,\boldsymbol{\lambda}_{dq} \tag{2.19}$$

The rotational transform is applied in order to write the equation 2.19 in $\alpha\beta$-axes:

$$\boldsymbol{v}_{dq} \cdot A(-\theta) = A(-\theta) \cdot R_s\,\boldsymbol{i}_{dq} + A(-\theta) \cdot \left[L_{inc,dq}\right]\frac{d\boldsymbol{i}_{dq}}{dt} + A(-\theta) \cdot J\,\omega\,\boldsymbol{\lambda}_{dq} \tag{2.20}$$

$$\boldsymbol{v}_{\alpha\beta} = R_s\,\boldsymbol{i}_{\alpha\beta} + A(-\theta) \cdot \left[L_{inc,dq}\right]\frac{d\boldsymbol{i}_{dq}}{dt} + A(-\theta) \cdot J\,\omega\,\boldsymbol{\lambda}_{dq} \tag{2.21}$$

Considering only the second term, characterized by the current derivative, it can be transformed in:

$$\begin{aligned} A(-\theta)\cdot[L_{inc,dq}]\,\frac{d}{dt}\boldsymbol{i}_{dq} = A(-\theta)\cdot[L_{inc,dq}]\,\frac{d}{dt}(A(\theta)\cdot\boldsymbol{i}_{\alpha\beta}) = \\ = A(-\theta)\cdot[L_{inc,dq}]\cdot A(\theta)\,\frac{d}{dt}\boldsymbol{i}_{\alpha\beta} + A(-\theta)\cdot[L_{inc,dq}]\,\frac{d}{dt}(A(\theta))\,\boldsymbol{i}_{\alpha\beta} \end{aligned} \tag{2.22}$$

The first part is equivalent to the tensor of incremental inductance in $\alpha\beta$-axes, as shown in 2.23.

$$[L_{inc,\alpha\beta}] = A(-\theta)\cdot[L_{inc,dq}]\cdot A(\theta) \tag{2.23}$$

Each component of this tensor can be calculated as:

$$[L_{inc,\alpha\beta}] = \begin{bmatrix} l_{\alpha\alpha} & l_{\alpha\beta} \\ l_{\beta\alpha} & l_{\beta\beta} \end{bmatrix} = \begin{bmatrix} cos(\theta) & -sin(\theta) \\ sin(\theta) & cos(\theta) \end{bmatrix}\cdot\begin{bmatrix} L_{dd} & L_{dq} \\ L_{qd} & L_{qq} \end{bmatrix}\cdot\begin{bmatrix} cos(\theta) & sin(\theta) \\ -sin(\theta) & cos(\theta) \end{bmatrix} \tag{2.24}$$

$$\begin{aligned} l_{\alpha\alpha} &= L_{dd}\,cos^2(\theta) + L_{qq}\,sin^2(\theta) - 2\,L_{dq}\,cos(\theta)sin(\theta) \\ l_{\alpha\beta} &= L_{dq}\,(cos^2(\theta) - sin^2(\theta)) + L_{dd}\,cos(\theta)sin(\theta) - L_{qq}\,cos(\theta)sin(\theta) \\ l_{\beta\beta} &= L_{qq}\,cos^2(\theta) + L_{dd}\,sin^2(\theta) + 2\,L_{dq}\,cos(\theta)sin(\theta) \end{aligned} \tag{2.25}$$

Taking into account that:

$$\begin{aligned} cos(2\theta) = cos^2(\theta) - sin^2(\theta) = 1 - 2sin^2(\theta) = 2cos^2(\theta) - 1 \\ sin(2\theta) = 2cos(\theta)sin(\theta) \end{aligned} \tag{2.26}$$

Substituting in 2.25, the tensor of incremental inductances in $\alpha\beta$-axes can be written as:

$$[L_{inc,\alpha\beta}] = \begin{bmatrix} L_{avg} + L_\Delta\,cos(2\theta) - L_{dq}\,sin(2\theta) & L_{dq}\,cos(2\theta) + L_\Delta\,sin(2\theta) \\ L_{dq}\,cos(2\theta) + L_\Delta\,sin(2\theta) & L_{avg} - L_\Delta\,cos(2\theta) + L_{dq}\,sin(2\theta) \end{bmatrix} \tag{2.27}$$

where

$$L_{avg} = \frac{L_{dd} + L_{qq}}{2} \qquad L_\Delta = \frac{L_{dd} - L_{qq}}{2} \tag{2.28}$$

Returning back to 2.22, the second term can be evaluated calculating the derivative of the rotational transform matrix:

$$\frac{d}{dt}(A(\theta)) = -\,\omega \begin{bmatrix} sin(\theta) & -cos(\theta) \\ cos(\theta) & sin(\theta) \end{bmatrix} \tag{2.29}$$

where ω is the electrical rotational speed.

$$A(-\theta) \cdot [L_{inc,dq}] \frac{d}{dt}(A(\theta))\, \boldsymbol{i}_{\alpha\beta} = A(-\theta) \cdot [L_{inc,dq}]\,(-\omega) \begin{bmatrix} sin(\theta) & -cos(\theta) \\ cos(\theta) & sin(\theta) \end{bmatrix} \boldsymbol{i}_{\alpha\beta} \tag{2.30}$$

Considering that $\boldsymbol{i}_{\alpha\beta} = A(\theta)\boldsymbol{i}_{dq}$, it is possible to write 2.30 as:

$$A(-\theta)\cdot[L_{inc,dq}]\,(-\omega) \begin{bmatrix} sin(\theta) & -cos(\theta) \\ cos(\theta) & sin(\theta) \end{bmatrix} \begin{bmatrix} cos(\theta) & -sin(\theta) \\ sin(\theta) & cos(\theta) \end{bmatrix} \boldsymbol{i}_{dq} = A(-\theta)\cdot[L_{inc,dq}]\,(-\omega) J \boldsymbol{i}_{dq} \tag{2.31}$$

Therefore, the stator equation in $\alpha\beta$-axes are written as:

$$\begin{aligned} \boldsymbol{v}_{\alpha\beta} &= R_s\, \boldsymbol{i}_{\alpha\beta} + [L_{inc,\alpha\beta}] \frac{d\boldsymbol{i}_{\alpha\beta}}{dt} + A(-\theta) \cdot [L_{inc,dq}]\,(-\omega) J \boldsymbol{i}_{dq} + A(-\theta) \cdot J\, \omega\, \boldsymbol{\lambda}_{dq} = \\ &= R_s\, \boldsymbol{i}_{\alpha\beta} + [L_{inc,\alpha\beta}] \frac{d\boldsymbol{i}_{\alpha\beta}}{dt} + A(-\theta) \cdot \left[[L_{inc,dq}]\,(-\omega) J \boldsymbol{i}_{dq} + J\, \omega\, \boldsymbol{\lambda}_{dq} \right] \end{aligned} \tag{2.32}$$

The last term in brackets is equivalent to the electromotive force in dq-axes, which, multiplied for the rotational transform $A(-\theta)$, is equal to the electromotive force in $\alpha\beta$-axes:

$$\boldsymbol{e}_{\alpha\beta} = A(-\theta) \cdot \left[[L_{inc,dq}]\,(-\omega) J \boldsymbol{i}_{dq} + J\, \omega\, \boldsymbol{\lambda}_{dq} \right] \tag{2.33}$$

$$\boldsymbol{v}_{\alpha\beta} = R_s\, \boldsymbol{i}_{\alpha\beta} + [L_{inc,\alpha\beta}] \frac{d\boldsymbol{i}_{\alpha\beta}}{dt} + \boldsymbol{e}_{\alpha\beta} \tag{2.34}$$

In order to transform equation 2.34 in *abc* frame, the inverse Park transform $[T]^{-1}$ is applied:

$$[T]^{-1} \cdot \boldsymbol{v}_{\alpha\beta} = R_s\, [T]^{-1} \cdot \boldsymbol{i}_{\alpha\beta} + [T]^{-1} \cdot [L_{inc,\alpha\beta}] \frac{d\boldsymbol{i}_{\alpha\beta}}{dt} + [T]^{-1} \cdot \boldsymbol{e}_{\alpha\beta} \tag{2.35}$$

Consequently, the equation 2.35 is equal to:

$$\boldsymbol{v}_{abc} = R_s\,\boldsymbol{i}_{abc} + [T]^{-1}\cdot[L_{inc,\alpha\beta}]\,\frac{d\boldsymbol{i}_{\alpha\beta}}{dt} + \boldsymbol{e}_{abc} \tag{2.36}$$

Taking in account that $\boldsymbol{i}_{\alpha\beta} = [T]\cdot\boldsymbol{i}_{abc}$ and the Park transform is time-independent, the previous equation can be written as:

$$\boldsymbol{v}_{abc} = R_s\,\boldsymbol{i}_{abc} + [T]^{-1}\cdot[L_{inc,\alpha\beta}]\cdot[T]\frac{d\boldsymbol{i}_{abc}}{dt} + \boldsymbol{e}_{abc} \tag{2.37}$$

where

$$L_{abc} = \begin{bmatrix} l_{aa} & l_{ab} & l_{ac} \\ l_{ba} & l_{bb} & l_{bc} \\ l_{ca} & l_{cb} & l_{cc} \end{bmatrix} = [T]^{-1}\cdot[L_{inc,\alpha\beta}]\cdot[T] \tag{2.38}$$

In order to evaluate this product among matrices the tensor of incremental inductances in $\alpha\beta$-axes must have three rows and three columns, thus one row and one column of zeros have been added to it. Therefore, the terms of the tensor of incremental inductances are equivalent to:

$$\begin{aligned}
l_{aa} &= \frac{2}{3}\,l_{\alpha\alpha} \\
l_{ab} = l_{ba} &= \frac{1}{3}\left[-l_{\alpha\alpha} + \sqrt{3}\,l_{\alpha\beta}\right] \\
l_{ac} = l_{ca} &= \frac{1}{3}\left[-l_{\alpha\alpha} - \sqrt{3}\,l_{\alpha\beta}\right] \\
l_{bb} &= \frac{1}{3}\left[\frac{l_{\alpha\alpha}}{2} + \frac{3}{2}\,l_{\beta\beta} - \sqrt{3}\,l_{\alpha\beta}\right] \\
l_{bc} = l_{cb} &= \frac{1}{3}\left[\frac{l_{\alpha\alpha}}{2} - \frac{3}{2}\,l_{\beta\beta}\right] \\
l_{cc} &= \frac{1}{3}\left[\frac{l_{\alpha\alpha}}{2} + \frac{3}{2}\,l_{\beta\beta} + \sqrt{3}\,l_{\alpha\beta}\right]
\end{aligned} \tag{2.39}$$

Moreover, it is possible to add the contribution of leakage inductances to the equation 2.37, obtaining:

$$\boldsymbol{v}_{abc} = R_s\, \boldsymbol{i}_{abc} + L_{\sigma s}\frac{d\boldsymbol{i}_{abc}}{dt} + [L_{inc,abc}]\frac{d\boldsymbol{i}_{abc}}{dt} + \boldsymbol{e}_{abc} \tag{2.40}$$

In contrast to the tensor of incremental inductances, the leakage inductances are not variable.
Considering the equation 2.40, the equivalent circuit for the electric machine is the following:

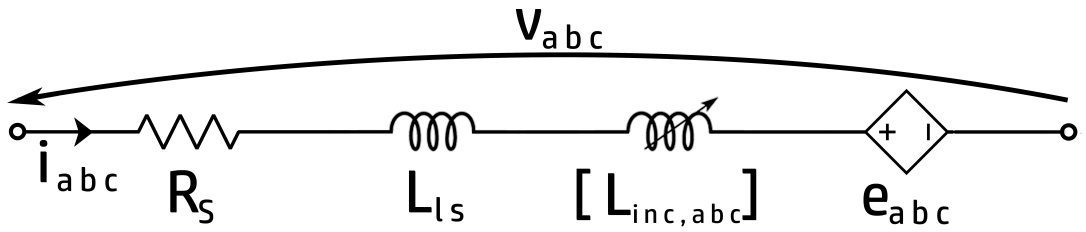

Figure 2.16: Equivalent circuit for the electric machine

This circuit is an electric equivalent of the electrical machine, thus mechanical behaviour is not considered. For this reason the torque is evaluated through equation 2.10, utilising fluxes coming from LUT and currents measured. This value will be integrated in the mechanical load model (section 2.4).
In order to replicate this circuit (Fig. 2.16) in Simscape-Simulink, two blocks are necessary:

- Three-phase controlled voltage source;
- Simscape component.

The first one is necessary to model the back-emf in *abc*-frame, while the second one is employed to model the stator resistances, the leakage inductances and the matrix of incremental inductances in *abc*-frame.

Three-phase Controlled Voltage Source

The Controlled Voltage Source (Three-Phase) block represents an ideal three-phase voltage source that maintains the specified voltage regardless of the current through it [12]. The symbol of this block is:

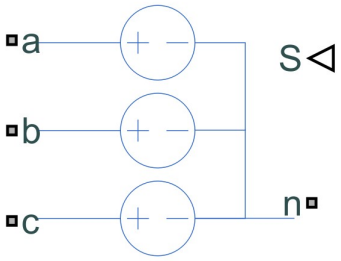

Figure 2.17: Simulink symbol for the Three-phase Controlled Voltage Source block

Furthermore, it is a controlled source, thus it maintains the voltage given as input in the logic port S. For this reason it has been chosen in order to model the back-emf in *abc*-frame, because the latter is a variable voltage source depending on currents, fluxes and speed. Therefore, fluxes in *dq*-axes are evaluated through a LUT, in which the inputs are currents in *dq*-axes, then equation 2.33 is applied and finally the Park transform is employed to obtain the needed results. These values are given as an input vector to the Simulink block.

Simscape component

The Simscape Component block lets the user generate a Simscape block directly from a textual component file, skipping the library build process [13]. The symbol of this block is:

Figure 2.18: Simulink symbol for the Simscape component block

As it is possible to notice, it has no specification because a component file has not deployed in it yet. In order to do this, a file with the *.ssc* has to be created and filled with the code necessary to make the block follow the desired behaviour. In this case, this block is utilized to model the stator resistor, the leakage stator inductor and the matrix of incremental inductances. The first two elements can be model using standard blocks, while for the third one there is not a suitable block. This block should behave as a three-phase inductor, with auto and mutual coupling, and there should be the possibility to give as input the inductance values because they are variable with currents. Because of this, a personal code has been developed to simulate this behaviour and inserted in the Simscape component. This code is divided in different parts that perform different tasks:

1. **Definition of nodes:**

```
nodes
   pa_in = foundation.electrical.electrical;    % a:left
   pb_in = foundation.electrical.electrical;    % b:left
   pc_in = foundation.electrical.electrical;    % c:left
   pa_out = foundation.electrical.electrical;   % a:right
   pb_out = foundation.electrical.electrical;   % b:right
   pc_out = foundation.electrical.electrical;   % c:right
end
```

In this section the input and output nodes are defined. All of these nodes are defined as electrical ones in order to be connected to other Simscape blocks of the same type. Since it is a three-phase element there are three input nodes and three output ones. The final comments in green are still part of the code and they are used to place physically the nodes on the block mask.

2. **Definition of inputs:**

```
inputs
   L = {[0 0 0 0 0 0 0 0 0],'H'};    % L:left
   Ldisp = {0, 'H'};                 % Lls:left
   R = {0, 'Ohm'};                   % R:left
end
```

In this part the variables that are given as logic input are defined. The logic input is a port as the electrical one but it is employed to insert in the block the parameter necessary for equations. Firstly, the tensor of inductances is defined and it is given as a vector of nine elements, which will be evaluated through the equations 2.17, 2.27 and 2.39. Then the leakage inductance and the resistance are defined as single values. Moreover the initial value and the unit of measurement are defined for every inputs. Again the final comments in green are used to place physically the input logic ports.

3. **Definition of variables:**

```
variables
   ia = {0, 'A'};   % Current phase a
   ib = {0, 'A'};   % Current phase b
   ic = {0, 'A'};   % Current phase c
   va = {0, 'V'};   % Voltage phase a
   vb = {0, 'V'};   % Voltage phase b
   vc = {0, 'V'};   % Voltage phase c
end
```

In this section the variables used in the equations inside the block are defined. They are the currents flowing through the three branches and the voltage drops across the three elements modelled. There is the possibility to define their unit of measurement and set their initial values through the block mask.

4. **Definition of branches:**

```
branches
   ia :  pa_in.i -> pa_out.i;   % Current phase a through from
                                   node pa_in to node pa_out
   ib :  pb_in.i -> pb_out.i;   % Current phase b through from
                                   node pb_in to node pb_out
   ic :  pc_in.i -> pc_out.i;   % Current phase c through from
                                   node pc_in to node pc_out
end
```

In this portion of code the path of currents is defined. In this case there are not particular necessities thus every phase current flows from the own input node to the respective output one.

5. **Definition of equations:**

```
equations
   va == pa_in.v - pa_out.v;
   vb == pb_in.v - pb_out.v;
   vc == pc_in.v - pc_out.v;
   va == L(1)*ia.der + L(2)*ib.der + L(3)*ic.der + Ldisp*ia.der +
         + R*ia;
   vb == L(4)*ia.der + L(5)*ib.der + L(6)*ic.der + Ldisp*ib.der +
         + R*ib;
   vc == L(7)*ia.der + L(8)*ib.der + L(9)*ic.der + Ldisp*ic.der +
         + R*ic;
end
```

In this final part the equation that regulate the block behaviour are defined. As it is possible to notice they are based on 2.37 equation.

The final aspect of the block Simscape component, after having deployed the personal code in it, is the following:

Figure 2.19: Simulink symbol for the personalised Simscape component block

2.3.4 Block selection and evaluation

Starting from the three possibilities suitable to model the electric machine, one of these has been chosen for the model. The Three-phase Controlled Voltage Source in combination with the personalised Simscape Component is chosen. The reason of this choice can be found in:

- great simplicity of the model;
- best suitability for the case under analysis;
- possibility to control the machine parameter directly in Simulink.

In order to evaluate this built model, it has been compared to an equal and tested model built in another simulation tool: PLECS. It has been done a comparison test using the same flux maps for the two simulation tools. The test conditions are the following:

- short-circuit of the stator;
- speed increasing with a ramp of slope $5000\,rad/s^2$;
- stator resistance equal to $1\,\Omega$;
- stator leakage inductance equal to $0.001\,mH$.

The currents obtained are the following:

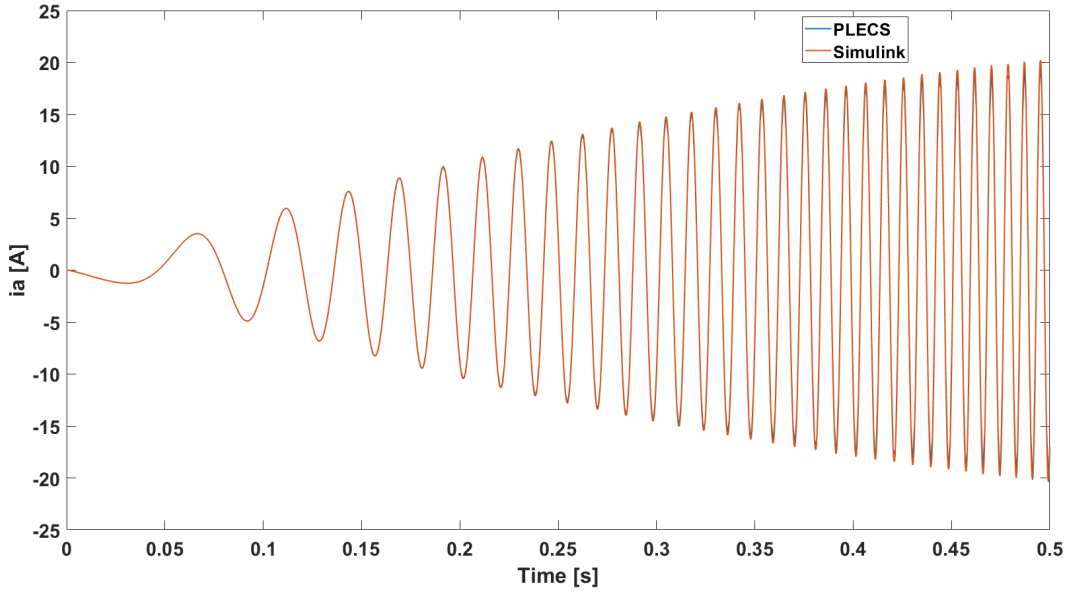

Figure 2.20: Current of phase a in the motor test

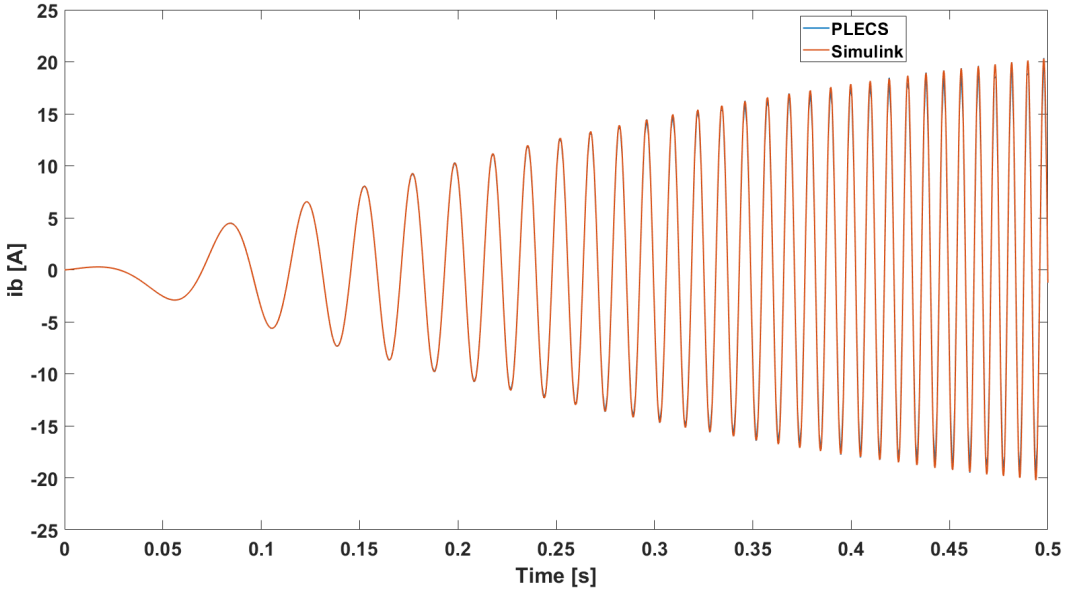

Figure 2.21: Current of phase b in the motor test

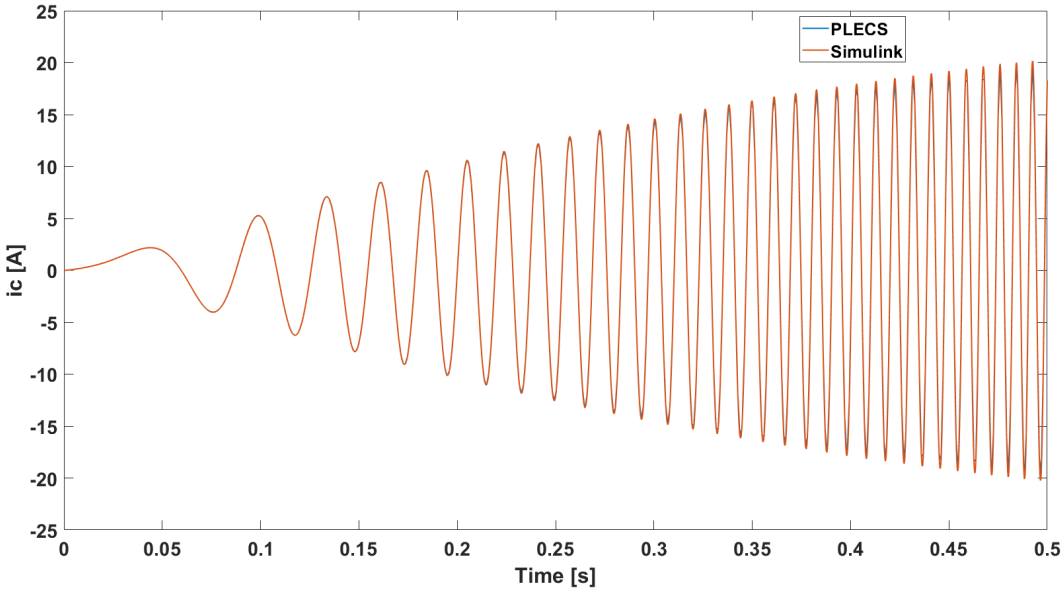

Figure 2.22: Current of phase c in the motor test

The results obtained are in line with the expected one: the unique voltage source is the back-emf of the magnet and it increases with the speed, thus currents increase too. Furthermore, the results of the two simulation tools are exactly the same, a part from some slight differences caused by the different solver, as it is possible to notice in figure 2.23.

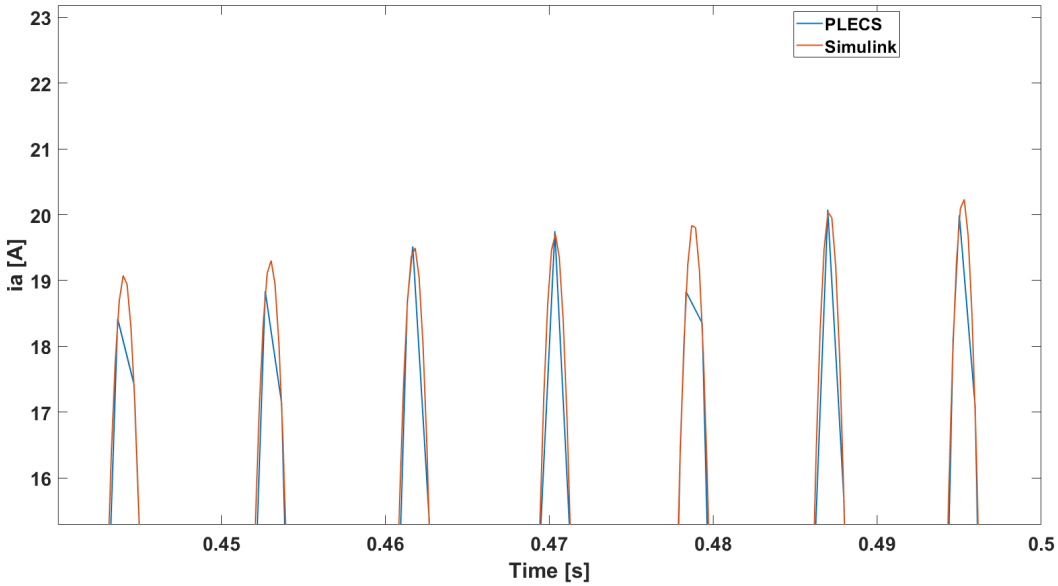

Figure 2.23: Detail of current of phase a in the motor test

2.4 Mechanical load model

The mechanical load in the system under study is the electric vehicle whose traction has been previously analysed. Pursuing the target of modelling it, a great simplification is applied: the vehicle is wholly considered as an equivalent inertia seen by the electrical machine. Therefore it is not possible to go inside the mechanical system in details, but only to analyse the mechanical response at the outlet of the electrical machine.

2.4.1 Ideal Torque Source

The first step is to convert the Simulink torque signal coming from the electrical machine into a Simscape mechanical signal. This allows to emulate the mechanical behaviour of the electrical machine. For this reason the Ideal Torque Source block is utilised:

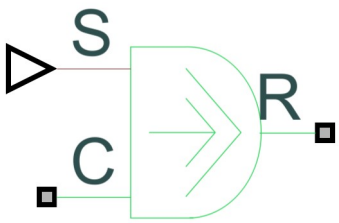

Figure 2.24: Simulink symbol for the Ideal Torque Source block

The Ideal Torque Source block represents an ideal source of mechanical energy that generates torque proportional to the input physical signal [14]. The input port is S, while C and R are mechanical rotational ports. The relative angular speed is evaluated as the difference between R angular speed and C angular speed. If the torque signal entering in S is positive, the torque is applied from C to R. The C port is connected to a mechanical rotational reference. This block is defined ideal because the losses are neglected and it maintains the torque requested at any speeds.

2.4.2 Inertia and Rotational Free End

As previously mentioned, the vehicle is modelled as a simple equivalent inertia therefore the Inertia block is utilised:

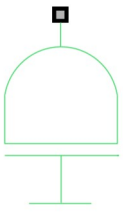

Figure 2.25: Simulink symbol for the Inertia block

This block represents an ideal mechanical rotational inertia, described with the following equation [15]:

$$T = J\frac{d\omega}{dt} \tag{2.41}$$

It has one mechanical rotational port which has to be connected to the R port of the Ideal Torque Source, because the Inertia positive direction is from its port to the reference one, C port of the Ideal Torque Source.

Furthermore, there is the necessity to put a block that allows the Inertia to rotate freely and has an initial speed different from zero. The Rotational Free End block is employed:

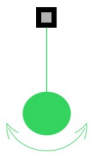

Figure 2.26: Simulink symbol for the Rotational Free End block

This block is used to terminate mechanical rotational port that is necessary to leave unconnected [16].

2.4.3 Ideal Rotational Motion Sensor

Finally, the speed of the equivalent Inertia has to be measured in order to provide it to the electrical machine model and to the control part. The Ideal Rotational Motion Sensor block is utilised:

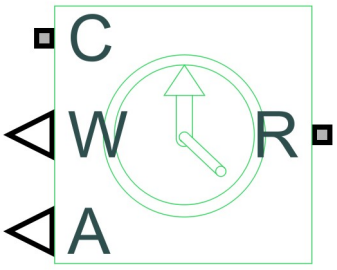

Figure 2.27: Simulink symbol for the Ideal Rotational Motion Sensor block

This block emulates a sensor that measures the speed between two mechanical rotational ports ad converts it into control signals proportional to angular speed and angular position. R and C are the mechanical rotational ports. W and A are physical signal output ports for speed and angular displacement, respectively [17].

The speed is measured as:

$$\omega = \omega_R - \omega_C \tag{2.42}$$

The positive direction is from port R to port C. The latter is connected to the mechanical rotational reference.

An additional block is introduce to transform the ideal behaviour into a real encoder behaviour: the quantizer block.

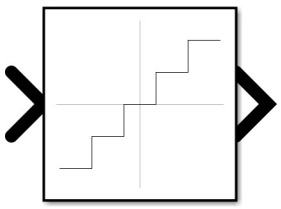

Figure 2.28: Simulink symbol for the Quantizer block

It quantise the input at given interval, which is the 2π divided by the number of notches of the encoder.

Chapter 3

Motor control

The method utilised for the motor control in this case study is the Direct Flux Vector Control. This method is usually employed in traction because it is notably convenient in flux-weakening operation, since it easily guarantees maximum torque production under current and voltage limitations [18]. The first step consists in referring the whole machine model in d_s and q_s axes, where the first one is headed towards the stator flux and the second one is normal to it, as shown in Fig. 3.1. This step is necessary due to the fact that the control is based on:

- direct regulation of the stator flux amplitude through the respective voltage component v_{ds};
- load angle δ regulation, equal to torque regulation, through the respective voltage component v_{qs}.

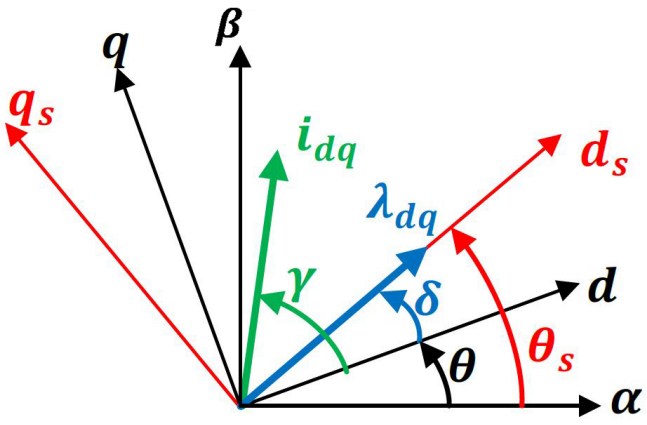

Figure 3.1: Vector diagram with d_s and q_s axes

In order to obtain the new machine equations, the rotational transform has to be applied with the load angle δ to the dq-axes equations.

The new equation obtained are:

$$v_{ds} = R_s\, i_{ds} + \frac{d\lambda}{dt} \tag{3.1}$$

$$v_{qs} = R_s\, i_{qs} + \lambda\,(\omega + \frac{d\delta}{dt}) \tag{3.2}$$

$$T = \frac{3}{2}\, p\, \lambda\, i_{qs} \tag{3.3}$$

It is possible to notice from 3.1 that the flux amplitude is directly regulated through the voltage in d_s-axis, while, from 3.2, the load angle is directly regulated through the voltage in q_s-axis. As mentioned above, the load angle regulation means torque regulation, which it is possible to be done directly through the current in q_s-axis as shown in 3.3.

The scheme of this control method is:

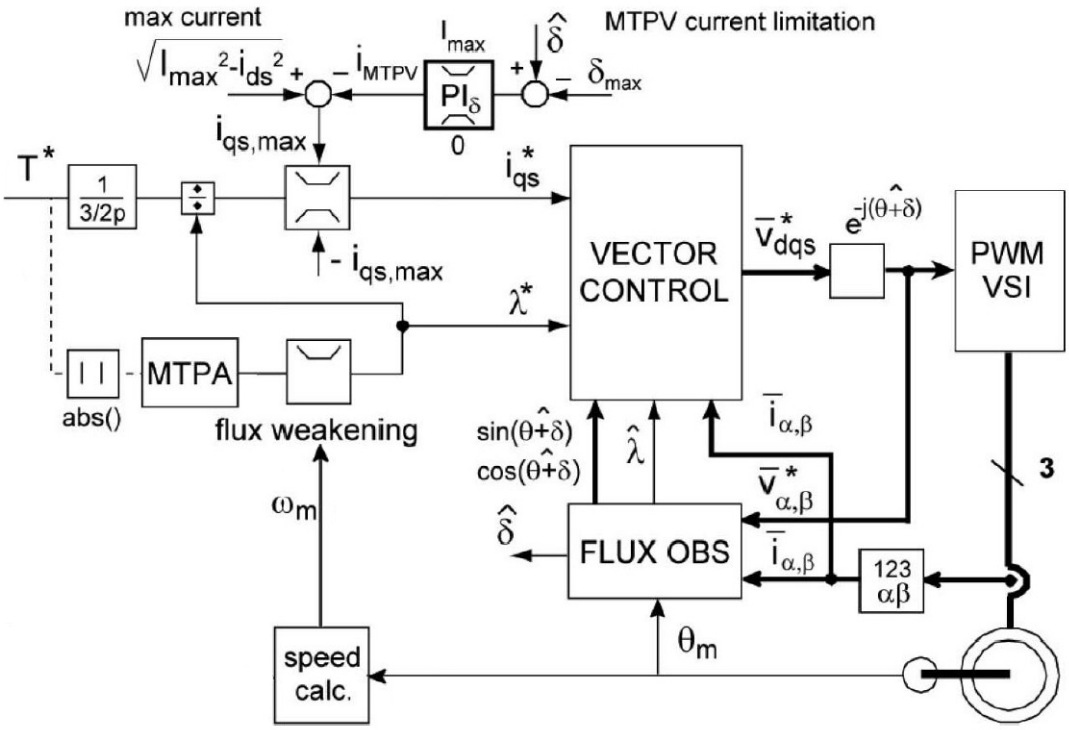

Figure 3.2: Scheme of the Direct Flux Vector Control

The main components of this scheme are:

- an MTPA-based generation of flux reference λ^* and current reference i^*_{qs};
- a flux weakening logic;

- an MTPV logic;
- a closed loop for the flux amplitude that generates as output the reference voltage in d_s-axis;
- a closed loop for the current in q_s-axis that generates as output the reference voltage in q_s-axis;
- a flux observer whose purpose is to observe the stator flux amplitude and its angular position in respect of the $\alpha\beta$-axes;

These main components will be now analysed.

3.1 MTPA-based generation of references

In this case study there is not a speed closed loop: there is not a speed reference that is compared to the measured one in order to obtain the torque reference through a PI regulator. This task is assigned to the vehicle driver that imposes the desired speed using the speed indicator. For this reason the torque reference is directly generated from the accelerator pedal and it is given as input to the control scheme. This reference is employed to obtain the reference of the flux amplitude and of the current in q_s-axis, as shown in Fig. 3.3.

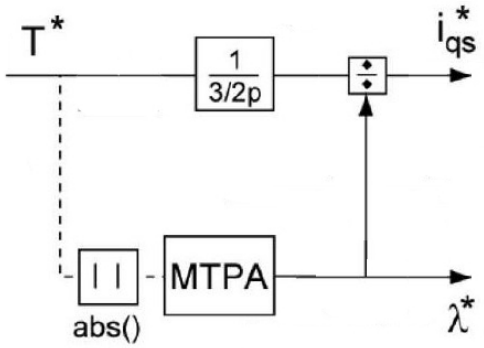

Figure 3.3: Scheme of the MTPA-based generation of references

Firstly, the flux reference is evaluated applying an MTPA algorithm. For this type of electrical machine, a LUT is employed to obtain the flux reference. The LUT is an array of flux amplitude, which is associated to an evenly spaced array of torque values. The LUT is calculated only for positive torque values thus the absolute value is applied to the torque reference. The two torque values, among which the desired torque is included, are selected and a linear interpolation is applied to obtain the flux value associated to the reference torque as shown in Fig. 3.4.

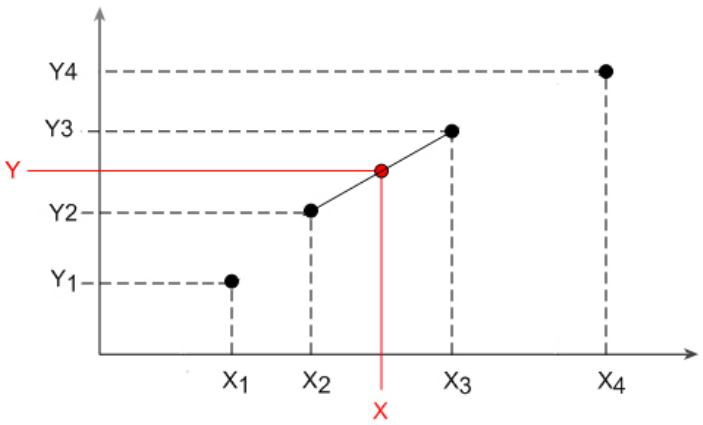

Figure 3.4: Scheme of the MTPA-based generation of references

The linear interpolation is applied using:

$$Y = \frac{Y_2 - Y_1}{X_2 - X_1} (X - X_1) + Y_1 \tag{3.4}$$

Then, the equation 3.3 is employed in order to calculate the reference value for the current in q_s-axis. These references are effective only when the motor is working in an MTPA point, when flux-weakening or MTPV algorithm are necessary, some additional algorithm are applied (Sec. 3.2 and 3.3).

3.2 Flux-weakening logic

As mentioned above, when flux-weakening is needed an additional algorithm is necessary to exit from MTPA curve and start reducing flux amplitude. This reduction is strictly connected to the voltage limitation led by inverter limits.
The voltage limitation condition is given by [19]:

$$\left(R_s\, i_{ds}\right)^2 + \left(R_s\, i_{qs} + \omega\, \lambda\right)^2 \leq V_{max}^2 \tag{3.5}$$

Therefore, neglecting the i_{ds} contribution, the flux amplitude is limited applying the following formula [18]:

$$\lambda^* \leq \frac{V_{max} - R_s\, |i_{qs}|}{|\omega|} \tag{3.6}$$

where

- V_{max} is the maximum output voltage that the inverter can provide, thus in this case it is evaluated from the measured DC-link voltage as:

$$V_{max} = \frac{V_{DC}}{\sqrt{3}} \tag{3.7}$$

- R_s is the estimated stator resistance;
- i_{qs} is the current in q_s-axis;
- ω is the electrical angular speed.

The resistive term in 3.8 is used only for low-power motors, otherwise it can be neglected [18]. From 3.8, it is possible to highlight that the flux-weakening starts in an adaptive manner according to the voltage limit, required current and measured speed.
Consequently a saturation block is added in the control scheme above shown3.3:

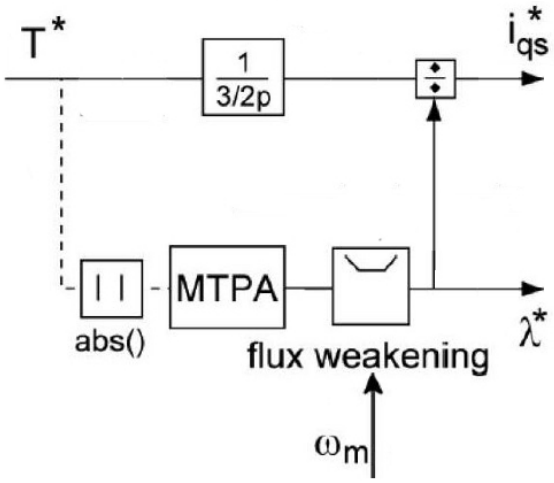

Figure 3.5: Scheme of the MTPA-based generation of references with the addition of flux-weakening logic

Furthermore, it is possible to reduce the limiting term for the flux in order to permit the regulation of current in q_s-axis, such as:

$$\lambda^* \leq 0.9 \, \frac{V_{max} - R_s \, i_{qs} \, sign(\omega)}{|\omega|} \tag{3.8}$$

This is also caused by a lower limit of inverter output voltage then the theoretical value 3.7, since the duty cycles are limited in the range $0.05 \div 0.95$.

3.3 MTPV logic

After reaching the voltage limit with the flux-weakening logic, it is not convenient to maintain the maximum current. Therefore the current amplitude is reduced along a specific value of load angle δ, which is called δ_{max}. This concept is the base of the MTPV logic. In order to obtain this limit angle, it is necessary to express the torque as a function of only fluxes as first step. Starting from the magnetic equation of the electrical machine, the currents are expressed as a function of fluxes:

$$\begin{bmatrix} \lambda_d \\ \lambda_q \end{bmatrix} = \begin{bmatrix} L_{dd} & L_{dq} \\ L_{qd} & L_{qq} \end{bmatrix} \begin{bmatrix} i_d \\ i_q \end{bmatrix} + \begin{bmatrix} 0 \\ -\lambda_M \end{bmatrix} \tag{3.9}$$

$$\begin{aligned} i_d &= \frac{L_{dq}\left(\lambda_q + \lambda_M\right) - L_{qq}\,\lambda_d}{{L_{dq}}^2 - L_{dd}\,L_{qq}} = K_1\left(\lambda_q + \lambda_M\right) - K_2\,\lambda_d \\ i_q &= \frac{L_{dq}\,\lambda_d - L_{dd}\left(\lambda_q + \lambda_M\right)}{{L_{dq}}^2 - L_{dd}\,L_{qq}} = K_1\,\lambda_d - K_3\left(\lambda_q + \lambda_M\right) \end{aligned} \tag{3.10}$$

In this case the tensor of apparent inductances is utilised. Then the equations (3.10) are substituted in the torque expression, obtaining:

$$T = \frac{3}{2}\,p\left(K_1\,{\lambda_d}^2 - K_3\,\lambda_d(\lambda_q + \lambda_M) - \lambda_q\,K_1\left(\lambda_q + \lambda_M\right) + K_2\,\lambda_d\,\lambda_q\right) \tag{3.11}$$

The fluxes in dq-axes are expressed as a function of the flux amplitude and load angle, obtaining:

$$T = \frac{3}{2}\,p\,\lambda\left(K_1\,\lambda\cos(2\delta) + \lambda\,(K_2 - K_3)\frac{1}{2}\,sin(2\,\delta) - \lambda_M\big(K_3\,cos(\delta) + K_1\,sin(\delta)\big)\right) \tag{3.12}$$

In order to find the limit load angle δ_{max}, the torque is derived with respect to the load angle and imposed equal to zero. Due to the cross saturation present in this motor, the terms K_1 , K_2 and K_3 are variable according to currents, thus to fluxes. Consequently the limit of load angle δ_{max} is dependent on fluxes. For this reason, every control routine it is evaluated employing a LUT, which is an array composed by maximum value of load angle δ_{max} and it is associated to an evenly spaced array of flux amplitude values. The same process, previously described in Sec. 3.1, is applied to obtain the requested limit of load angle δ_{max}.

There is a tight relationship between the current in q_s-axis and the load angle, specifically the limitation of the current in q_s-axis leads to a limitation of the load angle [18]. Therefore a current limitation is introduced and it is added to the existing one owed to the inverter limit, as it is shown in Fig. 3.6.

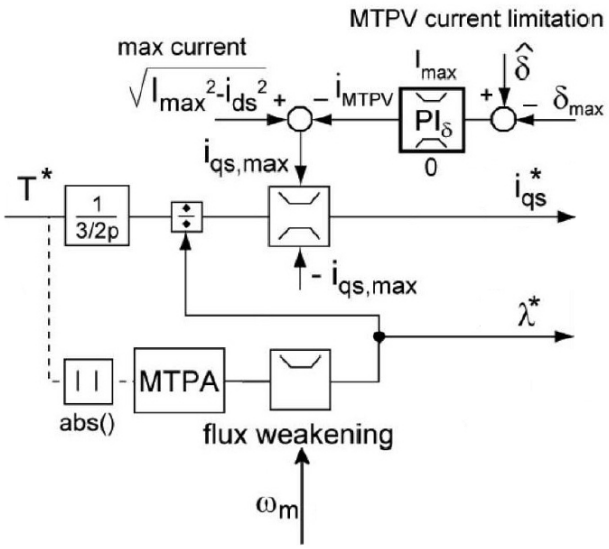

Figure 3.6: Scheme of the generation of references with the addition of flux-weakening and MTPV logic

The MTPV current limitation i_{MTPV} is subtracted from the inverter current limit, which is evaluated as:

$$i_{qs,inv-limit} = \sqrt{{I_{max}}^2 - {i_{ds}}^2} \tag{3.13}$$

where I_{max} is the maximum current that the inverter can provide.
This MTPV current limitation i_{MTPV} is calculated as output of a PI regulator, whose input is the difference between the estimated load angle δ and the limit δ_{max}. The output of the PI regulator is limited to I_{max} and to zero in order to produce an output only if the estimated load angle is higher than the limit δ_{max}.

The tuning of the PI regulator can be executed analysing the following block scheme, which is derived simplifying the scheme represented in Fig. 3.2:

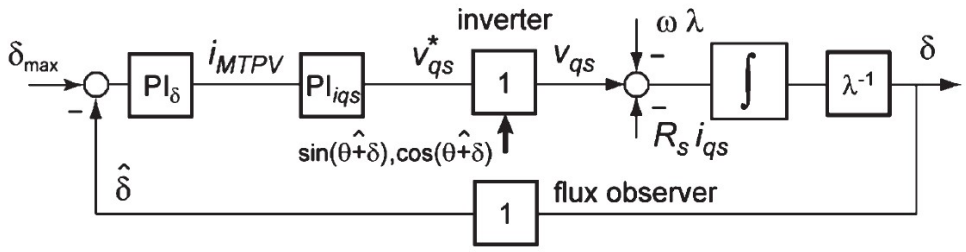

Figure 3.7: Simplified scheme highlighting the load angle regulation

The close-loop bandwidth of this scheme is equal to:

$$\omega_{bw,\delta} = \frac{k_{p,\delta}\, k_{p,iqs}}{\lambda} \tag{3.14}$$

where $k_{p,\delta}$ and $k_{p,iqs}$ are the proportional gains of the load angle and current regulators. The proportional gain of the load angle regulator can be evaluated as:

$$k_{p,\delta} = \frac{\omega_{bw,\delta}\, \lambda}{k_{p,iqs}} \tag{3.15}$$

The bandwidth is imposed, while the flux amplitude considered is the minimum value which is at maximum speed in order to not have a bandwidth higher than the imposed one.

3.4 Flux and current closed loop

The reference values of current in q_s-axis and flux amplitude are employed in a respective regulator. The input of the current regulator is the difference between the reference value and the measured one and its output is the reference voltage inq_s-axis. On the other hand the input of the flux regulator is the difference between the reference value and the observed one (see Sec. 3.5) and its output is the reference voltage in d_s-axis.

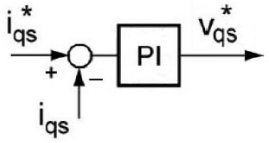

Figure 3.8: Regulator of the current loop

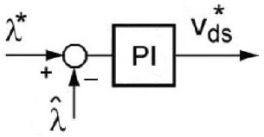

Figure 3.9: Regulator of the flux loop

These regulators are both composed by a proportional part and an integral one, the total gain is thereby equal to:

$$k_{tot} = k_p + \frac{k_i}{s} \tag{3.16}$$

where k_p is the proportional gain and k_i is the integral one.The tuning of these gains is different for the current loop and the flux one.
In the first case they are:

$$\begin{aligned} k_{p,current} &= \omega_{bw,current}\,(L_{d,sat} + L_{\sigma s}) \\ k_{i,current} &= k_{tune,current} \cdot \omega_{bw,current} \cdot k_{p,current} \end{aligned} \tag{3.17}$$

where

- $\omega_{bw,current}$ is the bandwidth of the current loop, which is imposed by the user;
- $L_{d,sat}$ is the inductance in d-axis when saturation occurs;
- $L_{\sigma s}$ is the stator leakage inductance;
- $k_{tune,current}$ is a tune gain lower than one owing to the necessity of respecting $k_{i,current} < \omega_{bw,current} \cdot k_{p,current}$.

In order to tune them, the bandwidth and the tune gain is changed until the desired response is obtained. In the second case they are:

$$\begin{aligned} k_{p,flux} &= \omega_{bw,flux} \\ k_{i,flux} &= k_{tune,flux} \cdot \omega_{bw,flux} \cdot k_{p,flux} \end{aligned} \tag{3.18}$$

where

- $\omega_{bw,flux}$ is the bandwidth of the flux loop, which is imposed by the user;
- $k_{tune,flux}$ is a tune gain lower than one owing to the necessity of respecting $k_{i,flux} < \omega_{bw,flux} \cdot k_{p,flux}$

The tuning of these gain is done in the same way as the current one.

The reference voltages in $d_s q_s$-axes are transformed into the reference voltages in *abc*-frame. This process is done through the rotational transform, which employs the sum of the load angle and the rotor angular position as rotation angle, and the Park transform. The reference voltages in *abc*-frame are utilised to evaluate the duty cycles as shown in Sec. 2.2.

3.5 Flux-observer

As mentioned above, the flux amplitude and the load angle δ are necessary for some blocks. These two quantities are evaluated through a flux observer, whose scheme is the following:

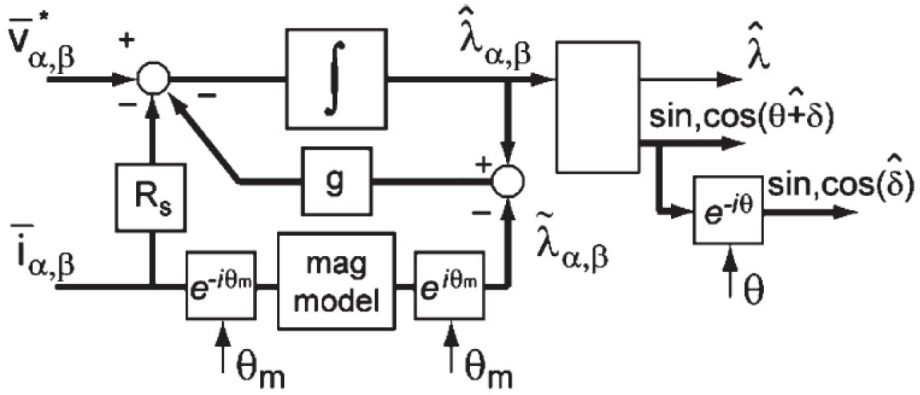

Figure 3.10: Scheme of the flux observer

The flux observer is based on the combination of two flux estimators, whose aim is to estimate a quantity through the machine model. The quantity estimated by both is the flux in $\alpha\beta$-axes.

The first one is an estimator founded on the stator equations. The flux is obtained as the integral of the electromotive force:

$$\tilde{\lambda}^s_{\alpha\beta} = \frac{\mathbf{v}_{\alpha\beta} - R_s\,\mathbf{i}_{\alpha\beta}}{s} \tag{3.19}$$

where the voltages in $\alpha\beta$-axes employed are the reference ones of the previous ISR, while the currents in $\alpha\beta$-axes are the measured ones of the ongoing ISR.

The second one is an estimator founded on the magnetic model of the electrical machine, previously analysed in 2.3. This magnetic model is applied in dq-axes and then the rotational transform is used to obtain the flux in $\alpha\beta$-axes:

$$\mathbf{i}_{\alpha\beta} = A(-\theta)\,\mathbf{i}_{dq}$$

$$\mathbf{i}_{dq} \xrightarrow{LUT} \tilde{\lambda}^i_{dq} \tag{3.20}$$

$$\tilde{\lambda}^i_{\alpha\beta} = A(\theta)\,\tilde{\lambda}^i_{dq}$$

where the currents in $\alpha\beta$-axes are the measured ones. As it is possible to notice the the flux in dq-axes is obtained through flux maps of the electrical machine given as LUT.

In order to combine the two outputs of estimators, it is necessary to introduce a feedback in the scheme shown above. It is equal to a gain g multiplied with the difference between the observed flux (output of the flux-observer) and the estimated one with the second type of estimator. This feedback is subtracted to the numerator of the equation 3.19 in the first type of estimator, thus it is integrated leading to obtain the observed flux in $\alpha\beta$-axes.
The global transfer function is:

$$\hat{\lambda}_{\alpha\beta} = \frac{s}{s+g}\left(\frac{\mathbf{v}_{\alpha\beta} - R_s\,\mathbf{i}_{\alpha\beta}}{s}\right) + \frac{g}{s+g}\,\lambda^{\mathbf{i}}_{\alpha\beta} \tag{3.21}$$

As it is possible to highlight the first type of estimator is multiplied with a high-pass filter, while the second type of estimator is multiplied with a low-pass filter. Therefore the first type is valid at high speed and the second one at low speed. These two filter contains the feedback gain g which determines the crossover angular speed at which there is the transition from one estimator to the other.

Finally, the necessary flux amplitude and its angular position are evaluated as:

$$\hat{\lambda} = \sqrt{\hat{\lambda}_\alpha^2 + \hat{\lambda}_\beta^2} \tag{3.22}$$

$$cos(\theta + \delta) = \frac{\lambda_\alpha}{\hat{\lambda}} \qquad\qquad sin(\theta + \delta) = \frac{\lambda_\beta}{\hat{\lambda}} \tag{3.23}$$

Therefore, the load angle is obtained subtracting from the angular position of the stator flux the rotor position. This difference is approximated with the sine of the difference.

3.6 Results

The implemented control method has been tested in order to analyse its functioning and tune the necessary parameters. The test is done employing the model previously generated and analysed.
The test parameters are the following:

- Battery voltage equal to 300 V, considered constant due to the short duration of the simulation;
- IGBT forward voltage equal to 0.7 V and IGBT on-state resistance equal to 10 $m\Omega$;
- Free-wheeling diode forward voltage equal to 0.7 V and free-wheeling diode on-state resistance equal to 10 $m\Omega$;
- Stator resistance equal to 17.06 $m\Omega$;
- Stator leakage inductance equal to 2 μH;
- Pole pair equal to 3;
- Magnet flux equal to 0.03515 Wb;
- Flux maps equal to

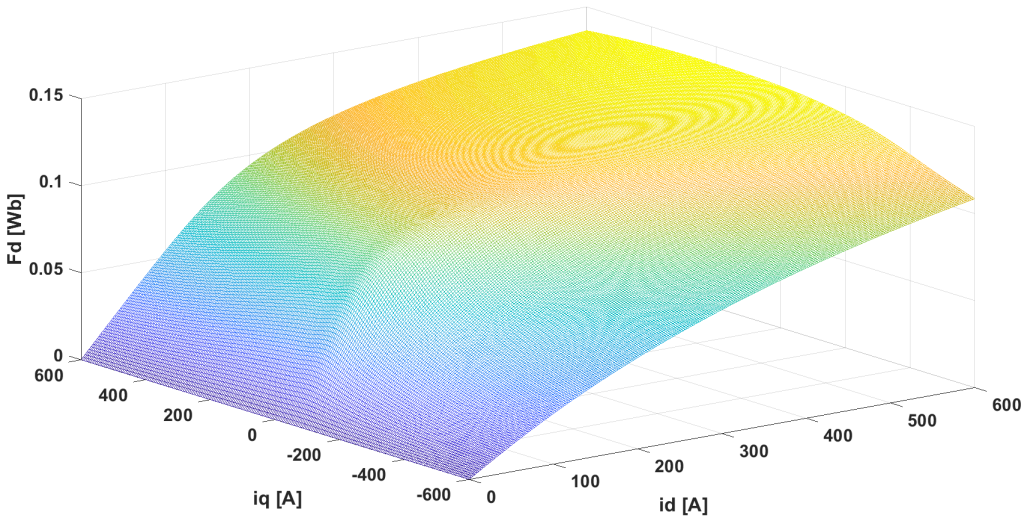

Figure 3.11: Flux map in d-axis

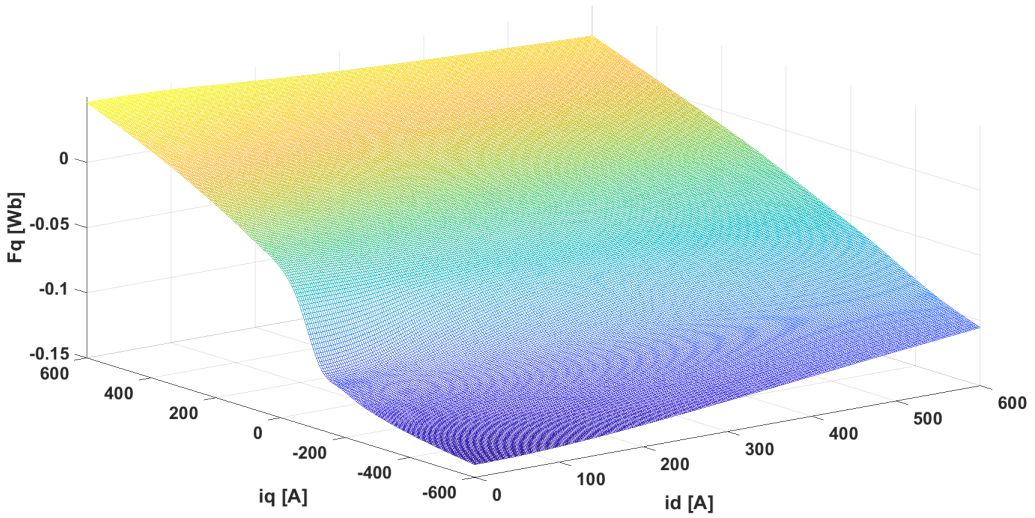

Figure 3.12: Flux map in q-axis

- Equivalent inertia seen from the electrical machine equal to 1.75 $kg \cdot m^2$ in order to satisfy this condition: accelerating from 0 to 100 km/h in 9 seconds.

The test conditions and the performance limits are set arbitrarily to test only the control method and they are not disclosed due to confidentiality issue.

3.6.1 Verification of the Flux-Observer

Firstly the feedback gain g of flux observer is tuned in order to make the flux estimation more accurate as possible.
The value found out is equal to $g = 2\pi 180\ rad/s$. The flux observer is tested both at low speed, 50 rpm, and at high speed, 6000 rpm. In the first case only the flux estimator deriving from the magnetic model works, while in the second one only the flux estimator deriving from the stator equations works.
As it is possible to see in Fig. 3.13, 3.14, 3.16 and 3.17, the flux is correctly estimated both at low speed and at high speed. The maximum error committed at low speed for the flux in in α-axis is equal to (Fig. 3.15):

$$\lambda_{error} = \lambda_{\alpha,plant} - \hat{\lambda}_{\alpha} = 0.1189 - 0.1185 = 4 \cdot 10^{-4}\, Wb \tag{3.24}$$

Therefore the relative percentage error is nearly 0.3%. This error is equal for the flux in β-axis at low speed. In the high speed case, the maximum error committed for the flux in in α-axis is equal to $1.4 \cdot 10^{-3}\, Wb$, thus a relative percentage error of 1.6%. Furthermore it is possible to notice the difference between the observed flux and the plant one in the first time interval, due to the fact that the motor control starts working only from $t = 0.032\, s$. In Fig. 3.16 and 3.17 it is possible to highlight the delay of the observed flux, because of the use of previous step quantities, and its discretization caused by the control working only every ISR.

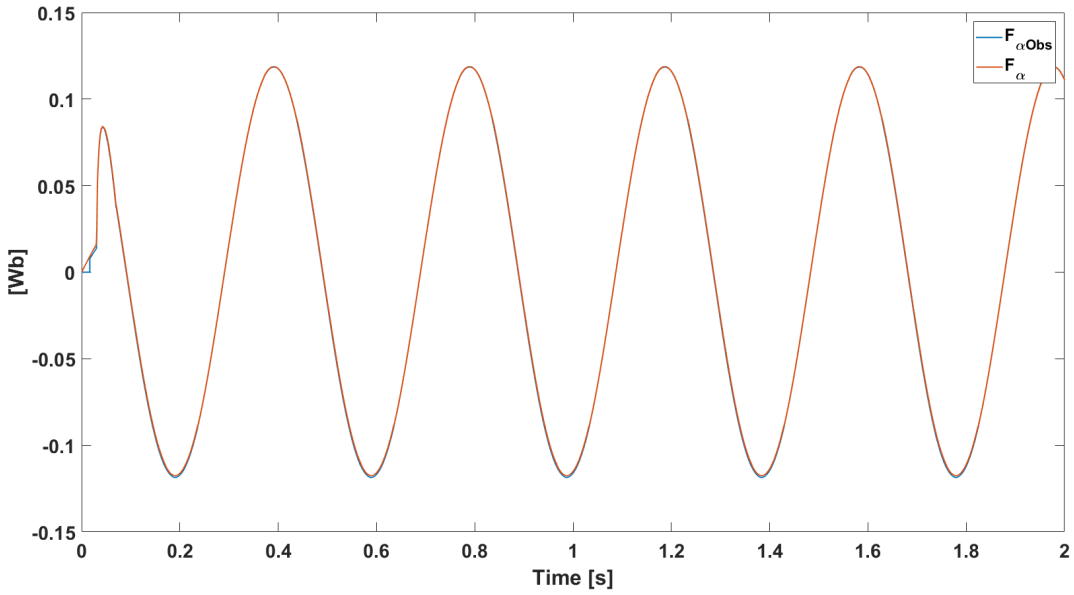

Figure 3.13: Plant flux in α-axis and observed flux in α-axis at low speed

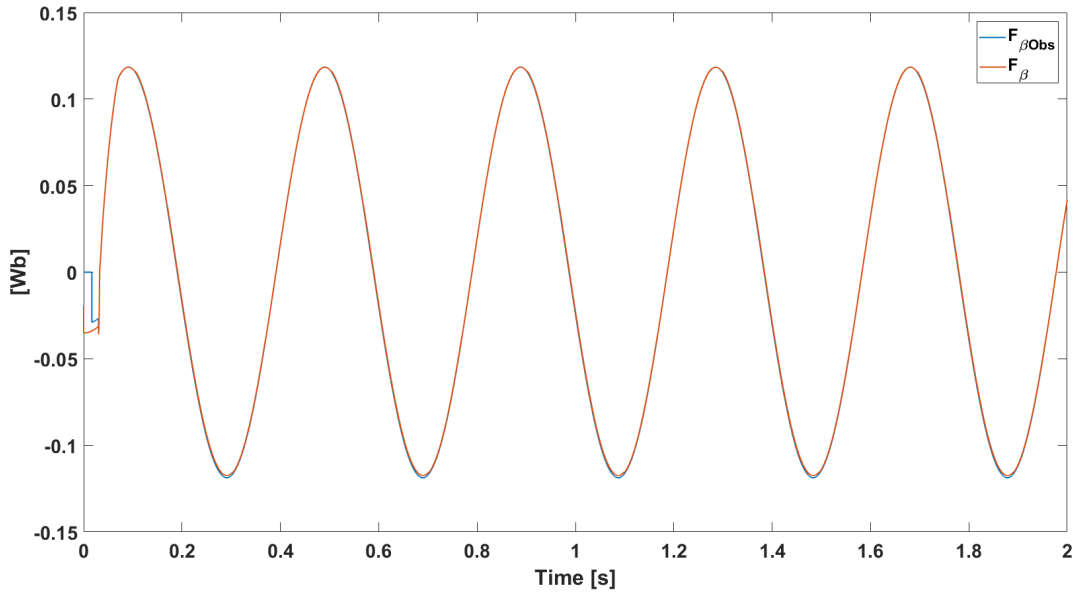

Figure 3.14: Plant flux in β-axis and observed flux in β-axis at low speed

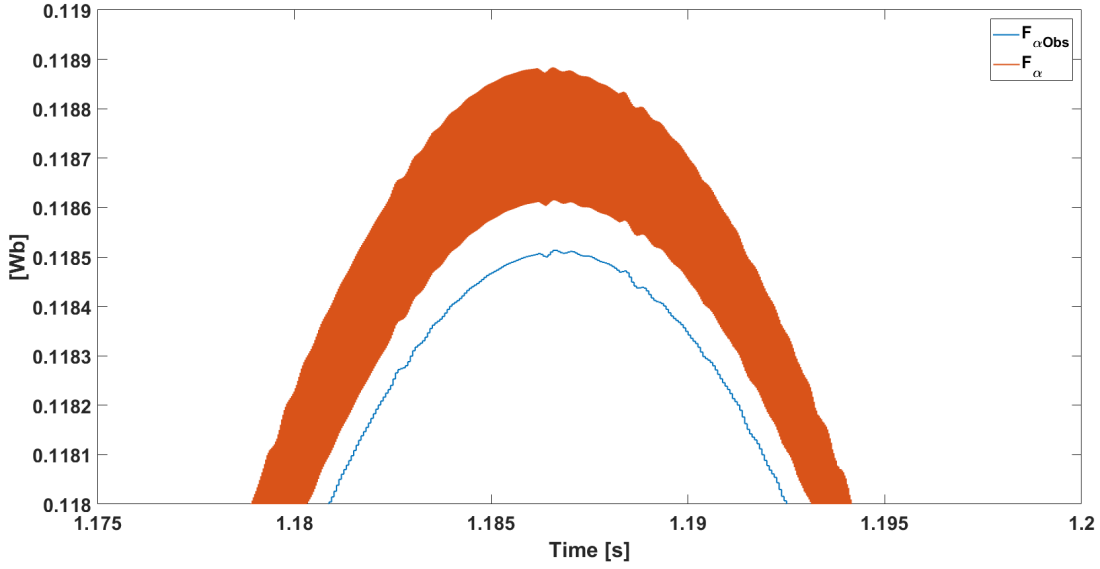

Figure 3.15: Detail of plant flux in α-axis and observed flux in α-axis at low speed

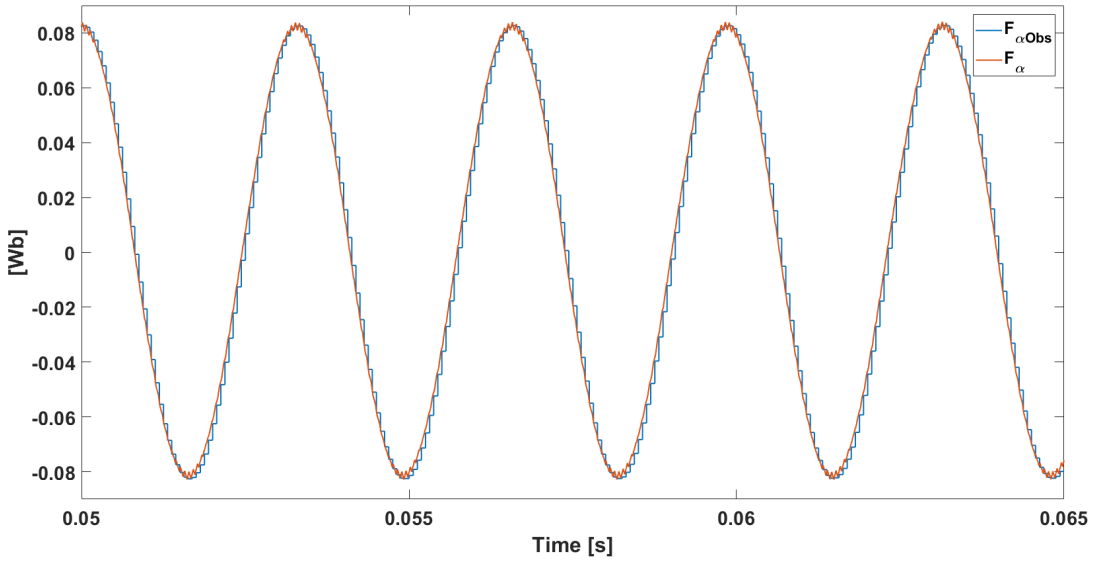

Figure 3.16: Plant flux in α-axis and observed flux in α-axis at high speed

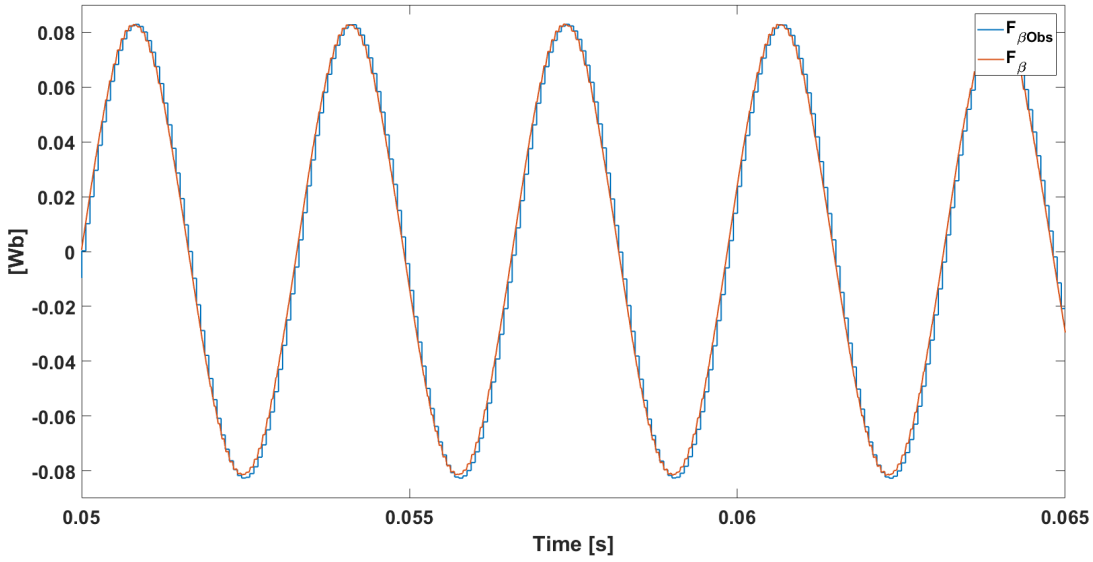

Figure 3.17: Plant flux in β-axis and observed flux in β-axis at high speed

3.6.2 MTPA operation

The MTPA logic is tested applying a torque step at the maximum torque obtainable, which is equal to $200Nm$ for the current analysis. The plant torque is a ramp, represented in Fig. 3.18, and the respective MTPA locus in the current plane and in the flux plane are represented in 3.19 and 3.20.

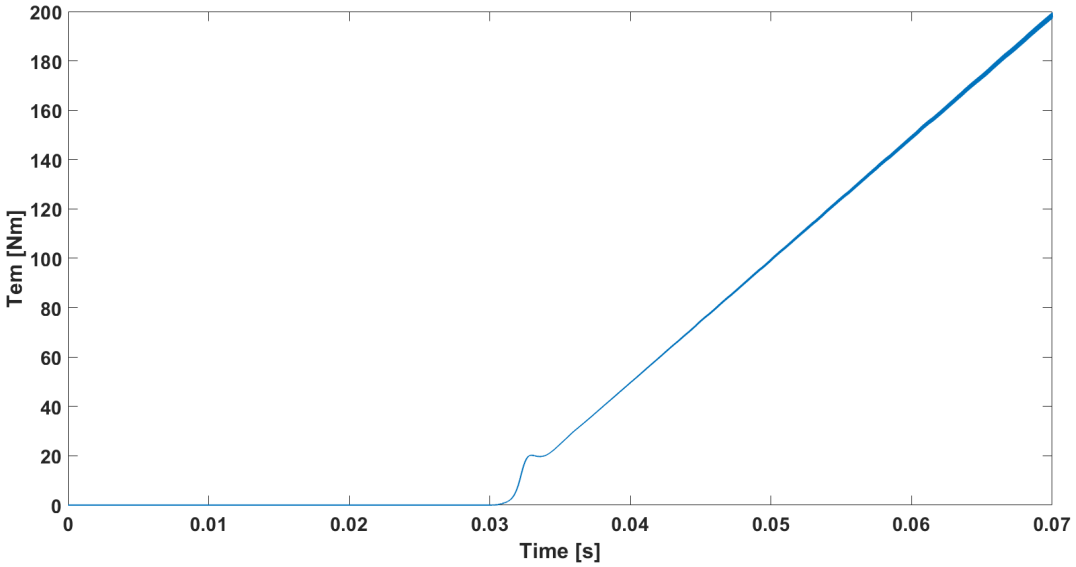

Figure 3.18: Torque evolution in MTPA test

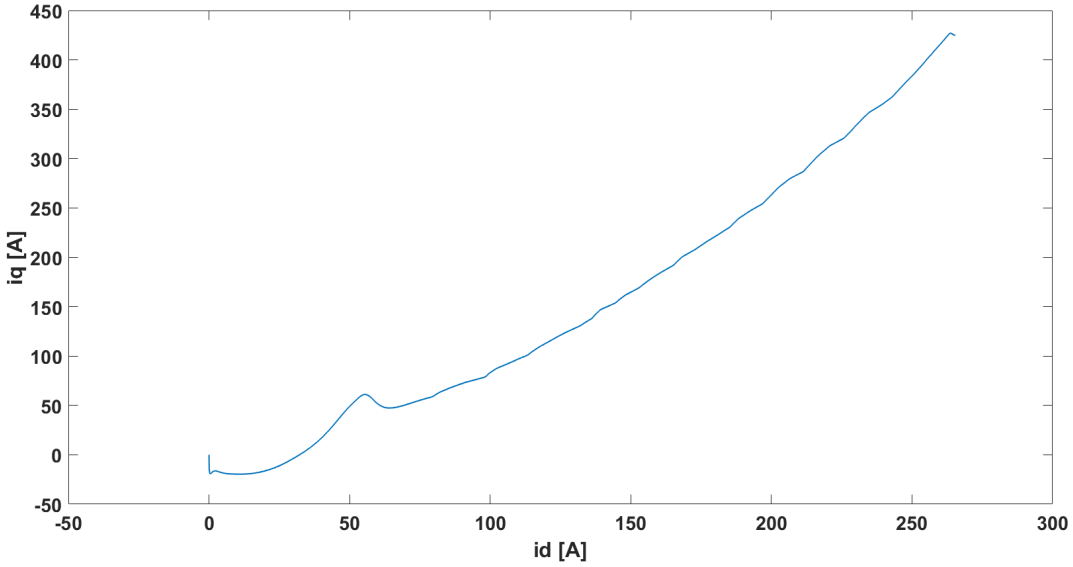

Figure 3.19: Currents in dq-axes following MTPA algorithm

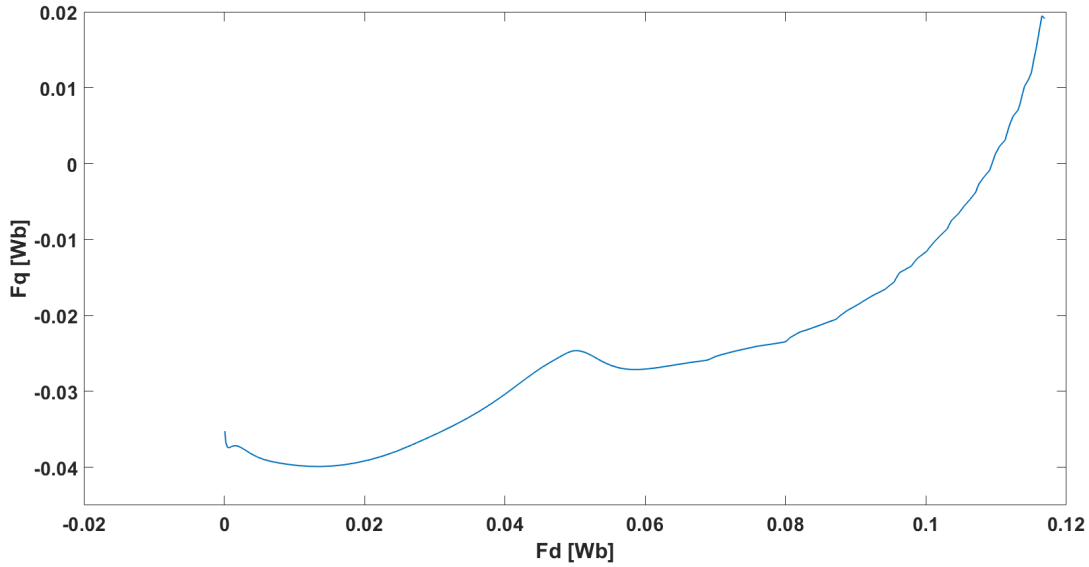

Figure 3.20: Fluxes in dq-axes following MTPA algorithm

The initial part of the obtained MTPA locus has some errors due to the initial response of the motor control, which leads to negative currents at the motor start. Moreover the starting value of the MTPA flux curve is equal to the magnet flux: it is directed along the negative semi-axis q and equal to $0.0351\,Wb$.

3.6.3 Flux-weakening and MTPV operation

The MTPV logic is tested applying a torque step at the maximum torque obtainable and lowering the equivalent inertia seen by the electrical machine in order to reduce the simulation time. The plant torque and speed are represented respectively in Fig. 3.21 and 3.22.

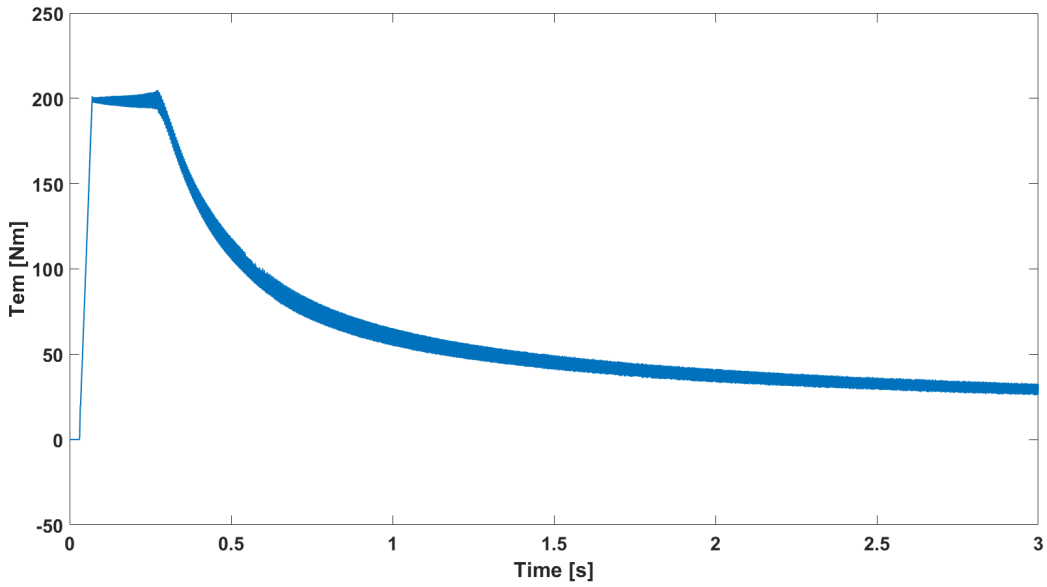

Figure 3.21: Torque evolution in MTPV test

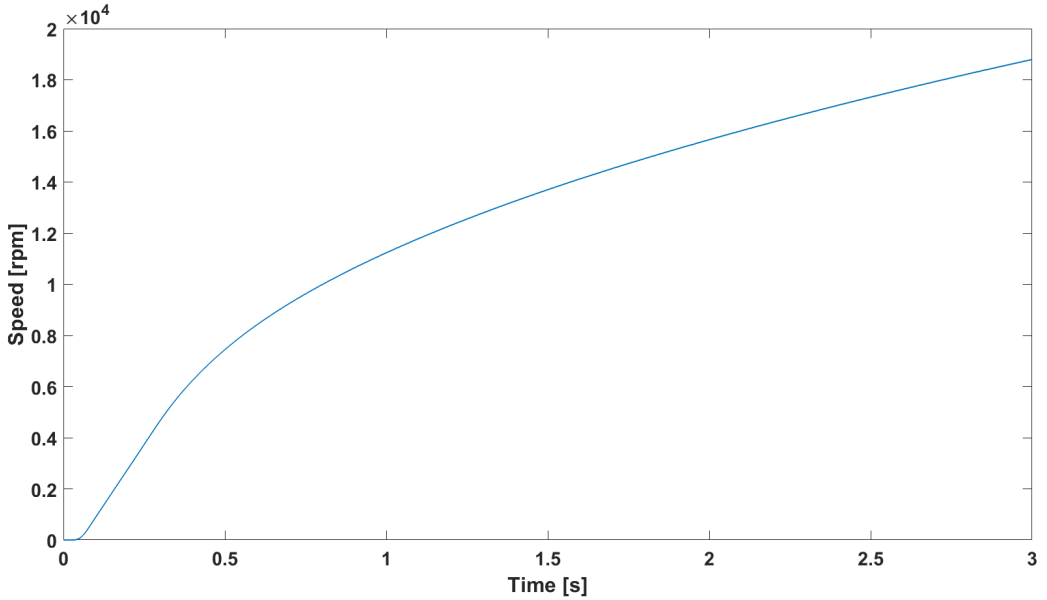

Figure 3.22: Speed evolution in MTPV test

The torque is limited to the maximum obtainable value until the flux-weakening operation at the base speed of nearly 4160 rpm, at which the maximum voltage is applied as shown in Fig. 3.23 where the moving average of a-phase voltage is represented until 0.5 s.

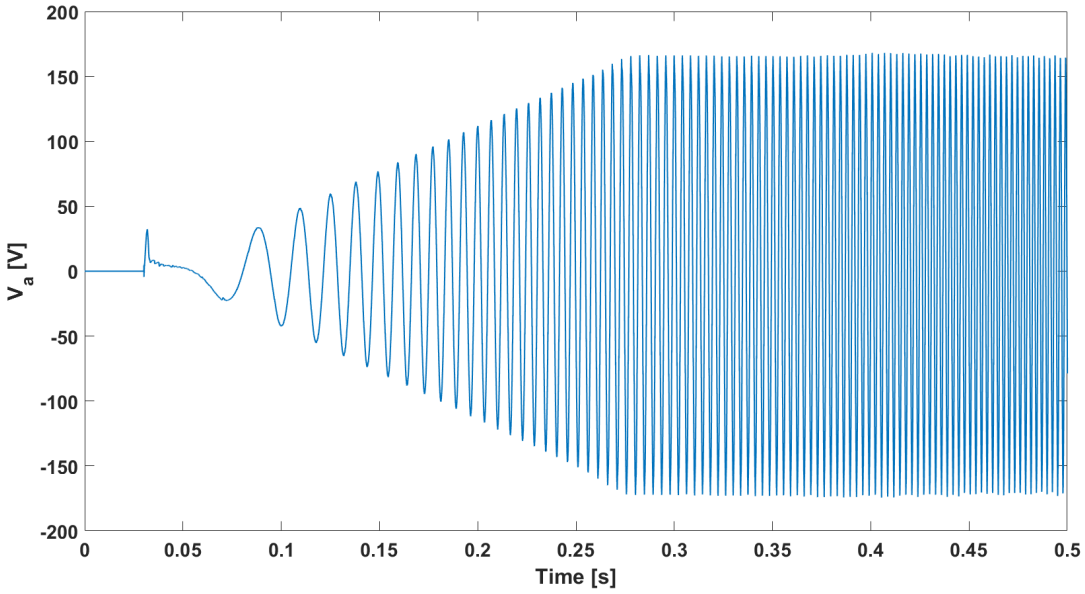

Figure 3.23: Phase a voltage evolution in MTPV test

The maximum speed reached in the current simulation is 18690 rpm and the control has become less stable as it is possible to highlight from the ripple on the controlled quantities, due to it is going near to its limits. Nonetheless the control, as presented in this chapter, cannot work until this speed due to its instability. This instability is caused by the delay of actuation that becomes significant in terms of electrical degree of the fundamental harmonics. For this reason a phase-advancing on the reference voltage is implemented, which consists of a rotational transform of an angle equal to:

$$\delta_{ph_{advance}} = p\,\omega_{motor}\,T_s \tag{3.25}$$

where

- p is the pole pair of the electrical machine;
- ω_{motor} is the mechanical speed of the electrical machine;
- T_s is the switching period.

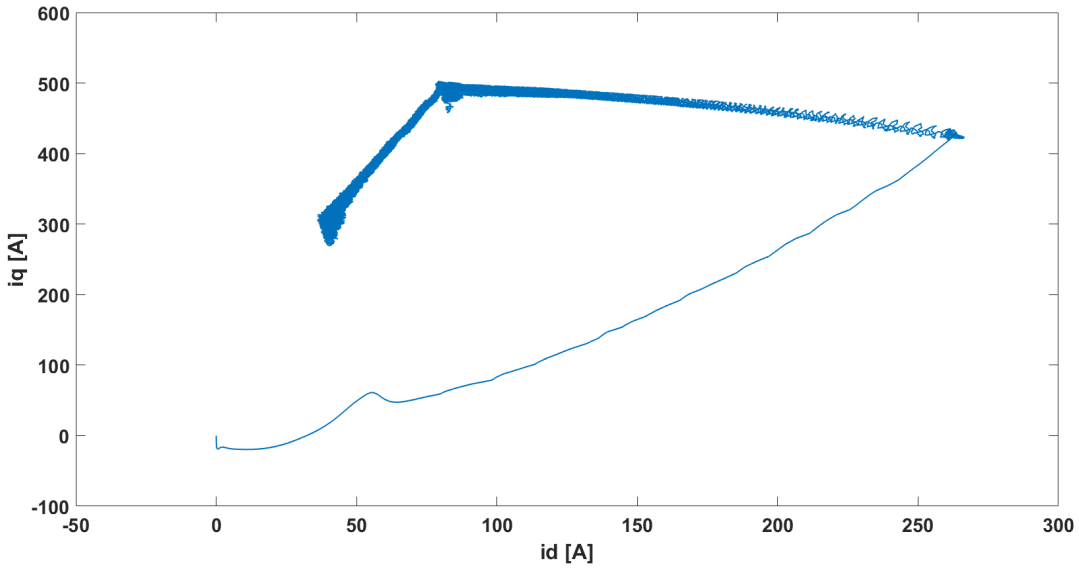

Figure 3.24: Currents in dq-axes following MTPA, flux-weakening and MTPV algorithm

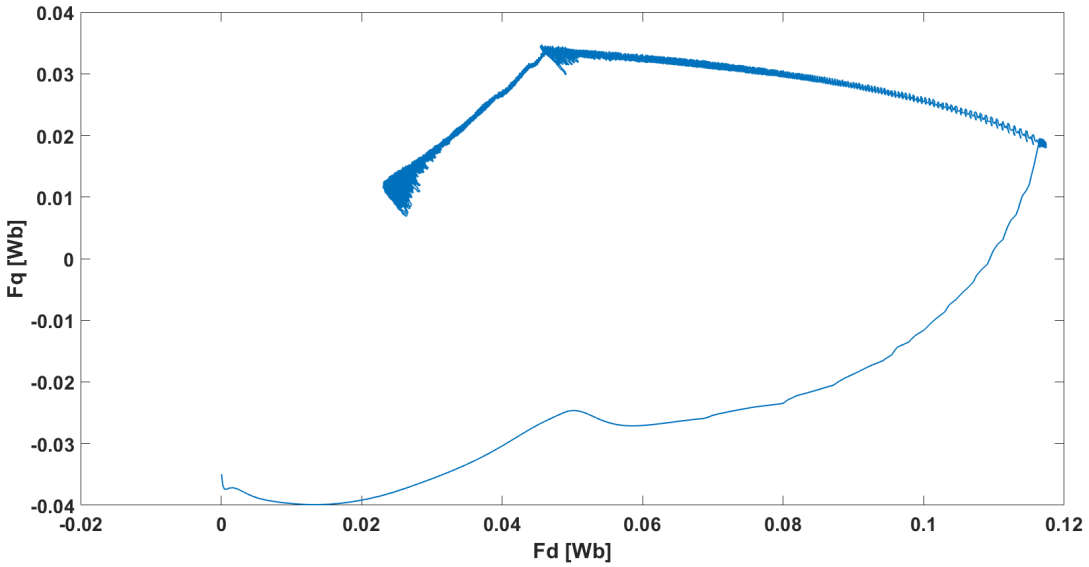

Figure 3.25: Fluxes in dq-axes following MTPA, flux-weakening and MTPV algorithm

In the MTPV operation the load angle is limited to the maximum value equal to $\delta_{max} = 126.9°$, due to the low permanent magnet flux per unit and the high saliency of the electrical machine under study. Moreover, in the flux-weakening operation the current is limited to the maximum allowable value, which is $500\,A$.

Chapter 4

High level control

The innovative electromechanical actuator needs specific conditions to be actuated. These conditions have to be monitored in order to activate it when necessary, such as when safety actions are required. Furthermore this actuator can work only when the inverter and electrical machine are switched off, thus a further control is implemented. This type of monitoring combined with the additional motor control is called high level control due to its asynchronous behaviour with respect to the principal motor control previously analysed. The logic of this high level control is shown in Fig. 4.1.

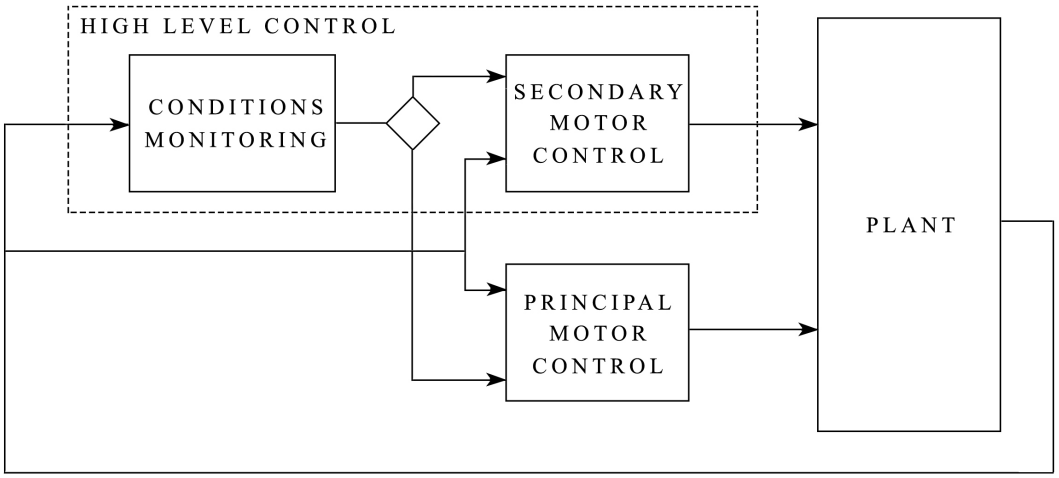

Figure 4.1: Scheme of the plant whole control

The principal motor control is run until a trigger coming from the conditions monitoring arrives, thereafter the secondary motor control starts working. When the inverter and the electrical machine are switched off, the electromechanical actuator is activated. After its successful execution, thus when all is reported in safety conditions, the inverter and the electrical machine are switched on again, so the secondary motor control ends up, and the principal motor control resumes work.

4.1 Conditions monitoring

As mentioned above, specific conditions have to be monitored in order to trigger when necessary the secondary motor control and the operations of the electromechanical actuator. In particular these conditions are related to two parameters of the electrical machine:

- Temperature;
- Equivalent back-emf.

These parameters and the related conditions will be analysed in order to understand their significance for the process. The method through they are evaluated will be analysed in chapter 5.

4.1.1 Temperature

The temperature is a relevant parameter that influences many quantities in the electrical machine, in particular material-based quantities as electrical resistivity. In this case the temperature under interest is the rotor one due to its influence on the magnetic characteristic of permanent magnets, which are positioned inside the rotor (Fig. 2.13). The useful part of the hysteresis loop for permanent magnet is the second quadrant:

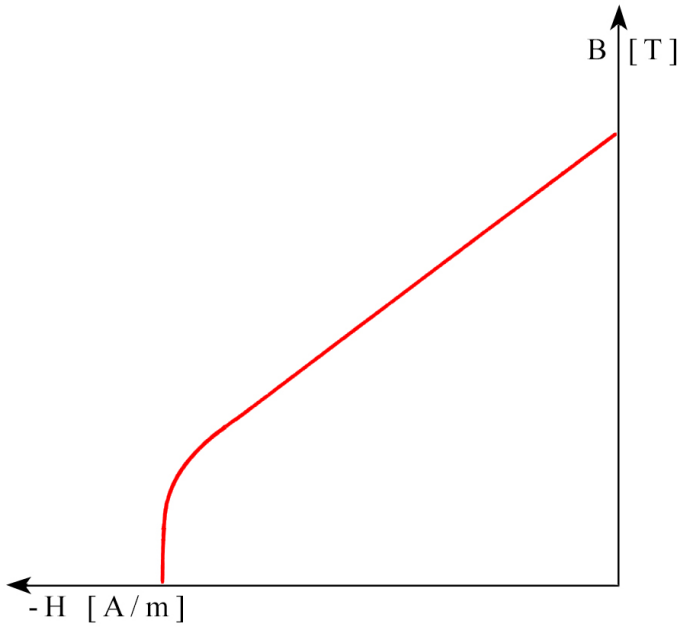

Figure 4.2: General magnetic characteristic in the second quadrant

This is called demagnetization curve and it is usually where the permanent magnet works. The working point has to be necessarily above the point where slope changes, called knee point, because under it the magnet goes through an irreversible process of demagnetization, decreasing its magnetic induction.

The electrical machine can be analysed with a simplified magnetic circuit. It is composed of:

- a single winding with N turns in which a current i flows;
- a permanent magnet with dimensions equal to l_m x S_m;
- an air gap with dimensions equal to l_g x S_g.

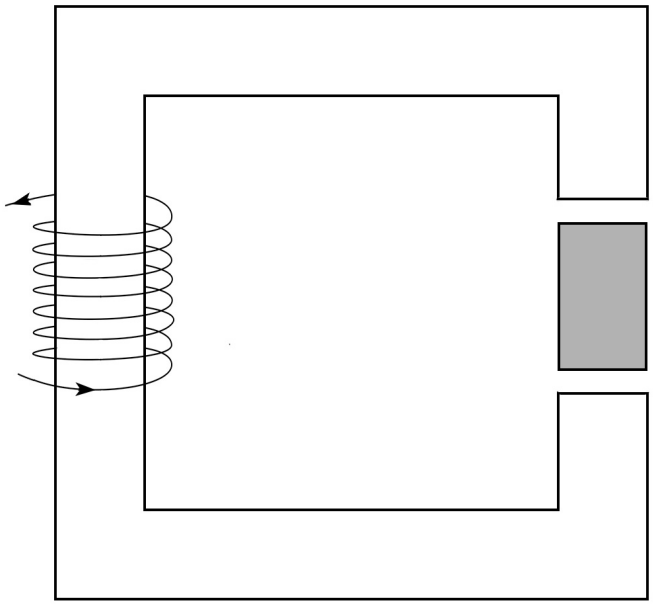

Figure 4.3: Simplified magnetic circuit

The equation associated to this circuit are:

$$H_m\, l_m = H_g\, l_g + N\, i$$

$$B_m\, S_m = B_g\, S_g \tag{4.1}$$

$$B_g = \mu_0\, H_g$$

Resolving them, it is possible to obtain:

$$H_m = \frac{B_m\, S_m\, l_g}{\mu_0\, S_g\, l_m} + \frac{N\, i}{l_m} \tag{4.2}$$

where B_m and H_m are respectively the magnetic flux density or induction and the magnetic field strength of the permanent magnet. The working point is given by the intersection between the permanent magnet characteristic and 4.2:

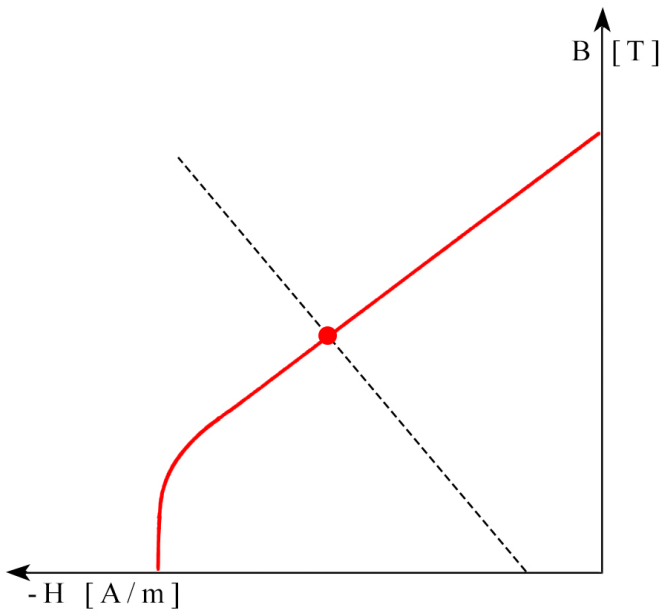

Figure 4.4: Working point of permanent magnet in the second quadrant

As it is possible to notice the working point varies according to the air gap dimensions and current value. Furthermore, the magnetic characteristic is influenced by the magnet temperature, as shown for NdFeB magnet [20]:

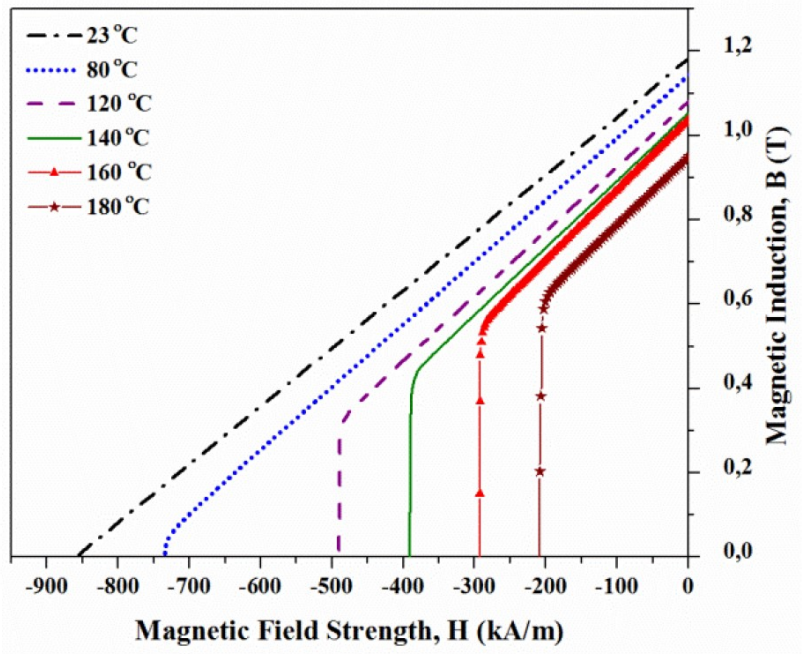

Figure 4.5: Magnetic characteristic of NdFeB with varying temperature

Therefore, on equal working conditions an increase of temperature initially lead to a performance reduction of the electrical machine, then permanent magnets may suffer risks of demagnetization under the condition of high temperature [21].

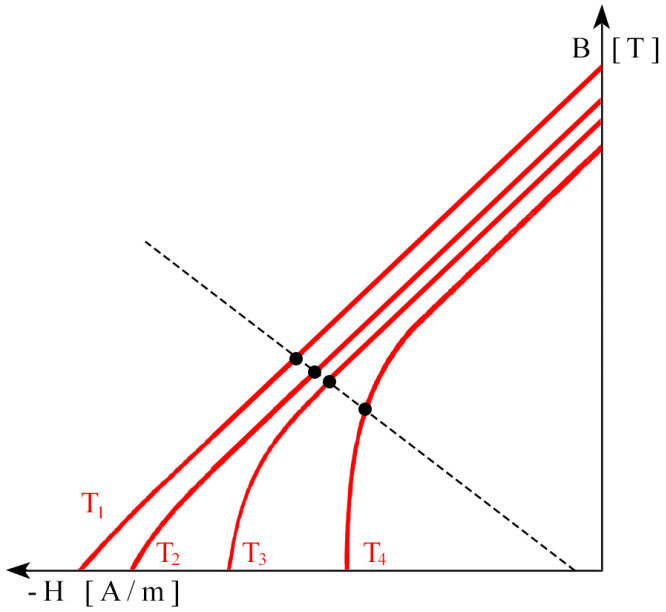

Figure 4.6: Working point in the magnetic characteristic with varying temperature

For these reasons temperature effects on permanent magnet are considered in models during machine design. Nonetheless, this electrical machine is a highly performing motor which could work in extreme conditions. Therefore the rotor temperature has to be constantly monitored in order to avoid the demagnetization phenomenon. Usually electrical machines are over-dimensioned to ensure continuous safe operations, although this can be avoided if precise temperature estimation is present.

4.1.2 Equivalent back-emf

The main condition under which the electromechanical actuator can work is that the inverter and the electrical machine are switched off. The simple operation of switching off all the inverter IGBT is not sufficient due to a phenomenon called Uncontrolled Generation (UGC). This phenomenon is typical of unsafe situations, such as when IGBT commands are suddenly lost during field weakening high speed operation [23]. The UGC could be really dangerous for battery, inverter and other relevant components, due to the high increase of currents and voltages [24]. As mentioned above, the inverter IGBT are switched off, whereas the free-wheeling diodes of each IGBT cannot be controlled in order to be switched off, thus they generate an Uncontrolled Rectifier (UR), shown in Fig. 4.7.

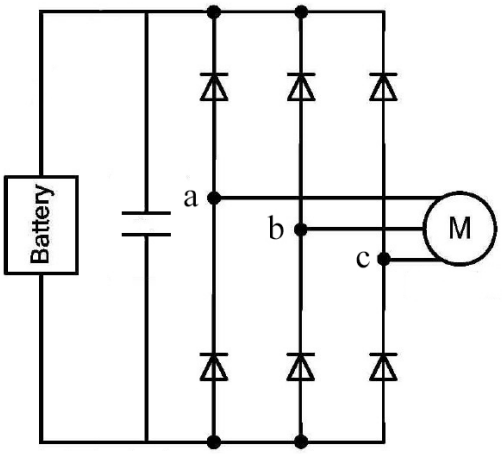

Figure 4.7: Electrical scheme of the uncontrolled rectifier

Whenever only one of the line-to-line voltage is higher than the total voltage seen at the outlet of the uncontrolled rectifier, the respective two free-wheeling diode are switched on and current starts flowing. In details it is described as [25]:

$$V_{in} = MAX\left(V_{ab}, V_{ba}, V_{ac}, V_{ca}, V_{bc}, V_{cb}\right)$$

$$\begin{cases} V_{out} = V_{in} - 2\,V_{on} & if\ (V_{in} - 2\,V_{on}) > V_{bat} \\ V_{out} = V_{bat} & if\ (V_{in} - 2\,V_{on}) \leq V_{bat} \end{cases} \tag{4.3}$$

Where:

- V_{in} represents the input voltage of the uncontrolled rectifier;
- V_{on} is the threshold voltage of the free-wheeling diode;
- V_{bat} is the battery voltage.

Therefore when V_{in} is higher than $V_{bat} + 2\,V_{on}$, two diodes are switched on and the current flows back. The activated diodes varies according to the line-to line voltage, for example if $V_{ab} > V_{bat} + 2\,V_{on}$ the two diodes are shown in Fig. 4.8 and the current flows as shown in Fig. 4.8:

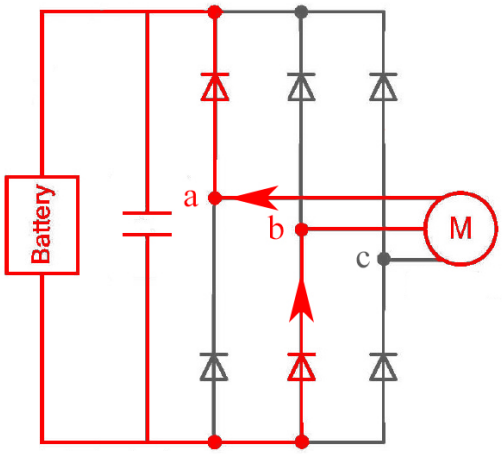

Figure 4.8: Flow back of current in the uncontrolled rectifier

For safety issues, there are many solutions that can be implemented in order to avoid the side effects of the UCG phenomenon, such as external protection circuit employed to bring down the DC-link voltage or an optimal design of the electrical machine [25]. Nonetheless in this case study the uncontrolled generation has to be avoided ex ante, for this reason the equivalent back-emf has to be constantly monitored.

4.2 Secondary motor control

The secondary motor control is a logic of control applied to the motor and not to the electromechanical actuator. Therefore it substitutes the principal one when a trigger from the conditions monitoring arrives. The logic is the following:

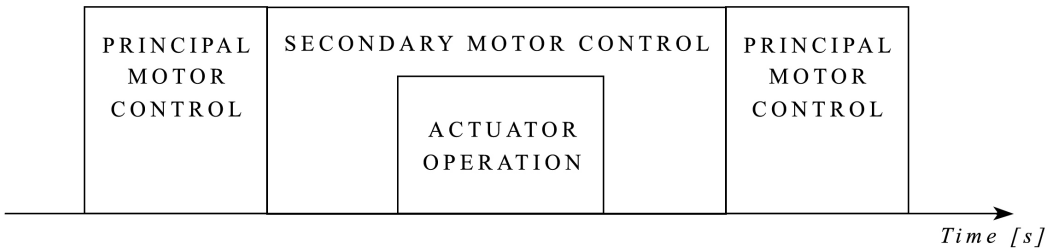

Figure 4.9: Time scheme of the plant whole control

This control is based on three different phases:

- switching off the electrical machine and the inverter;
- waiting for the actuator operations;
- switching on the electrical machine and the inverter, returning the control to the user (reference values).

This type of control can be done in two different ways:

- zero torque control;
- zero current control.

The first one is based on the same motor control previously analysed, while the second differs in some aspects.

4.2.1 Zero torque control

As mentioned above, this control is equal to the principal motor control. The difference stays in the reference values that are given to the control. When the trigger comes, the reference torque starts decreasing with a slope imposed by the user until it is equal to zero, as shown in Fig. 4.10.

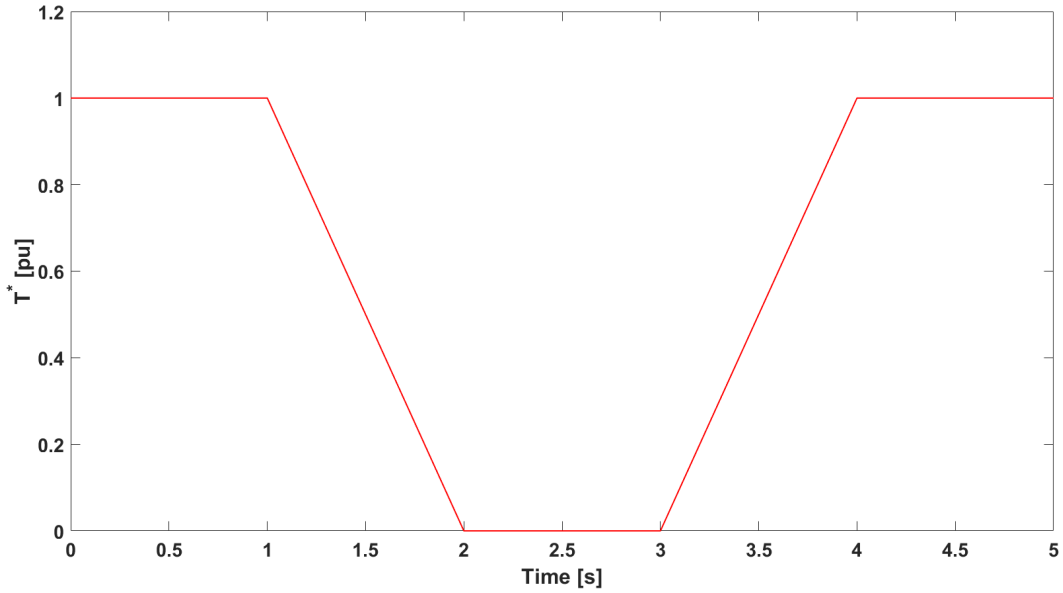

Figure 4.10: Value of reference torque during the secondary motor control

Thereafter the control verifies that the torque and the phase currents are below a respective determined threshold, again imposed by the user. When this occurs, the inverter is switched off. From this moment the electrical machine inductances start discharging, therefore the control checks when the currents are equal to zero. Once this happens, a signal is sent to the actuator thus it can operate. After its successful execution, a trigger is sent back to the control that switches on the inverter. The control waits until the transient is extinguished and then starts increasing with a slope the reference torque until it reaches the value imposed by the driver (Fig. 4.10), which it is not necessary equal to the starting one.

4.2.2 Zero current control

In this case the control is different from the principal motor control. The controlled quantities are directly the currents in dq-axes. Consequently a closed loop for both currents is introduced, whose input is the difference between the reference value and the measured one and its output is the reference voltage in the respective axis (Fig. 4.11 and 4.12).

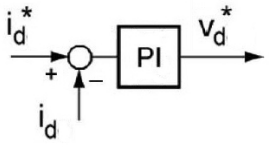

Figure 4.11: Regulator of the current loop in d-axis

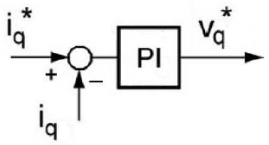

Figure 4.12: Regulator of the current loop in q-axis

When the trigger comes from the conditions monitoring, the reference currents in dq-axes starts decreasing with a respective slope imposed by the user until they are equal to zero, as shown in Fig. 4.13.

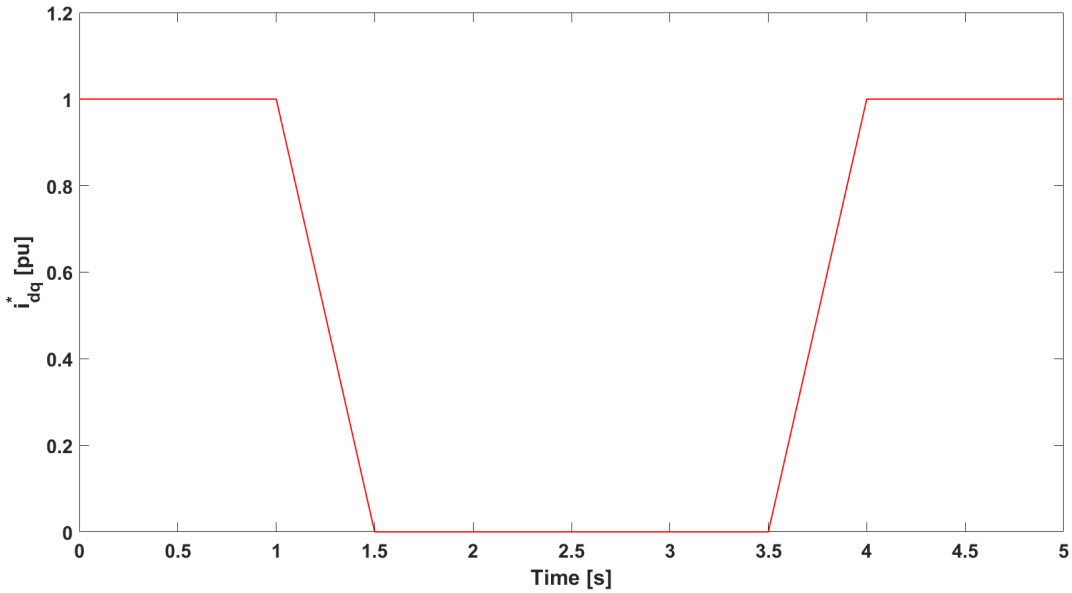

Figure 4.13: Value of reference currents in dq-axes during the secondary motor control

Successfully the control logic is equal to the previously analysed one, until the inverter is switched on. Then the control waits until the transient is extinguished and then starts increasing with a respective slope the reference currents until they reach the values equal to the respective ones corresponding to the torque imposed by the driver (Fig. 4.13), which it is not necessary equal to the starting one.

4.2.3 Control selection

Starting from the two possible solutions, they are analysed in order to find out the best suitable. The main differences are:

- the implementation with the principal motor control;
- the current values before the inverter is switched off.

The implementation of the first one is simple because only a change of reference torque has to be added together with the logic of switching off and on. The implementation of the second one is slightly complex than the previous one, due to the change of controlled quantities. Furthermore in the first type of control, after the torque decrease, the currents are not necessary equal to zero, while in the second one they are controlled to be equal to zero.
For the simplicity of implementation, the first type of control is chosen. After the torque decrease, the currents are not so high that even if they are suddenly interrupted generated, overvoltage are not significant.

4.3 Results

The high level control is tested in simulation in order to verify its functioning and accuracy, while the functioning of the electromechanical actuator is completely neglected. The test is done employing the model and the motor control previously generated and analysed. The test parameters for the electrical machine are the same of the test done for the motor control (see subsection 3.6). The other test parameters are the following:

- torque reference equal to the maximum obtainable of $200\,Nm$;
- since the operation time of the innovative actuator is variable and it is not of interest in this simulation, it is set quite low to be $0.3\,s$ in order to reduce the simulation time;
- initial speed equal to $0\,rpm$.

As mentioned above, the control applied is the zero torque control. The torque evolution is represented in Fig. 4.14 and it follows exactly the wanted one. When the trigger coming from the conditions monitoring arrives, at $1\,s$, the torque start decreasing until zero. When the torque and the current are both under a specific threshold the inverter is switched off. Both the thresholds are imposed employing a comparator with an hysteresis band. This is composed by two thresholds: a high one and a low one. When the input goes below the low threshold, the logic output is equal to one and remains so until the input overcomes the high one. On the other hand, when the input is higher than the high threshold the logic output is equal to zero and remains so until the input goes below the low one. The current thresholds are equal to $30\,A$ and $15\,A$, while the torque ones are $2\,Nm$ and $0.1\,Nm$. Then the innovative actuator works for $0.3\,s$, after this, when safety conditions are obtained, the inverter is switched on again and the torque gets back to the original value.

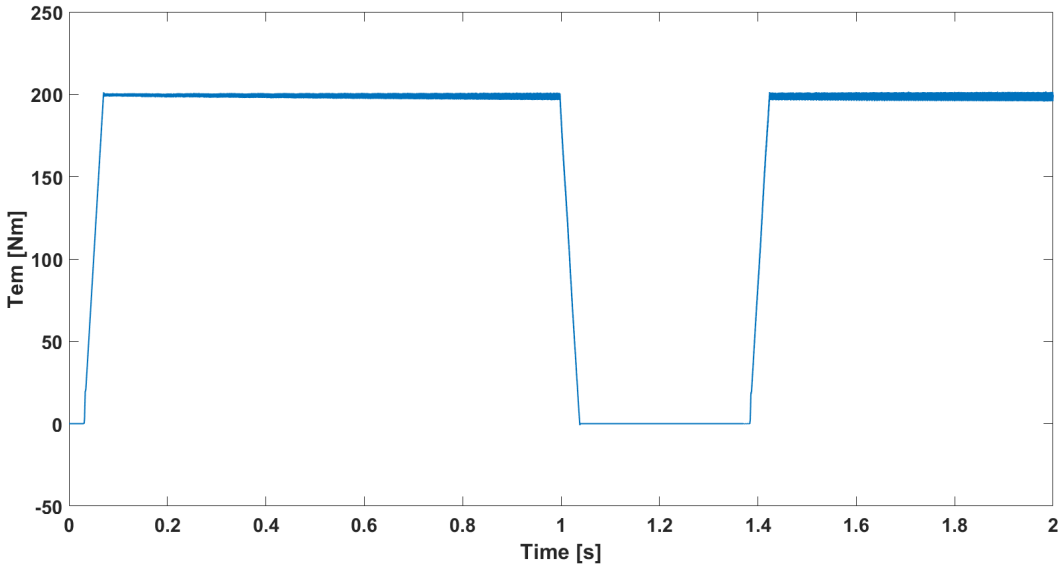

Figure 4.14: Torque evolution during the high level control test

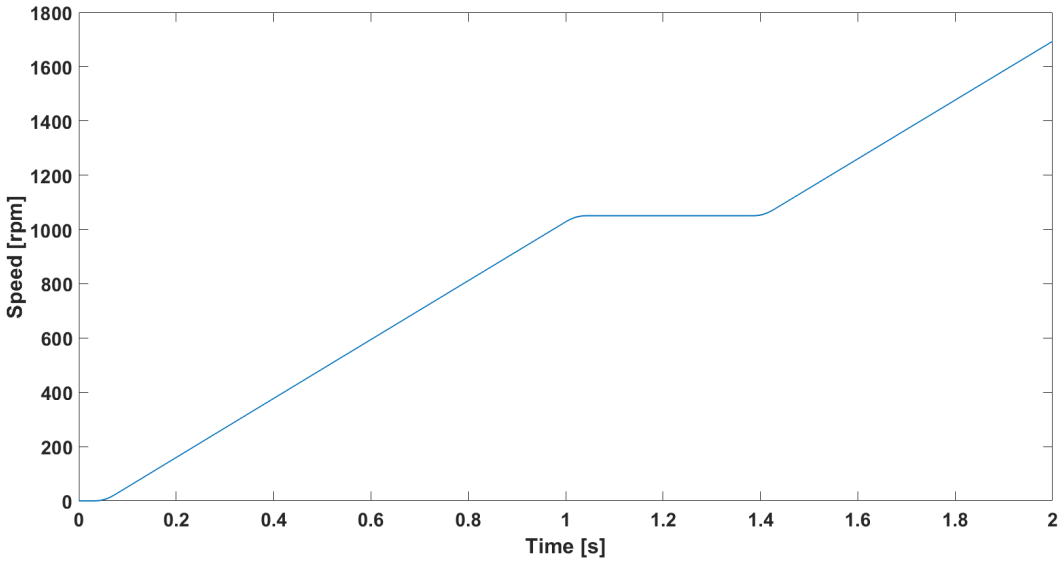

Figure 4.15: Speed evolution during the high level control test

The speed during the actuator operation does not change due to no additional torque source is considered or element that dispel mechanical power.
The phase currents follow the same evolution of the torque. As previously mentioned they are limited to the maximum value allowable, which is $500\,A$. When the inverter is switched off they are not all equal to zero, for example in this case the phase a current is equal to $6\,A$. This remaining current is interrupted abruptly leading to an overvoltage in the respective phase that reaches $90\,V$.

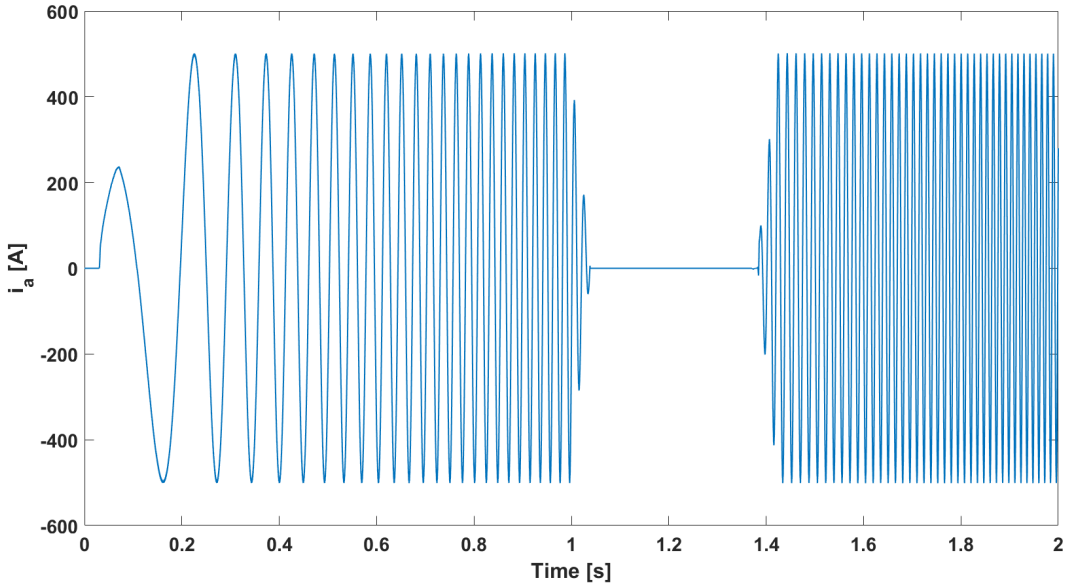

Figure 4.16: Phase a current evolution during the high level control test

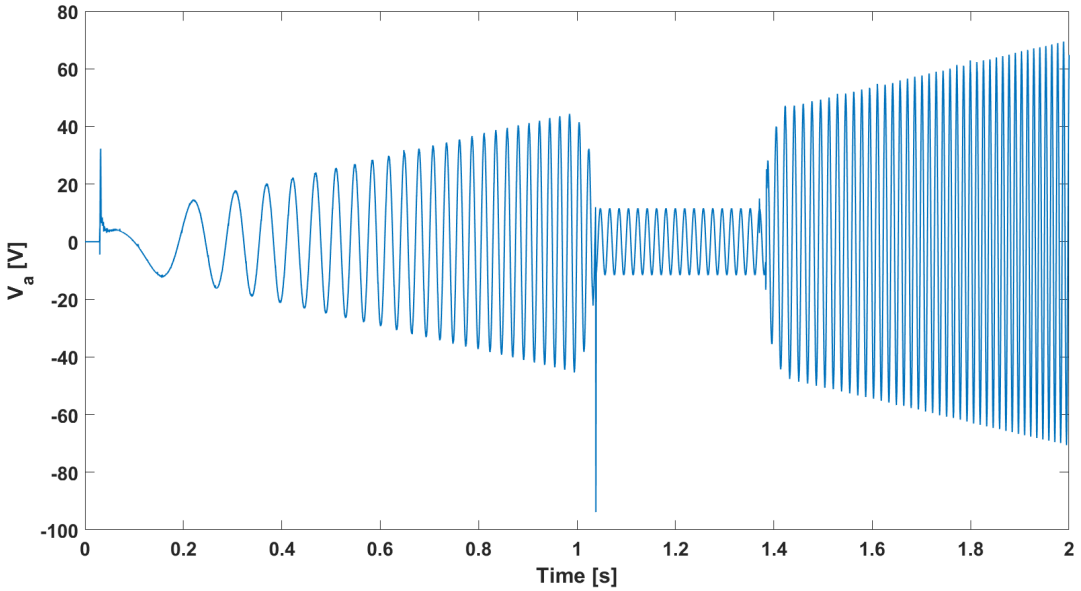

Figure 4.17: Phase a voltage evolution during the high level control test

The voltage during the actuator operation is equal to the magnet back-emf. In this case it is certainly lower than the V_{DC} avoiding the uncontrolled generation phenomenon.
In order to test the reliability of the control, another simulation is done where the UCG is wanted. Therefore the trigger is required when the speed is near to $18000\,rpm$. The equivalent inertia is lowered in order to reduce the simulation time and the DC-link voltage is imposed equal to $200\,V$ so that UCG phenomenon is visible.

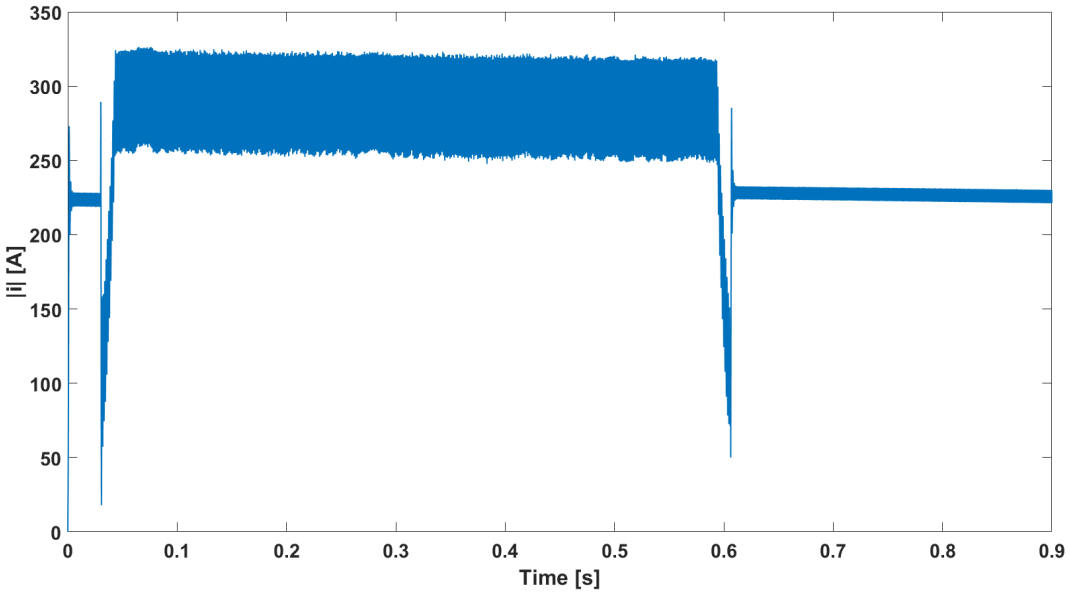

Figure 4.18: Phase a current evolution during the second high level control test

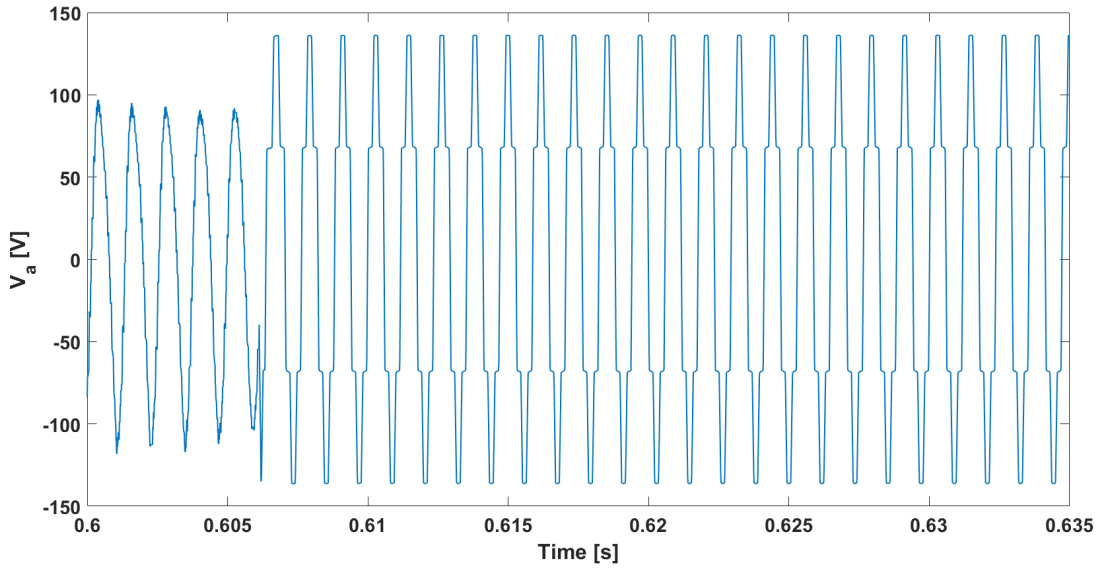

Figure 4.19: Detail of phase a voltage evolution during the second high level control test

In Fig. 4.18, it is possible to highlight that after the inverter shut-down, the current does not become equal to zero due to the uncontrolled generation phenomenon, thus the inverter is not properly switched off and the actuator cannot work. The voltage during the UGC is represented in Fig. 4.19. As it is possible to notice, hypothesising a sinusoidal equilibrate three-phase voltage tern, the line-to-line voltage is higher than the DC-link one:

$$V_{ab} = V_a \sqrt{3} = 136 \sqrt{3} = 235.6V \tag{4.4}$$

Chapter 5

Temperature and magnet back-emf evaluation

As analysed in 4.1, the temperature and the magnet back-emf have to be monitored in order to make the electromechanical actuator operate when safety operations are required. The two quantities that have to be estimated are characterised by a close relationship. The magnet flux is strictly related to its temperature: when the temperature increase, the magnet flux decrease and viceversa.
This can be expressed through:

$$\lambda_M = K_{Br} \left(Temp_M - Temp_{M0} \right) + \lambda_{M0} \tag{5.1}$$

where:

- K_{Br} is a coefficient assumed to be constant;
- $Temp_M$ is the magnet temperature;
- λ_{M0} is the known magnet flux at a known magnet temperature $Temp_{M0}$.

In the case of NdFeB magnet, the law is :

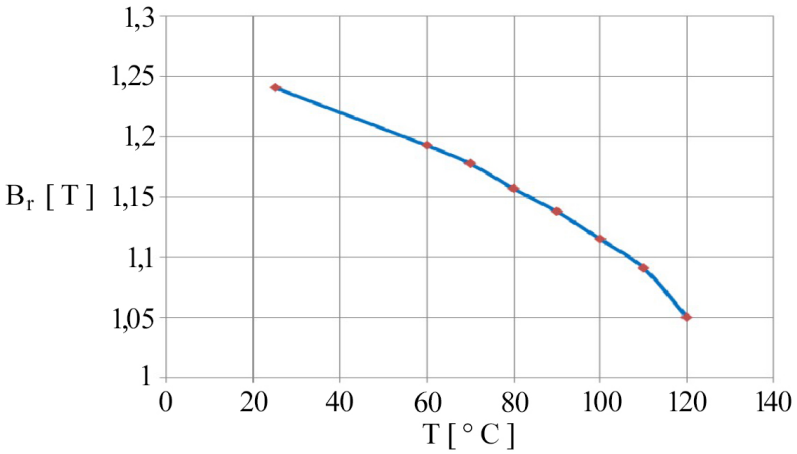

Figure 5.1: NdFeB magnetic remanence as a function of temperature

Therefore, if the magnet temperature is estimated also the magnet back-emf can be estimated if it is known in a determined temperature condition.
There are different possible methods available to do this:

- temperature measurement method;
- thermal model method;
- flux-observing method;
- signal injection method.

These methods will be investigated to understand the best suitable for this case under study. The implemented method will not be analysed due to confidentiality issues, while its results will be shown.

5.1 Temperature measurement method

The first method is a direct measurement of temperature through sensors. There are different available methods to measure directly the temperature and they can be divided in three categories:

- sensor with direct transmission through slip ring;
- sensor with wireless transmission;
- infra-red camera.

The first two are based on the positioning inside the rotor of the temperature sensor, which can be of different type such as thermocouple or Resistive Temperature Detector (RTD). A first disadvantage can be found in the necessity to change the rotor shape, thus changing the machine parameters and performance. Furthermore, these systems must have a high immunity to electromagnetic interference, sustain high temperature up to 180°C and centrifugal forces. Therefore they must be highly robust system negatively impacting on the whole cost. Moreover the complexity is to collect the data that are coming from the sensor due to their embedding inside the rotor, which is rotating.
In the first case slip rings are employed to overcome the carrying out of rotating wires. This technique is successfully implemented in some cases (Fig. 5.2), although mainly in experimental settings and not in an automotive case [26].

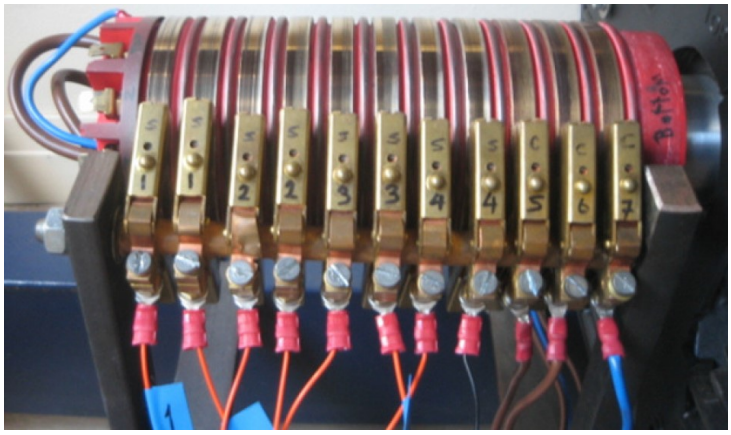

Figure 5.2: Shaft mounted brush slip-rings for temperature sensors embedded in the rotor

The reason of this can be found in several troubles that affect this strategy. The first one is the necessary enlargement of the motor shaft that lead to an unwanted increased space occupation, but also to a limitation of the rings number. Furthermore, as all the applications based on slip ring, it is characterized by mechanical weakness which results in a limited speed range. Therefore only low speed operations are allowed, completely excluding the automotive world.
In the second case wireless transmission is employed to send data to an external board.The carrier through which the data are transmitted can be of different kind: radio telemetry,

optical fibre, infra-red or Bluetooth. For each carrier type there are different advantages and disadvantages encountered in distinct scientific papers:

- Radio telemetry is based on a $433\,MHz$ carrier frequency [27]. The disadvantages, such as data loss, are mainly based on electromagnetic interference, which can be avoided increasing the power of wireless transmission, although this means an increase in power consumption [28];
- Optical fibre is based on the data transmission through light [29], it has the advantage of being highly immune to electromagnetic interference, but it is quite expensive and requires a perforated shaft to which the light emitter has to be centred;
- Infra-red is similar to the optical fibre, but based on emitting infra-red LED [28], it is relatively precise and immune to electromagnetic interference, but it has the same disadvantages of the optical fibre with also the necessity of a very precise and balanced manufacture, limiting its application to laboratory test environment;

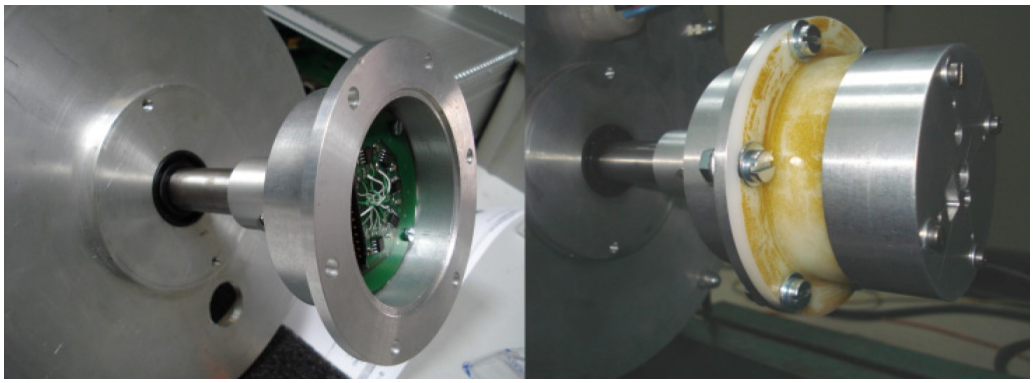

Figure 5.3: Installation of the rotor temperature monitoring instrumentation in [28]

- Bluetooth is based on a $2.45\,GHz$ carrier frequency [30], it is highly precise with an error bound of ± 1.5°C but it is not totally immune to electromagnetic interference.

In addition another disadvantage is the lifetime of the energy system for the sensor and the board embedded in the rotor. This is not unlimited and it has to be accessible from the outside in order to change it. The energy system is usually a battery, which has also the problem of the operating temperature.
In the third case, there are no sensor positioned inside the rotor and the temperature is measured through an infra-red camera outside the rotor. This technique is effective only if the surface under investigation is accessible by line-of sight [31]. Therefore if the electric machine is a surface mount magnet this technique is applicable, while in the case of internal permanent magnet it is not.

In conclusion, the main advantage of these technique is the direct measurement of the temperature that is independent from all the machine parameters. On the other hand, the disadvantages are the possible changes of the machine parameters and performance, the complex mechanical installation and the additional cost of sensors and board.

5.2 Thermal model method

This method is based on the analysis of the thermal behaviour of the electrical machine through the generation of an equivalent electric circuit, which is called lumped-parameter thermal network ($LPTN$) [32]. Considering two points among which an heat flux $\dot{Q}$ flows and there is a temperature difference ΔT, it is possible to define a thermal resistance R_{th} that respects the following equation:

$$\Delta T = R_{th}\,\dot{Q} \tag{5.2}$$

All the most relevant points of the electrical machine, such as at the ends of a permanent magnet, become the nodes of the equivalent electric circuit. This is build upon the following equivalences:

Thermal world		**Electric world**	
Temperature difference	ΔT	Voltage	V
Heat flux	$\dot{Q}$	Current	I
Thermal resistance	R_{th}	Electric resistance	R_{el}

Table 5.1: Equivalence between thermal and electric world

The temperature difference is seen as a difference of potential, thus as a voltage. If the temperature has to be imposed in one point, such as the ambient temperature, a voltage generator is introduced equal to the necessary temperature.
The heat flux is generated from power losses in the motor case: all of them are considered as a current generator in the $LPTD$.
The thermal resistances have to be evaluated with respect to the geometric and physical characteristics of the motor. The thermal resistance is principally of two types: conductive and convective. In the first case, considering these hypothesis:

- cylindrical element (Fig. 5.4);
- heat flux in radial and axial direction are independent;
- thermal capacity and heat generation are uniformly distributed;
- circumferential heat flux is neglected;
- a temperature θ_m defines the heat flow in both axial and radial direction.

two different thermal network can be find out: a radial one and an axial one (Fig. 5.5) [33].

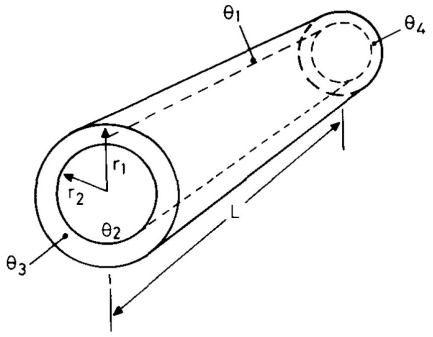

Figure 5.4: General cylindrical component

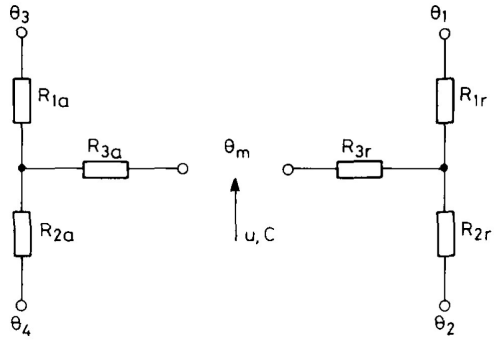

Figure 5.5: Independent axial and radial thermal network

These thermal resistances can be evaluated as follows:

$$R_{1a} = \frac{L}{2\pi k_a (r_1^2 - r_2^2)} = R_{2a} \qquad R_{3a} = \frac{-L}{6\pi k_a (r_1^2 - r_2^2)}$$

$$R_{1r} = \frac{1}{4\pi k_r L}\left[1 - \frac{2r_2^2 ln\left(\frac{r_1}{r_2}\right)}{r_1^2 - r_2^2}\right]$$

$$R_{2r} = \frac{1}{4\pi k_r L}\left[\frac{2r_1^2 ln\left(\frac{r_1}{r_2}\right)}{r_1^2 - r_2^2} - 1\right] \tag{5.3}$$

$$R_{3r} = \frac{-1}{8\pi (r_1^2 - r_2^2) k_r L}\left[r_1^2 + r_2^2 - \frac{4r_1^2 r_2^2 ln\left(\frac{r_1}{r_2}\right)}{r_1^2 - r_2^2}\right]$$

where k_a and k_r are respectively the axial and radial thermal conductivities.

In the second case, it is modelled through a single thermal resistance, evaluated as:

$$R_c = \frac{1}{h\,A_c} \tag{5.4}$$

where A_c is the area of the surface in contact with the fluid and h is the boundary film coefficient, which evaluated with respect to the motor under study.

Returning back to the *LPTN*, the first step is to evaluate it through the analysed thermal resistance and according to the electric machine in question. Considering that it is mainly composed by cylindrical elements, an axial *LPTN* and a radial *LPTN* can be found out, as shown in Fig. 5.6 [32]:

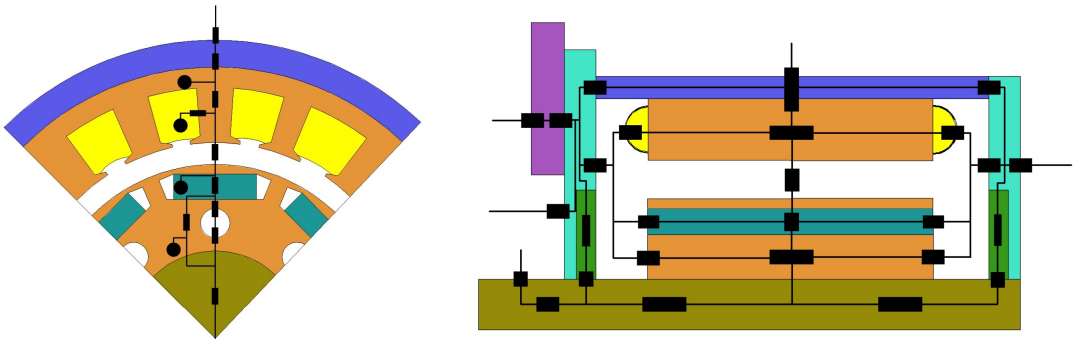

(a) Radial view of *LPTN* (b) Axial view of *LPTN*

Figure 5.6: Possible *LPTN* of a PMASR motor

The second step is to evaluate all the thermal resistances though the geometric and physical properties of the motor or through laboratory test. The principal test adopted is the DC thermal test [32], in which the motor is supplied in DC current and reach the thermal balance.
After the construction of the *LPTN*, the losses are evaluated and the magnet temperature can be calculated. As it is possible to understand, this method accuracy and time-consumption depend on the *LPTN* complexity: if the *LPTN* is built with a great degree of complexity, the method will be very accurate but also highly time-consuming. If something is neglected voluntarily or not, such as external heat sources or some kind of losses, it is particularly difficult to obtain a great precision with this method [34]. Furthermore this method lead to the evaluation of a mean temperature over a determined time period, thus faster dynamics than this are completely neglected.

5.3 Flux-observing method

This method is based on the estimation or observation of permanent magnet flux in the electrical machine, therefore the temperature is evaluated through the inverse of equation 5.1.
There are different methods for the magnet flux estimation, two of them are analysed:

- KF or EKF method [35] and [36];
- Flux-observer variant [37];

5.3.1 Kalman Filter

The first one is the Kalman Filter or its Extended version. It is a recursive filter, which is usually employed for measurements affected by noise. The central idea is the update of the estimation in the light of a new measurement in order to improve the estimation [38]. The procedure followed is now explained for a time varying single variable [38], whose evolution follows:

$$x_{n+1} = \Phi_n \, x_n + w_n \tag{5.5}$$

where Φ_n is the time variation of x and w_n is an additional noise with a zero mean distribution. The prediction of x is called $\hat{x}_{n+1|n}$ and it is natural to be considered as 5.6, neglecting the noise:

$$\hat{x}_{n+1|n} = \Phi_n \, \hat{x}_{n|n} \tag{5.6}$$

The variance of $\hat{x}_{n+1}$ is equal to:

$$P_{n+1|n} = \Phi_n^2 \, E\{(\hat{x}_{n|n} - x_n)^2\} + E\{w_n\} \tag{5.7}$$

where the $E\{...\}$ represents the expectation operator. A measurement of the scalar y_{n+1}, which is linearly related to x_{n+1} by H_{n+1}, is considered:

$$\hat{y}_{n+1} = H_{n+1} \, x_{n+1} + v_{n+1} \tag{5.8}$$

where v_n is again an additional noise with a zero mean distribution. The variance of $\hat{y}_{n+1}$ is equal to:

$$R_{n+1} = E\{v_{n+1}^2\} \tag{5.9}$$

The update of the prediction $\hat{x}_{n+1|n}$, shown in 5.6, is equal to:

$$\hat{x}_{n+1|n+1} = \hat{x}_{n+1|n} + K_{n+1} \left[\hat{y}_{n+1} - H_{n+1} \, \hat{x}_{n+1|n}\right] \tag{5.10}$$

where K_{n+1} is the Kalman Gain, which evaluated in order to minimize the variance of $\hat{x}_{n+1|n+1}$ as:

$$K_{n+1} = \frac{P_{n+1|n} \, H_{n+1}}{H_{n+1}^2 \, P_{n+1|n} + R_{n+1}} \tag{5.11}$$

This process can be extended to a vector of time varying variables on the same principle.

This method is applied to the electrical machine equations analysed in 2.3, which can be written as:

$$\dot{x}(t) = A\,x(t) + B\,u(t) \tag{5.12}$$

Taking into account what previously analysed, they can be written as:

$$\begin{cases} \dot{x}(t) = A\,x(t) + B\,u(t) + \sigma(t) \\ y(t_n) = H\,x(t_n) + \mu(t_n) \end{cases} \tag{5.13}$$

where t_n is a determined time instant, $\sigma(t)$ and $\mu(t_k)$ are the noises with a zero mean distribution. The first one represents the model inaccuracy, while the second one represents the measurement noise. The prediction $\hat{x}_{n|n-1}$ is equal to [36]:

$$\hat{x}_{n|n-1} = (A\,T_s + 1)\,\hat{x}_{n-1|n-1} + B\left(u_{n-1}\right)T_s \tag{5.14}$$

where T_s is the time interval length between t_n and t_{n-1}. The update of this prediction is done through the measurement y and it is equal to:

$$\hat{x}_{n|n} = \hat{x}_{n|n-1} + K_n\left[\hat{y}_n - H_n\,\hat{x}_{n|n-1}\right] \tag{5.15}$$

where K_n is the Kalman gain and it is under the form of a matrix, calculated as:

$$\begin{cases} K_n = P_{n|n-1}\,H'_n(H_n\,P_{n|n-1}\,H'_n + R)^{-1} \\ \\ H_n = \left.\dfrac{\partial h(x)}{\partial x}\right|_{x=\hat{x}_{n|n-1}} \end{cases} \tag{5.16}$$

Therefore, this method is employed to obtain the permanent magnet flux and then temperature is calculated through the inverse of 5.1. This procedure is effective and quite accurate, although it is tested only for a surface-mount permanent magnet motor and a synchronous reluctance motor [36], thus neglecting the cross coupling between d-axis and q-axis.

5.3.2 Flux-observer variant

The second method is based on the flux observer described in 3.5 with some modifications employed to obtain the permanent magnet temperature. In specific the estimator based on stator equation is employed and a feedback based on the difference between measured and estimated currents in dq-axes is added.
In [37], the flux in dq-axes is obtained making discrete the derivative in the stator equation (Eq. 5.17) and applying the rotational transform (Eq. 5.18):

$$v_{\alpha\beta,k} = R_s\,i_{\alpha\beta,k} + \frac{\lambda_{\alpha\beta,k+1} - \lambda_{\alpha\beta,k}}{T_s} \tag{5.17}$$

$$\lambda_{dq,k} = A\big(\theta_{k+1} - \theta_k\big)\left[\lambda_{dq,k-1} + T_s\,v_{dq,k-1} - A\left(\frac{\theta_{k+1} - \theta_k}{2}\right)T_s\,R_s\,i_{dq,k}\right] \tag{5.18}$$

where $A(...)$ is the rotational transform done with the angle indicated in brackets and θ is the rotor position.

The feedback is a flux, which is added to the one coming from the stator estimator. It is evaluated as the output of a PI regulator (discretize in 5.19), whose input is the difference between the measured and estimated currents in dq-axes:

$$\Delta\hat{\lambda}_{dq,k} = \begin{bmatrix} 0 & 0 \\ 0 & 1 \end{bmatrix} K_i\, T_s\, (i_{dq,k} - \hat{i}_{dq,k}) + \Delta\hat{\lambda}_{dq,k-1} \tag{5.19}$$

The estimated currents in dq-axes are evaluated through the inverse of the magnetic model, whose input are estimated fluxes in dq-axes coming from 5.18 with the addition of the feedback.
The flux in dq-axes can be written as a flux known in a determined temperature condition summed with the variation caused by the temperature change, hypothesising the latter influences only the flux in q-axis:

$$\lambda_{dq}(i_{dq}; Temp_M) = \lambda_{dq}(i_{dq}; Temp_{M0}) + \begin{bmatrix} 0 \\ 1 \end{bmatrix} K_{Br}\,(Temp_M - Temp_{M0})\,\lambda_{M0} \tag{5.20}$$

Consequently the temperature is calculated as:

$$Temp_{M,k} = \frac{\Delta\hat{\lambda}_{q,k}}{K_{Br}\,\lambda_{M0}} + Temp_{M0} \tag{5.21}$$

where the $\Delta\hat{\lambda}_{q,k}$ is equivalent to the one evaluated in 5.19.
Therefore, the scheme employed is the following:

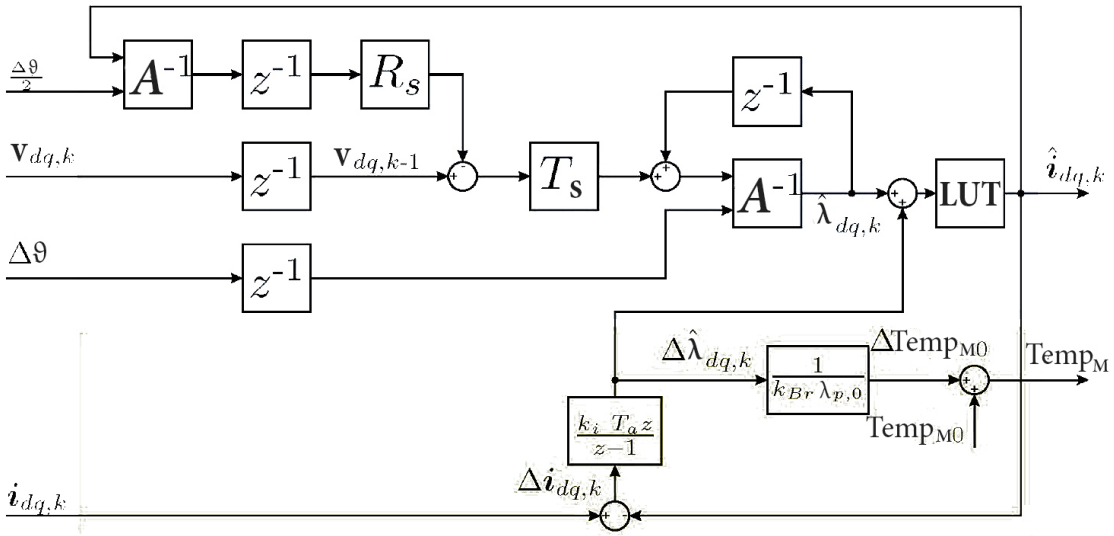

Figure 5.7: Scheme of the temperature observer developed in [37]

This method demonstrates satisfying performances with small errors on the estimated temperature, although it can not be applied at very low speeds. Furthermore, it is strongly dependent on the degree of knowledge of the parameters employed in the model, such as the stator resistance.

5.4 Signal-injection method

This technique is build upon the injection of a voltage or a current with specific characteristics and in specific conditions in order to monitor the electrical machine response, through which the parameters under interest are estimated. There are different methods to do this and most of them are based on the expected response of the electrical machine to a determined stimulation.
Two different procedures are now analysed:

- zero d-axis current injection [34];
- q-axis voltage pulse [39].

5.4.1 Zero d-axis current injection

The principle of this technique is to control for few milliseconds the d-axis current in order to make it equal to zero. On the other hand the q-axis current is maintained equal to its previous reference value. Starting from the electrical machine equation, analysed in 2.3:

$$\begin{cases} v_d = R_s\, i_d + L_{dd}\,\dfrac{di_d}{dt} + L_{dq}\,\dfrac{di_q}{dt} - \omega\,(L_{qd}\, i_d + L_{qq}\, i_q + \lambda_m) \\ \\ v_q = R_s\, i_q + L_{qd}\,\dfrac{di_d}{dt} + L_{qq}\,\dfrac{di_q}{dt} + \omega\,(L_{dd}\, i_d + L_{dq}\, i_q) \end{cases} \tag{5.22}$$

Two conditions are imposed: d-axis current equal to zero and steady state is reached. The equation 5.22 can be written as:

$$\begin{cases} v_d = -\omega\,(L_{qq}\, i_q + \lambda_m) \\ \\ v_q = R_s\, i_q + \omega\, L_{dq}\, i_q \end{cases} \tag{5.23}$$

Therefore, it is possible to calculate the q-axis flux as:

$$\lambda_{q,zero} = L_{qq}\, i_q + \lambda_m = -\frac{v_d}{\omega} \tag{5.24}$$

This flux has a linear relationship with temperature, if the temperature increases:

- L_{qq} increases too, due to the reduced core saturation level, and i_q is major than zero, thus the first term globally increases;
- λ_m decreases with temperature, but it is negative because it is directed along q-axis negative direction, thus the second term globally increases too.

Therefore, the q-axis flux increases as temperature rise with a thermal coefficient higher than the one of the permanent magnet flux. In this way the temperature variation can be estimated. The disadvantage of this method is that the d-axis current is equal to zero for a time interval, leading to a higher torque and speed ripple.

5.4.2 Q-axis voltage pulse

This method is based on a q-axis voltage pulse injection with the consequent measurement of the q-axis current response. This current is chosen because the permanent magnet flux level influences more it than the current d-axis. The q-axis current response is strongly influenced by the currents in dq-axes and the magnet temperature, which influences the magnet flux:

$$\frac{di_q}{dt} = f(i_d; i_q; Temp_M) \tag{5.25}$$

If this relationship is known, it is possible to evaluate the magnet temperature starting from the knowledge of the q-axis current response. In order to know this relationship laboratory test must be done due to its high non-linearity.
The procedure to obtain the q-axis current response is to inject a voltage pulse in the negative direction of the q-axis, along one of the six basic vector of the hexagon. For example the voltage pulse is injected in the phase a as shown in:

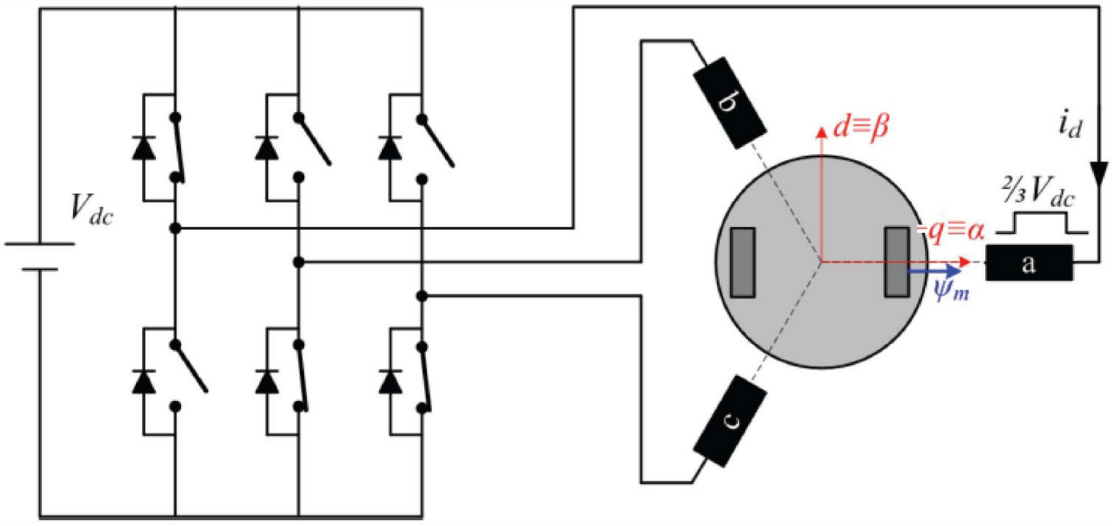

Figure 5.8: Voltage pulse injection in the phase a

This pulse cannot be given exactly when $\theta_{el} = 0°$ but it extended before and after with a width of t_{pw}, tried to kept as shorter as possible in order to obtain:

$$v_d \cong v_\beta \qquad v_q \cong -v_\alpha \qquad i_d \cong i_\beta \qquad i_q \cong -i_\alpha \tag{5.26}$$

Since the q-axis current response is influenced by the d-axis current, due to the cross-saturation phenomenon and the influence on the q-axis voltage, it is necessary to compensate the d-axis current.

Starting from the electrical machine equation:

$$\begin{cases} v_d = R_s\, i_d + L^*_{dd}\,\dfrac{di_d}{dt} + L^*_{dq}\,\dfrac{di_q}{dt} - \omega\,(L_{qd}\, i_d + L_{qq}\, i_q + \lambda_m) \\ \\ v_q = R_s\, i_q + L^*_{qd}\,\dfrac{di_d}{dt} + L^*_{qq}\,\dfrac{di_q}{dt} + \omega\,(L_{dd}\, i_d + L_{dq}\, i_q) \end{cases} \tag{5.27}$$

where L^* are the differential inductances:

$$\begin{aligned} L^*_{dd} &= L_{dd} + \frac{dL_{dd}}{di_d} i_d \qquad & L^*_{dq} &= L_{dq} + \frac{dL_{dq}}{di_q} i_q \\ L^*_{qd} &= L_{qd} + \frac{dL_{qd}}{di_d} i_d \qquad & L^*_{qq} &= L_{qq} + \frac{dL_{qq}}{di_q} i_q \end{aligned} \tag{5.28}$$

Therefore, injecting a negative voltage pulse in q-axis $v_q = -\frac{2}{3}V_{DC}$ from 5.27 it possible to obtain the q-axis current response:

$$L^*_{qq}\,\frac{di_q}{dt} = -\frac{2}{3}V_{DC} - R_s\, i_q - L^*_{qd}\,\frac{di_d}{dt} - \omega\,(L_{dd}\, i_d + L_{dq}\, i_q) \tag{5.29}$$

Furthermore it is possible to delete the dependence on the d-axis current and partially delete the speed dependence. The procedure to do this is to inject another voltage pulse but of opposite sign $v_q = \frac{2}{3}V_{DC}$, obtaining:

$$L^*_{qq}\,\frac{di_{qP}}{dt} = \frac{2}{3}V_{DC} - R_s\, i_{qP} - L^*_{qd}\,\frac{di_d}{dt} - \omega\,(L_{dd}\, i_d + L_{dq}\, i_{qP}) \tag{5.30}$$

Consequently, subtracting 5.30 with 5.29:

$$L^*_{qq}\,\frac{d(i_{qP} - i_{qN})}{dt} = \frac{4}{3}V_{DC} - R_s\,(i_{qP} - i_{qN}) - \omega\, L_{dq}\,(i_{qP} - i_{qN}) \tag{5.31}$$

This derivative reflects the changes in the magnetization level while d-axis current is constant.
This method is characterized by a high accuracy along a wide speed-range, nevertheless at high speed it is more difficult to inject the voltage pulse at the right moment. Furthermore this method can cause additional losses and torque or speed ripple.

5.5 Implemented method and results

The four methods employed to estimate the magnet temperature and previously analysed have each one advantages and disadvantages, which are resumed in the following table:

Method	Advantages	Disadvantages
Temperature measurement	Direct measurement of the temperature	– Expensive – Mechanical and temperature criticality – Mainly limited to laboratory environment
Thermal model	Estimate not only the rotor temperature	– Time-consuming – Possible errors in case of losses neglect, wrong assumption on the ambient or inaccurate knowledge of the motor geometry – Mainly limited to industrial environment
Flux-observing	– No additional cost – No time consuming	– Possible errors in case of an inaccurate machine and inverter model – Very sensitive to variable parameters such as stator resistance (stator temperature sensors required)
Signal injection	– No additional cost – No time consuming	– Additional losses – Torque and speed ripple – Mainly applicable at low speed

Table 5.2: Advantages and disadvantages of the method for the magnet temperature estimation

Among these techniques, a flux-observing method is chosen. For confidentiality issue the way how it works is not treated in this thesis, while the results are shown.

A test is conducted in the simulation environment, its parameters are the following:

- magnet temperature $Temp_M = -10°C$;
- torque requested equal to $T_{em} = 30\,Nm$;
- speed range from $250\,rpm$ to $6000\,rpm$;
- simulation time $3\,s$.

Every test is done at speed imposed, thus the speed is constant in the whole test. The initial value of the estimated temperature is set to zero and then evolves till steady-state.

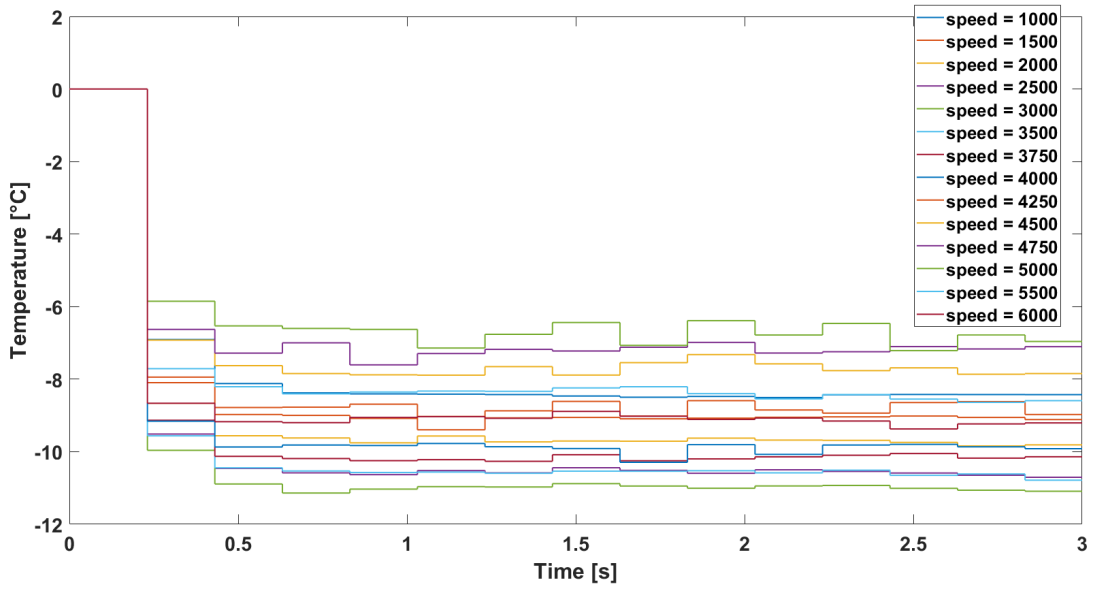

Figure 5.9: Evolution of the temperature estimation at different speed

As it is possible to notice the estimated temperature is different according to the imposed speed. After the first transient phase, the maximum error is around 3.614°C for a speed of $5000\,rpm$, highlighting a great accuracy.
In order to show better the evolution of the temperature with speed, a mean temperature is calculated from $1\,s$ to $3\,s$ and plotted as a function of the speed:

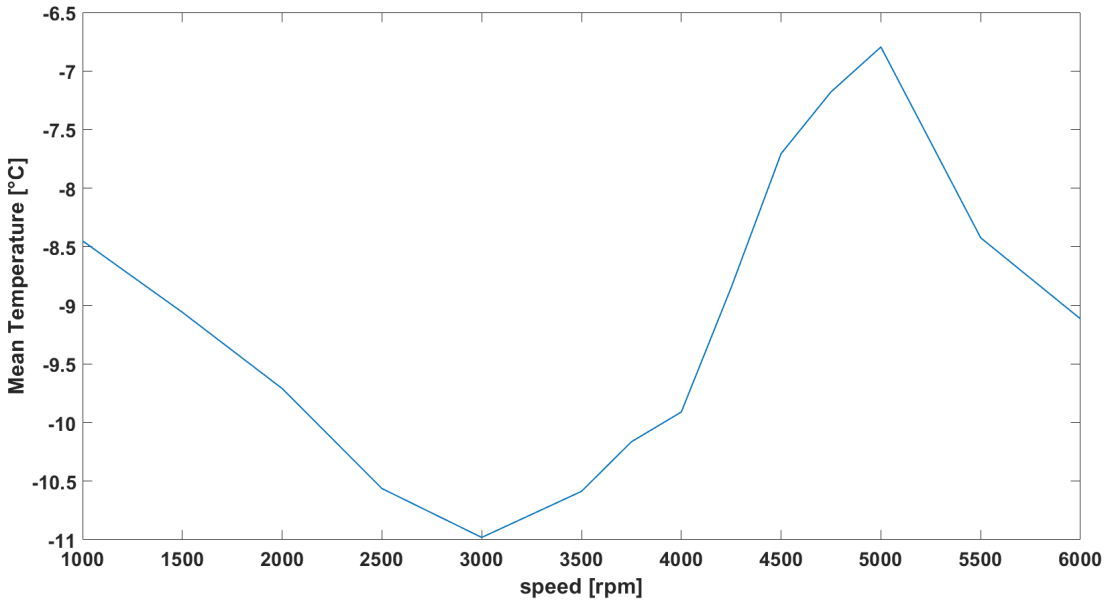

Figure 5.10: Mean temperature estimation as a function of the speed

Furthermore, an other test in the simulation environment is conducted with a different magnet temperature $Temp_M = 50°C$ and in three different torque request: low load at $30\,Nm$, medium load at $90\,Nm$ and full load at $200\,Nm$. The temperature estimator is changed in order to follow the faster evolution of the speed, thus an additional ripple is present in the three following graphs:

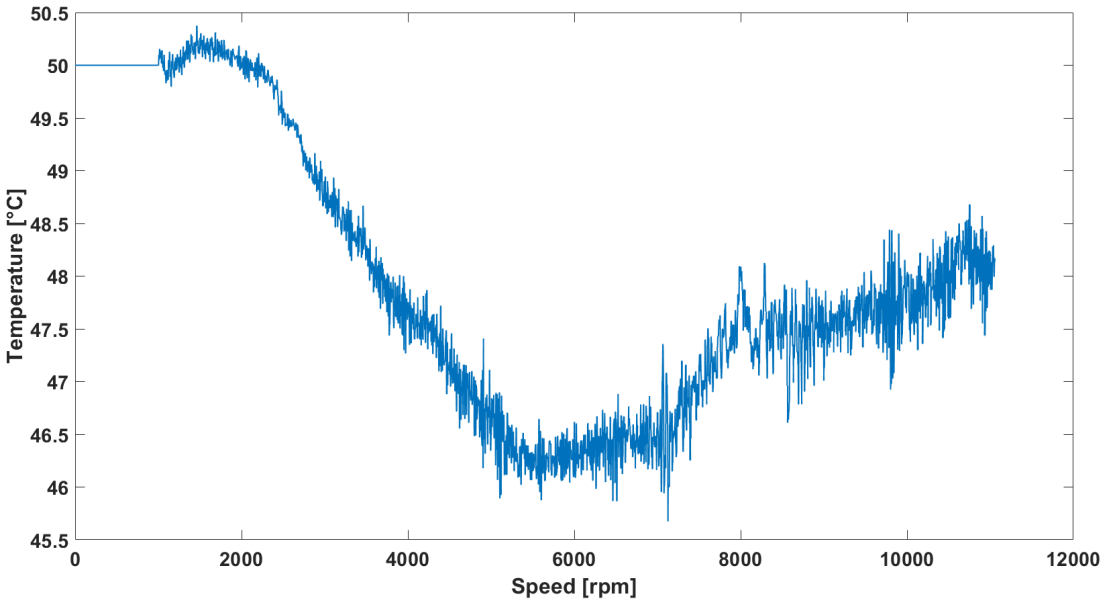

Figure 5.11: Temperature estimation as a function of the speed at low load

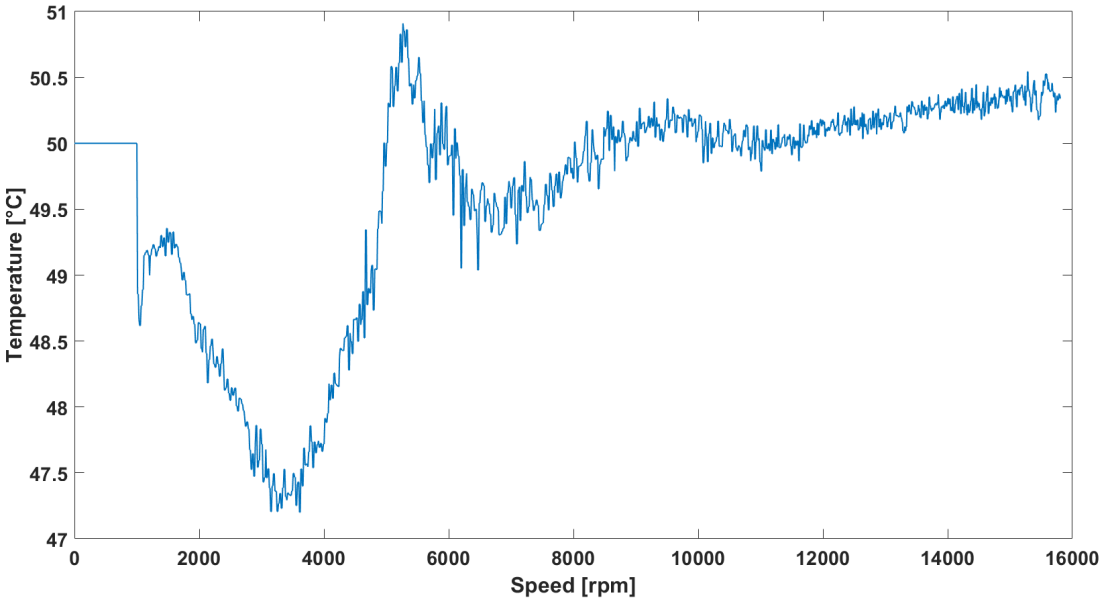

Figure 5.12: Temperature estimation as a function of the speed at medium load

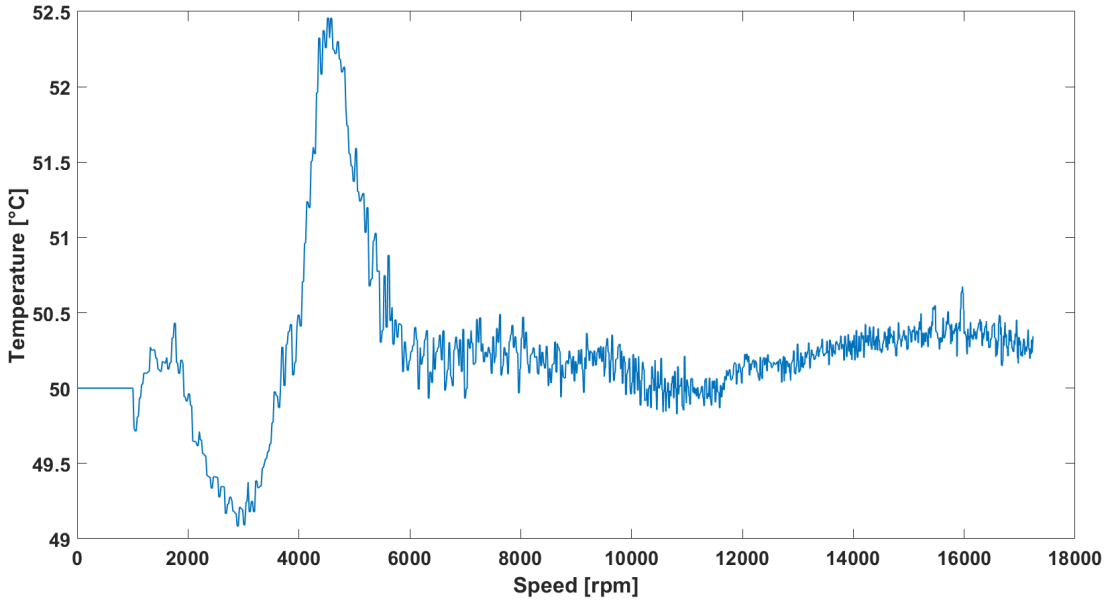

Figure 5.13: Temperature estimation as a function of the speed at full load

As it is possible to notice, the maximum speed reached is different according to the load due to the simulation time is imposed to $3\,s$. The evolution of the estimated temperature varies in the three cases. The error at steady-state is different in one case or the other, the minimum one is the full load case.

Furthermore also the maximum error is different:

- Maximum error at low load is equal to 4.3°C;
- Maximum error at medium load is equal to 2.8°C;
- Maximum error at full load is equal to 2.5°C.

Therefore, the developed method has a great accuracy over all the motor speed and torque range. Nonetheless it is tested in a simulation environment, thus a test on the real motor when it will be built is necessary to demonstrate its accuracy and effectiveness.

Chapter 6

Conclusion

This thesis dealt with different problematic, all concerning an innovative electrical drive for electrical vehicle. The electric traction system is successfully modelled in the simulation environment Simulink. Existing blocks are employed to model the energy storage, the converter and the mechanical load. On the other hand, a new circuit model for the electrical machine is introduced from the theoretical point of view and correctly modelled with a specific Simulink block. This motor modelling has great potentialities in the simulation world due to its high adaptability and flexibility. Future developments could be the implementation of other electrical machine dynamics, such the mechanical one or the losses aspect. Furthermore the comparison and test with the real electric traction system is strictly necessary to give a solid validity to this simulation model and to understand deeply its shortcomings.
The motor control together with the secondary motor control is satisfactorily implemented in the specific programming language. They are tested in the Simulation environment, highlighting their feasibility and validity. In particular the possibility of taking back the control instantaneously, after the innovative actuator operation, is shown. Further step is the necessary evaluation of these controls on the real electrical traction system.
A deep analysis of the state of art about permanent magnet temperature evaluation is conducted to allow proper operations of the innovative actuator. Advantages and disadvantages of each techniques are analysed and a new method is introduced. This method is not shown for confidentiality issue, but it is tested in the simulation environment. The results are promising and show the correctness and validity of the new method. Nonetheless the test with the real traction system will be strictly necessary, due to the typology of chosen method.
In conclusion the whole system generated with the control and monitoring logic represents a strong base for future developments in the electrical automotive world, highly necessary in this coming period of deep innovation.

Bibliography

[1] IEA (2019), "Global EV Outlook 2019", IEA, Paris, www.iea.org/publications/reports/globalevoutlook2019/.

[2] https://www.mckinsey.com/industries/automotive-and-assembly/our-insights/the-global-electric-vehicle-market-is-amped-up-and-on-the-rise

[3] https://edition.cnn.com/interactive/2019/08/business/electric-cars-audi-volkswagen-tesla/

[4] https://www.businessinsider.com/toyota-investing-in-electric-vehicles-indonesia-2019-7?IR=T

[5] https://it.3dexport.com/3dmodel-tesla-roadster-2020-green-with-interior-and-chassis-209902.htm

[6] https://www.techopedia.com/definition/16316/battery

[7] *MathWorks Documentation about Controlled Voltage Source block*, https://it.mathworks.com/help/physmod/simscape/ref/controlledvoltagesource.html

[8] *MathWorks Documentation about IGBT block*, https://it.mathworks.com/help/physmod/sps/ref/igbtidealswitching.html

[9] *MathWorks Documentation about Converter block*, https://it.mathworks.com/help/physmod/sps/ref/converterthreephase.html

[10] *MathWorks Documentation about FEM-Parameterized PMSM block*, https://it.mathworks.com/help/physmod/sps/ref/femparameterizedpmsm.html

[11] *MathWorks Documentation about Hybrid Excitation PMSM block*, https://it.mathworks.com/help/physmod/sps/ref/hybridexcitationpmsm.html

[12] *MathWorks Documentation about Three-phase controlled voltage source block*, https://it.mathworks.com/help/physmod/sps/ref/controlledvoltagesourcethreephase.html

[13] *MathWorks Documentation about Simscape component block*, https://it.mathworks.com/help/physmod/simscape/ref/simscapecomponent.html

[14] *MathWorks Documentation about Ideal Torque Source block*, https://it.mathworks.com/help/physmod/simscape/ref/idealtorquesource.html

[15] *MathWorks Documentation about Inertia block*, https://it.mathworks.com/help/physmod/simscape/ref/inertia.html

[16] *MathWorks Documentation about Rotational Free End block*, https://it.mathworks.com/help/physmod/simscape/ref/rotationalfreeend.html

[17] *MathWorks Documentation about Ideal Rotational Motion Sensor block*, https://it.mathworks.com/help/physmod/simscape/ref/idealrotationalmotionsensor.html

[18] G. Pellegrino, R. I. Bojoi and P. Guglielmi, "Unified Direct-Flux Vector Control for AC Motor Drives", IEEE Transaction on Industrial Application, vol. 47, no. 5, pp.

2093–2102, Sept./Oct. 2011.

[19] R. Bojoi, G. Pellegrino, A. Cavagnino and P. Guglielmi, "Direct Flux Vector Control of Axial Flux IPM Motors for in-Wheel Traction Solutions", IECON 2010 - 36th Annual Conference on IEEE Industrial Electronics, pp. 2224–2229, Dec. 2010.

[20] S. Hamidizadeh, N. Alatawneh, R. R. Chromik and D. A. Lowther, "Comparison of Different Demagnetization Models of Permanent Magnet in Machines for Electric Vehicle Application", IEEE Transaction on Magnetics, vol. 52, no. 5, May 2016.

[21] P. Peng, J. Zhang, W. Li, F. Leopardi, C. Rong, M. W. Degner, F. Liang and L. Zhu, "Temperature-Dependent Demagnetization of Nd-Fe-B Magnets for Electrified Vehicles", IEEE International Electric Machines and Drives Conference, pp. 2056-2062, 2019.

[22] M. D. Călin, E. Helerea and G. Anghel, "Temperature Influence and Measurement Uncertainty on NdFeB Magnetic Characteristics", 5th International Symposium on Electrical and Electronics Engineering, 2017

[23] J. Liu, X. Ding and C. Mi, "Effectively Dealing with Uncontrolled Generation of Traction Motors in Hybrid Electric Vehicles", International Conference on Electrical Machines and Systems, 2011.

[24] X. Ding, H. Guo, F. Yang and X. Du, "Uncontrolled Generation in Different Converter Systems", International Conference on Electrical Machines and Systems, pp. 119-121, Oct. 2013.

[25] C. Gong, Y. Hu, C. Gan, G. Chen and M. Alkahtani, "Modelling, Analysis and Attenuation of Uncontrolled Generation for IPMSM based Electric Vehicles in Emergency", IEEE Transaction on Industrial Electronics, 2019.

[26] C. Mejuto, M. Mueller, M. Shanel, A. Mebarki, M. Reekie and D. Staton, "Improved synchronous machine thermal modelling," International Conference on Electrical Machines (ICEM), pp. 1-6, Sep. 2008.

[27] H. Zhe and G. Guobiao, "Wireless rotor temperature measurement system based on MSP430 and nRF401", International Conference on Electrical Machines and Systems (ICEMS), pp. 858-861, Oct. 2008.

[28] M. Ganchev, H. Umschaden and H. Kappeler, "Rotor Temperature Distribution Measuring System", 37th Annual Conference of the IEEE Industrial Electronics Society, IECON, pp. 2006-2011, 2011.

[29] H. Yahoui, G. Grellet, "Measurement of physical signals in rotating part of electrical machine by means of optical fibre transmission", Instrumentation and Measurement technology Conference 1996, IMTC-96, vol. 1, pp. 591-596, Jun. 1996.

[30] D. Park, H. Jung, H. Cho and S. Sul, "Design of Wireless Temperature Monitoring System for Measurement of Magnet Temperature of IPMSM", IEEE Transportation Electrification Conference and Expo (ITEC), pp. 656-661, 2018.

[31] J. H. Dymond, R. Ong and N. Stranges, "Instrumentation, Testing, and Analysis of Electric Machine Rotor Steady-State Heating", IEEE Transaction on Industry applications, vol. 38, no. 6, Nov./Dec. 2002.

[32] W. Wang, Y. Zhou and Y. Chen, "Investigation of Lumped-parameter Thermal Model and Thermal Parameters Test for IPMSM", 17th International Conference on Electrical Machines and Systems (ICEMS), pp. 3246-3252, Oct. 2014.

[33] P. H. Mellor, D. Roberts and D. R. Turner, "Lumped Parameter Thermal Model for Electrical Machines of TEFC Design", IEEE Proceedings Electric Power Applications, vol. 138, no. 5, pp. 205-218, Sept. 1991.

[34] H. Kim, H. Jung, S. Sul1 and D. J. Berry, "IPMSM Magnet Temperature Estimation by d-axis Flux Linkage", 10th International Conference on Power Electronics (ECCE), pp. 2517-2522, May 2019.

[35] C. Wen, "A new on-line detection method of magnet flux linkage for permanent magnet synchronous motor", Chinese Control and Decision Conference, IEEE, 2009.

[36] X. Xiao, C. Chen and M. Zhang, "Dynamic Permanent Magnet Flux Estimation of Permanent Magnet Synchronous Machines", IEEE Transactions on applied superconductivity, vol. 20, no. 3, pp. 1085-1088, June 2010.

[37] A. Specht, O. Wallscheid and J. Bocker, "Determination of Rotor Temperature for an Interior Permanent Magnet Synchronous Machine Using a Precise Flux Observer", International Power Electronics Conference (IPEC), pp. 1501-1507, 2014.

[38] P.J. Hargrave, "A tutorial introduction to Kalman filtering", IEEE Colloquium on Kalman Filters: Introduction, Applications and Future Developments, 1989.

[39] M. Ganchev, C. Kral and T. Wolbank, "Sensorless Rotor Temperature Estimation of Permanent Magnet Synchronous Motor under Load Conditions", 38th Annual Conference on IEEE Industrial Electronics Society, pp. 1999-2004, 2012.

[40] G. Xie, K. Lu, S. K. Dwivedi, R. J. Riber and W. Wu, "Permanent Magnet Flux Online Estimation Based on Zero-Voltage Vector Injection Method", IEEE Transaction on Power Electronics, vol. 30, no. 12, pp. 6506-6509, Dec. 2015